ISSN : 2349-6495(P) | 2456-1908 (O)

International Journal of Advanced Engineering Research and Science

(IJAERS)

An Open Access Peer-Reviewed International Journal

Journal DOI: 10.22161/ijaers

Issue DOI: 10.22161/ijaers.125

AI PUBLICATIONS

Vol.- 12 | Issue - 5 | May 2025

editor.ijaers@gmail.com | editor@ijaers.com | https://www.ijaers.com/

International Journal of Advanced Engineering Research and Science (IJAERS)

(ISSN: 2349-6495(P)| 2456-1908(O))

DOI: 10.22161/ijaers

Vol-12, Issue-5

May, 2025

Publisher

AI Publication

Email: editor.ijaers@gmail.com; editor@ijaers.com

Web: www.ijaers.com

International Editorial/ Reviewer Board

Editor in Chief

- **Dr. Swapnesh Taterh (Chief-Editor),** Amity University, Jaipur, India

Cheif Executive Editor

- **S. Suman Rajest,** Vels Institute of Science, Technology & Advanced Studies, India
  chief-executive-editor@ijaers.com

Associate Editors

- **Dr. Ram Karan Singh,** King Khalid University, Guraiger, Abha 62529, Saudi Arabia
- **Dr. Shuai Li,** University of Cambridge, England, Great Britain

Editorial Member

- **Behrouz Takabi,** PhD, Texas A&M University, Texas, USA
- **Dr. Gamal Abd El-Nasser Ahmed Mohamed Said,** Port Training Institute (PTI), Arab Academy For Science, Technology and Maritime Transport, Egypt
- **Dr. Hou, Cheng-I ,** Chung Hua University, Hsinchu Taiwan
- **Dr. Ebrahim Nohani,** Islamic Azad University, Dezful, IRAN.
- **Dr. Ahmadad Nabih Zaki Rashed,** Menoufia University, EGYPT
- **Dr. Rabindra Kayastha ,** Kathmandu University, Nepal
- **Dr. Dinh Tran Ngoc Huy,** Banking and Finance, HCM, Viet Nam
- **Dr. Engin NAS,** Duzce University, Turkey
- **Dr. A. Heidari,** California South University (CSU), Irvine, California, USA
- **Dr. Uma Choudhary,** Mody University, Lakshmangarh, India
- **Dr. Varun Gupta,** National Informatic Center, Delhi, India
- **Dr. Ahmed Kadhim Hussein,** University of Babylon, Republic of Iraq
- **Dr. Vibhash Yadav,** Rajkiya Engineering College, Banda. UP, India
- **Dr. M. Kannan,** SCSVMV University, Kanchipuram, Tamil Nadu, India
- **José G. Vargas-Hernández,** University of Guadalajara Periférico Norte 799 Edif. G201-7, Núcleo Universitario Los Belenes, Zapopan, Jalisco, 45100, México
- **Dr. Sambit Kumar Mishra,** Gandhi Institute for Education and Technology, Baniatangi, Bhubaneswar, India
- **DR. C. M. Velu,** Datta Kala Group of Institutions, Pune, India
- **Dr. Deependra Pandey,** Amity University, Uttar Pradesh, India
- **Dr. K Ashok Reddy,** MLR Institute of Technology, Dundigal, Hyderabad, India
- **Dr. S.R.Boselin Prabhu,** SVS College of Engineering, Coimbatore, India
- **N. Balakumar,** Tamilnadu College of Engineering, Karumathampatti, Coimbatore, India
- **R. Poorvadevi,** SCSVMV University, Enathur, Kanchipuram, Tamil Nadu, India
- **Dr. Subha Ganguly,** Arawali Veterinary College, Sikar, India
- **Dr. P. Murali Krishna Prasad,** GVP College of Engineering for Women, Visakhapatnam, Andhra Pradesh, India
- **Anshul Singhal,** Bio Instrumentation Lab, MIT, USA
- **Mr. Lusekelo Kibona,** Ruaha Catholic University, Iringa, Tanzania
- **Sina Mahdavi,** Urmia Graduate Institute, Urmia, Iran
- **Dr. N. S. Mohan,** Manipal Institute of Technology, Manipal, India
- **Dr. Zafer Omer Ozdemir,** University of Health Sciences,Haydarpasa, Uskudar, Istanbul, TURKIYE
- **Bingxu Wang,** 2721 Patrick Henry St Apt 510, Auburn Hills, Michigan, United States

Vol-12, Issue-5, May 2025

(10.22161/ijaers.125)

Detail with DOI (CrossRef)
Determination of the Rigor Mortis Index for the species Eugerres brasilianus (Cuvier, 1830), Captured in Itaipava, Espírito Santo - Brasil Hugo A. M. Azevedo, Mileni S. P. Gonçalves, Thiago L. Oliveira, Débora B. Gava, Flavio C. G. Junior, Geslaine S. Oliveira, Paulo Henrique C. Lyrio, Marcelo G. Minozzo DOI: 10.22161/ijaers.125.1 Page No: 01-05
Culture of Innovation: The Impact on the Day-to-Day of an Organization Bruno Tadeu Ferreira da Silva, Alexandre Acácio de Andrade, Anderson Orzari Ribeiro DOI: 10.22161/ijaers.125.2 Page No: 06-11
DreamTalk-DMT: A Lightweight Sparse Mechanism Model with Dynamic Thresholds Jia Zhang, Lin Po Shang DOI: 10.22161/ijaers.125.3 Page No: 12-20
Mathematical Modeling and Simulation of an Alkaline Electrolyzer for Hydrogen Production Andrianaivoarivelo Jaolalaina Arisoa, Andrianjatovo Falinirina, Rafanjanirina Eulalie Odilette, Randriamanantany Zely Arivelo DOI: 10.22161/ijaers.125.4 Page No: 21-32
A Comparative Analysis of Logistic Regression and Random Forest for Individual Fairness in Machine Learning Sanjit Kumar Saha DOI: 10.22161/ijaers.125.5 Page No: 33-37
Diffraction Model on the Breakwater Gap Based on Velocity Potential Equation Syawaluddin Hutahaean DOI: 10.22161/ijaers.125.6 Page No: 38-44
Norms and Associated Health Hazard in Himalayan Water System: A Review Shagolsem Dungo Meitei, Pydikondala Narasimha Satya Abhiram, Rohit Singh Sajwan, Veena Joshi DOI: 10.22161/ijaers.125.7 Page No: 45-54

International Journal of Advanced Engineering Research and Science (IJAERS)
Peer-Reviewed Journal
ISSN: 2349-6495(P) | 2456-1908(O)
Vol-12, Issue-5; May, 2025
Journal Home Page Available: https://ijaers.com/
Article DOI: https://dx.doi.org/10.22161/ijaers.125.1

Determination of the Rigor Mortis Index for the species *Eugerres brasilianus* (Cuvier, 1830), Captured in Itaipava, Espírito Santo - Brasil

Hugo A. M. Azevedo[1], Mileni S. P. Gonçalves[2], Thiago L. Oliveira[3], Débora B. Gava[4], Flavio C. G. Junior[5], Geslaine S. Oliveira[6], Paulo Henrique C. Lyrio[7] and Marcelo G. Minozzo[8]

[1]Federal Institute of Education, Science and Technology of Espírito Santo, Rua Augusto Costa Oliveira, 660, Piúma, 29285-000, Espírito Santo, Brazil
Email: hugo.azevedo@estudante.ifes.edu.br

Received: 01 Apr 2025,

Receive in revised form: 03 May 2025,

Accepted: 08 May 2025,

Available online: 13 May 2025

***Keywords*— Carapeba; freshness; rigor mortis.**

***Abstract*—** *Fish has increasingly become an essential element in the search for sustainable protein sources in human nutrition. The diverse species available along the 8,000 km of our country's coastline provide a rich and varied source of food. To consolidate the fishing market, ensuring the quality of the food presented to the consumer is crucial. Among the existing ways to ensure the freshness of fish, the rigor mortis index reflects the biochemical aspects of the flesh and the stages it undergoes until it becomes unfit for human consumption. This study aimed to determine the rigor mortis index and its stages in the Carapeba species (E. brasilianus). The samples were captured on the beach of Itaipava, Espírito Santo, Brazil, and the experiment was conducted at IFES – Piúma Campus over a period of 30 hours. The measurements taken indicate that Carapeba exhibits pronounced and long-lasting rigor mortis indices, suggesting great potential in terms of quality and freshness. Specimens P2 and P3 reached the rigor mortis stage first, both at around 4.3 hours, while P1 took 5.3 hours. The full rigor mortis stage lasted 40 minutes for P1, whereas P2 and P3 remained in full rigor for 18.7 and 16.7 hours, respectively. The importance of this study for the species is notable, as even under stressful slaughter methods, the rigor mortis response time is significantly high, indicating an extremely attractive preservation potential.*

I. INTRODUCTION

According to data from the FAO 2024 report, in the year 2022, fishery and aquaculture production reached 223.2 million tons, with approximately 83% of this amount related to the fishing of fish, crustaceans, and mollusks, and 17% related to the extraction and cultivation of algae. Of these 223.2 million tons, 130.9 million tons come from aquaculture, while 92.3 million come from fishing (FAO, 2024).

Fish and crustaceans are important sources of protein for the entire population, especially in coastal areas. Fishery products serve as a source of high-quality proteins essential for the maintenance and repair of human body tissues. Additionally, fish are rich in omega-3 fatty acids, which help reduce the risk of cardiovascular diseases, improve brain function, and reduce inflammation in the body. They are also important sources of vitamins, such as vitamin D, which is essential for bone health, and B-complex vitamins, which play a crucial role in energy

metabolism. Minerals such as selenium, iodine, and zinc, present in fish, are fundamental for the proper functioning of the immune system and thyroid function control (Bito et al., 1983; Presenza et al., 2021).

Despite this nutritional significance, Brazil has low consumption rates, struggling to surpass the mark of 10 kilograms per capita (Sartori & Amancio, 2012), compared to the global average per capita fish consumption, which is around 20 kg per year (Trondsen et al., 2003). Fish consumption can be influenced by socioeconomic and social factors, cultural aspects, and personal consumption patterns, which can directly impact the amount of fish consumed by individuals (Trondsen et al., 2003). For decades, fish consumption levels in Brazil have remained below the global average, particularly in the southern and southeastern regions. The dissemination of knowledge about the nutritional benefits of fish consumption could significantly contribute to increasing this index (Rebelatto et al., 2022; Sartori & Amancio, 2012).

However, fish is a highly perishable food due to its high free water content, which accelerates bacterial action in its muscle tissue. After slaughter, a series of chemical, biochemical, and microbiological changes begin, which determine the degree of freshness of the fish. (Bito et al., 1983; Gonçalves, 2011; Minozzo, 2011).

The assessment of fish quality and freshness can be determined through sensory, physicochemical, and microbiological methods. However, due to the subjectivity of analyses, delays in results, and high costs, other methodologies have gained prominence, such as rigor mortis (Presenza et al., 2021). This method is based on muscle contraction and the loss of the elastic capacity of fish muscle. Using simple materials and an easy evaluation process, it is possible to determine the quality and freshness of the fish in question (Juliana Antunes, 2017).

In the initial phase, also categorized as pre-rigor, the fish's musculature remains flaccid for varying periods depending on thermal and intrinsic characteristics. The second phase, known as rigor mortis, is characterized by muscle stiffness and a reduction in the characteristic fish odor. The duration of this phase is determined both by the environmental characteristics of the storage location and by the slaughter method used during the capture of the fish. However, muscle conditions change over time, making the musculature flaccid again. This third phase is known as post-rigor. In the post-rigor phase, conditions favor microbial growth, which, combined with chemical reactions, become perceptible both in physical and sensory aspects (Nunes et al., 2007).

Fish has high nutritional value and is an extremely perishable product. Therefore, ensuring the commercialization of raw materials that are safe for consumption is essential in the fishery production chain. Consequently, understanding the physicochemical and biological changes in fish before subjecting it to any processing or commercialization is of vital importance. From this perspective, the present study aimed to observe and calculate the rigor mortis index of Carapeba in order to assess the potential shelf life of this fish's derivatives.

II. METHODOLOGY

For the evaluation of the rigor index, three specimes of carapeba *(Eugerres brasilianus)* were selected. These specimens were collected throug beach seine fishing conducted in Itaipava (Fig 1), located in the municipality of Itapemirim, in the southern region of the state of Espírito Santo (Fig 2).

Fig.1: Record of Beach Seine Fishing Activity being carried out in the municipality of Itaipava, ES.

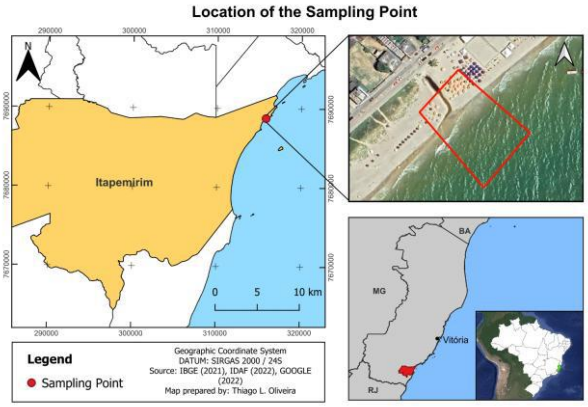

Fig.2: Geographical Location of the Collection Point.

The collected individuals were removed alive from the net and immediately placed on ice for transport to the Fish Processing Laboratory at the Federal Institute of Espírito Santo, in Piúma, a municipality bordering Itapemirim (SISBIO: 87028-2). The icing process was carried out at approximately 9:20 a.m., and the rigor analysis process

began at 10:00 a.m. The individuals were identified as P1, P2, and P3 (Fig 3).

Fig.3: Eugerres brasilianus specimens arranged on the bench, with a square ruler used for measurements beside them. From left to right, the individuals P1, P2, and P3 are displayed, respectively.

The specimens were placed on an aluminum bench, and using a square ruler (Figure 3), the initial measurement of each specimen's length was taken. These measurements continued to be taken every 20 minutes.

The evaluation of the rigor index was conducted using a methodology adapted from Bito et al.(1983), positioning the square ruler beside the fish on a horizontal table, with half of its body (the tail section) suspended beyond the edge of the table. At 20-minute intervals, the rigor index was measured using equation 1.

Rigor Index (%) = [(D0 – Dt)/ D0] x 100 (1).

Where D_0 is the distance between the base of the caudal fin and the reference point immediately after death, and D_t is the distance between the base of the caudal fin and the reference point measured at the predetermined time intervals, which in this study were set at every 20 minutes. The experiment lasted approximately 30 hours. Ambient temperature measurement was not conducted, as the experiment took place in a climate-controlled environment with an average temperature of 23°C.

The rigor mortis index values were analyzed using the statistical software JASP (version 0.18.3.0). P1, P2, and P3 were subjected to an Analysis of Variance (ANOVA) test, and the samples were compared using Tukey's method at a 5% significance level.

III. RESULTS AND DISCUSSIONS

The rigor mortis stage was first observed in samples P2 and P3, 4.3 hours after slaughter, while sample P1 reached this stage one hour later than the others (Fig 3). Regarding the duration of full rigor, a difference between sample P1 and the others was again observed. P2 and P3 remained in full rigor for 18.7 and 16.7 hours, respectively, while P1 remained in this stage for only 40 minutes.

Based on the above findings, when analyzing the organoleptic factors of the fish, the first visual signs of decomposition began to appear at 23 hours into the experiment. The fish became opaque, with a concave eye appearance, dry skin, and a foul odor, no longer meeting the ideal conditions for commercialization.

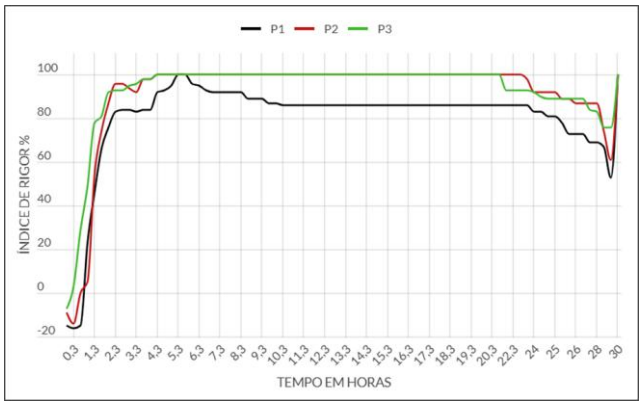

Fig.4: Rigor Mortis Index (%) Over Time for Eugerres brasilianus (Carapeba).

According to the analysis of variance at a 5% significance level, the mean of sample P1 compared to P2 and P3 showed a significant difference, while no difference was observed between P2 and P3. Considering that a p-value less than 0.05 indicates a significant difference between the means of the analyzed samples, otherwise, the difference between the means is considered negligible (Table 1). Tabela 1 - Análise comparativa das amostras de acordo com o teste de Tukey.

Table. 1: Comparative Analysis of Samples According to the Tukey Test.

Comparison		Mean Difference	SE	t	p_{tukey}
P1	P2	-10.894	3.415	-3.190	0.005
P1	P3	-12.322	3.415	-3.609	0.001
P2	P3	-1.429	3.415	-0.418	0.908

Note: Adjusted p-value for a family of 3.

Correlating the fact that the Carapeba was captured alive and immediately placed on ice, the autolysis process was significantly reduced, as after capture, the organism undergoes a series of biochemical, physical, and

microbiological changes driven by enzymatic and bacterial actions (Gonçalves, 2011; Medeiros et al., 2024).

The concentration of ATP in the post-mortem muscle and muscle contraction are decisive factors for observing the changes in fish, with rigor mortis being the stage where muscle stiffness has already occurred due to the lack of energy reserves for muscle activity. Because of this, this stage is crucial for extending the shelf life of the fish, especially when associated with the temperature and storage binomial (Gonçalves, 2011).

Several factors, such as sexual maturity, nutritional aspects, stress, method of slaughter, fish size, and others, influence the rigor mortis indices of a species. Statistically, sample P1 was the one that presented results divergent from the other samples.

It is essential to state that the method of capture has a direct influence on the rigor mortis index between the samples. As an active fishing technique, trawl fishing causes greater stress to the fish compared to other capture methods. In this type of fishing gear, the fish must exert significant effort to escape the net, leading to a rapid depletion of its energy reserves, significantly increasing the consumption of ATP and glycogen. This rapid energy demand increases the production of lactic acid, which consequently lowers the pH of the flesh (Academy, 2023; Gonçalves, 2011). Moura (2018) reports in his studies that Acaris bodós specimens subjected to stressful slaughter methods entered and exited the rigor mortis stage more quickly than those slaughtered through other methods. It is worth noting that all samples were subjected to the same capture method, meaning that stress cannot be considered the sole hypothesis for sample P1 deviating so much from the others.

However, the stress factor cannot be overlooked in this study. Mendes et al. (2015) demonstrated through their experiments that *Colossoma macropomum* specimens subjected to slaughter methods after a certain recovery period showed a delayed onset of rigor mortis compared to those subjected to stressful slaughter methods. Therefore, the importance of the capture method for the target species cannot be ignored, as the physiological stress load to which the species is subjected is extremely high when struggling or exerting effort to escape capture. Although each individual may have different responses to stressful stimuli, intrinsic factors such as nutritional, reproductive aspects, and the habitat in which the organism is situated contribute to changes in the post-mortem rigor index.

IV. CONCLUSION

The species *Eugerres brasilianus* (Couvier, 1830) remained in full rigor for an average of 12 hours, indicating a greater resistance of the fish to deterioration. Thus, it is a species with significant conservation potential, which opens up a range of possible studies for its conservation and processing methods.

More studies are needed regarding rigor mortis in this species, as its behavior when subjected to less stressful slaughter methods is still unknown. Therefore, it is recommended that future studies conduct analyses with greater detail on the post-mortem biochemical changes in the fish, aiming to understand the behavior of the rigor index in this species when subjected to other slaughter conditions. This study highlights the potential factors affecting the quality and shelf life of Carapeba meat.

ACKNOWLEDGEMENTS

We extend our deepest and most respectful gratitude to the Federal Institute of Espírito Santo – Piúma Campus, for its invaluable institutional support, academic excellence, and intellectually stimulating environment that greatly contributed to the successful development of this research. We are sincerely grateful for the dedication of the faculty, the support provided by the technical staff, and the infrastructure made available, all of which were essential to the accomplishment of this work. Our heartfelt appreciation goes to everyone who, directly or indirectly, contributed to this achievement.

REFERENCES

[1] Academy, A. F. (2023, abril 28). QUALIDADE E SEGURANÇA DO PESCADO: REVISÃO. *Agron Food Academy*. https://agronfoodacademy.com/qualidade-e-seguranca-do-pescado-revisao/

[2] Bito, M., Yamada, K., Mikumo, Y., & Amano, K. (1983). *Studies on rigor mortis of fish, 1: Difference in the mode of rigor mortis among some varieties of fish [17 species marine fishes] by modified Cutting's method.* https://www.semanticscholar.org/paper/Studies-on-rigor-mortis-of-fish%2C-1%3A-Difference-in-Bito-Yamada/adc987e322d6d0c0b05e1eac6837a9cfa96741ed

[3] FAO. (2024). *The State of World Fisheries and Aquaculture 2024*. FAO ; https://openknowledge.fao.org/handle/20.500.14283/cd0683en

[4] Gonçalves, A. A. (2011). *Tecnologia do pescado: Ciência, tecnologia, inovação e legislação*.

[5] Juliana Antunes, G. (2017). *Qualidade e processamento de pescado* (M. OETTERER, Org.). Elsevier.

[6] Medeiros, E. S. D., Gonzaga, M. G. D. S., Cordeiro, I. L. M., Almeida, E. P. M., Ferreira, L. B. B., Guimarães, A. K. V.,

Costa, G. D. A., & Otani, F. S. (2024). FATORES DE DETERIORAÇÃO FÍSICO-QUÍMICA E CONSERVAÇÃO POR SALGA EM PEIXE: REVISÃO DE LITERATURA. Em *Ciência e Tecnologia do Pescado: Tópicos atuais em pesquisa—Volume 3* (1º ed, p. 26–43). Editora Científica Digital. https://doi.org/10.37885/240516693

[7] Mendes, J. M., Inoue, L. A. K. A., & Jesus, R. S. (2015). Influência do estresse causado pelo transporte e método de abate sobre o *rigor mortis* do tambaqui *(Colossoma macropomum)*. *Brazilian Journal of Food Technology*, *18*, 162–169. https://doi.org/10.1590/1981-6723.1115

[8] Minozzo, M. G. (2011). *Processamento e Conservação do Pescado*.

[9] Moura, M. L. A., Cunha, F. T., Macedo, H. J. A. de, Batista, J. D. D. O., Reis, S. M., Oliveira, S. S., & Otani, F. S. (2018). RIGOR MORTIS E ASPECTOS REPRODUTIVOS DE ACARIS BODÓS CAPTURADOS NO RIO TAPAJÓS, PARÁ, BRASIL. *Revista Agroecossistemas*, *10*(2), Artigo 2. https://doi.org/10.18542/ragros.v10i2.5170

[10] Nunes, M. L., Irineu, B., & Cardoso, C. (2007). Aplicação do índice de qualidade (QIM) na avaliação da frescura do pescado. *Publicações Avulsas do IPIMAR*, *Nº15*. https://comum.rcaap.pt/handle/10400.26/33873

[11] Presenza, L., Dos Santos, A. S., França Silva, A. C., Bernabé, C. V., Fonseca Ferreira, J. V., Caixeta Dayrell, L., Paiva Garcia, R. C. D., David Lavander, H., & Minozzo, M. G. (2021). Rigor Index of juvenile cobia (Rachycentron canadum): Study with anesthesia (eugenol) and hypothermia. *International Journal of Advanced Engineering Research and Science*, *8*(4), 123–127. https://doi.org/10.22161/ijaers.84.14

[12] Rebelatto, I. D. S., Lintzmaia, D. J. H., Ritter, D. O., Lanzarin, M., Faria, R. A. P. G., & Chitarra, G. S. (2022). COMPOSIÇÃO QUIMÍCA E VALOR NUTRICIONAL DO PESCADO. Em C. A. M. Cordeiro, D. D. S. Sampaio, & F. C. A. F. Holanda, *Engenharia de Pesca: Aspectos teóricos e práticos—Volume 4* (1º ed, p. 50–66). Editora Científica Digital. https://doi.org/10.37885/220408711

[13] Sartori, A. G. de O., & Amancio, R. D. (2012). Pescado: Importância nutricional e consumo no Brasil. *Segurança Alimentar e Nutricional*, *19*(2), Artigo 2. https://doi.org/10.20396/san.v19i2.8634613

[14] Trondsen, T., Scholderer, J., Lund, E., & Eggen, A. E. (2003). Perceived barriers to consumption of fish among Norwegian women. *Appetite*, *41*(3), 301–314. https://doi.org/10.1016/s0195-6663(03)00108-9

International Journal of Advanced Engineering Research and Science (IJAERS)
Peer-Reviewed Journal
ISSN: 2349-6495(P) | 2456-1908(O)
Vol-12, Issue-5; May, 2025
Journal Home Page Available: https://ijaers.com/
Article DOI: https://dx.doi.org/10.22161/ijaers.125.2

Culture of Innovation: The Impact on the Day-to-Day of an Organization

Bruno Tadeu Ferreira da Silva[1], Alexandre Acácio de Andrade[2], Anderson Orzari Ribeiro[3]

[1]Graduate Program in Engineering and Innovation Management, Federal University of ABC , UFABC, Brazil
Email: brn.tadeu@gmail.com
[2]Center for Engineering, Modeling and Applied Social Sciences, Federal University of ABC , UFABC, Brazil
Email : aacacio@ufabc.edu.br
[3]Center for Engineering, Modeling and Applied Social Sciences, Federal University of ABC , UFABC, Brazil
Email : anderson.ribeiro@ufabc.edu.br

Received: 03 Apr 2025,

Receive in revised form: 02 May 2025,

Accepted: 07 May 2025,

Available online: 13 May 2025

***Keywords*— Competitiveness, Culture of Innovation, Innovation Hubs, Organizational Management, Innovation Strategy.**

***Abstract*—** *This study analyzes stakeholders' perceptions of the culture of innovation in an organization in the Greater ABC region linked to an Innovation Hub. The research adopts an exploratory approach, using qualitative and quantitative methods, with data collection carried out through employee questionnaires and interviews with managers. The results show that, although innovation is recognized as essential, there are challenges in integrating this culture, in training employees, and in strategic alignment with the Hub. The study concludes that it is necessary to strengthen support mechanisms and promote greater internal cohesion to ensure that innovation becomes a consistent practice within the organization.*

I. INTRODUCTION

The culture of innovation is a crucial element for the success and sustainability of organizations in a competitive and dynamic environment. The capacity for innovation is not limited to the development of new products or services, but includes the implementation of new processes, business models and management methods that promote a sustainable competitive advantage [1].

The authors [2] state that a solid organizational culture, which values creativity and flexibility, is essential to foster an innovative environment. However, many organizations face challenges in establishing a culture of innovation due to barriers such as resistance to change and lack of adequate incentives [3]. In addition, research by [4] suggests that the organizational structure must be flexible to allow rapid adaptation to market changes and the implementation of new ideas.

The general objective of this study is to analyze the perception of those involved and impacted on the Culture of Innovation of an organization in the Greater ABC region of São Paulo, Brazil, which has a link with an Innovation Hub.

The concept of culture proposes that there is structural stability, depth, extension and patterns or integrations, indicating that culture is a learned phenomenon, in the same way that character and personality are for each of us [5].

Some studies indicate that the role of culture is critical and fundamental for organizations and that it is considered one of the determining factors of success or even failure [6].

Organizational culture, according to [7], is a form of sociocultural system, in which the social and structural components are closely connected to the symbolic and ideological issue of the organization.

Within the scope of organizational culture, the authors [8] indicate that organizational behavior is a field of study that attempts to explain, predict and even modify human behavior within the context of organizational culture, but

there are three considerations that are necessary for organizational behavior, which are:

• It aims at observable behaviors, such as the use of equipment, way of speaking in meetings, how to write a report. It also deals with people's internal states, for example, how to think, decide and perceive which issues that accompany an observable action are.

• It also evaluates the relationship and behavior of groups among themselves, since people, groups and organizations do not behave in the same way. In this way, events can occur within the organization that we cannot explain solely as a result of an individual's behavior, for example. It is necessary to evaluate from a group or organizational perspective.

• Therefore, it is always necessary to analyze the behavior of people as individuals, as members of groups and of the organization.

For the concept of innovation, one of the main points is that people understand the concept in different ways, usually confusing it with invention, since the term innovation derives from the Latin - innovare, which means "to do something new", but the concept for innovation is a process of transforming opportunities into new ideas to be taken advantage of and used by society [9].

Innovation is a process in which a product or service is created, renewed or updated with the introduction of new techniques or ideas to generate value for the consumer and organization. In this way, innovation ceases to have an optional role and is seen as a protagonist [10].

In closed innovation, organizations carry out the process internally without external contact, only with restricted knowledge [11].

For [12], success in the closed innovation process requires control, in which organizations must generate their own ideas, then develop, distribute, serve, finance and support them.

According to [13], in open innovation there are activities carried out internally and others carried out with external partners, showing that in this model organizations do not innovate in isolation, as the organization is inserted in the environment and society and therefore depends on external knowledge to create something innovative for the market. In the open innovation model, a concept attributed to Henry Chesbrough, the organization carries out the process collaboratively with other companies, universities and even consumers [11]. One of these models are innovation hubs, which according to [14], are essential for the implementation of smart specialization strategies, especially in European regions. A key element of the initiative is the innovation hubs that act as ‘one-stop-shops’ where small and medium-sized enterprises (SMEs) can test the latest digital technologies and obtain training, financial advice, market intelligence and networking opportunities to improve their businesses through digital innovations. This is exemplified by figure 1 where one can see, schematically, the Catalan innovation hub [15].

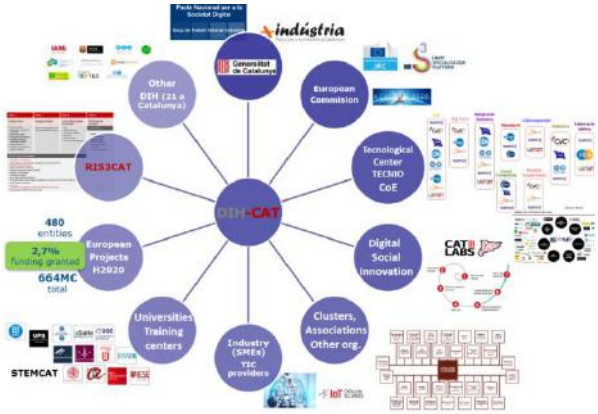

Fig. 1: Catalan Ecosystem and DIH

Source: [15]

Innovation hubs offer numerous benefits to their users. Among the advantages are the dissemination of knowledge, entrepreneurship and technologies, which occur through courses, workshops and lectures, often taught by the startups that are part of the hub [16].

According to the report by [17], innovation hubs stand out for their agglomeration capacity, where geographic proximity and the density of talents and resources create synergies that accelerate the innovation process.

Innovation hubs create an ecosystem where startups, large corporations, universities and investors can interact and collaborate. This collaboration facilitates the exchange of knowledge and resources, promoting synergies that can result in significant innovations [18].

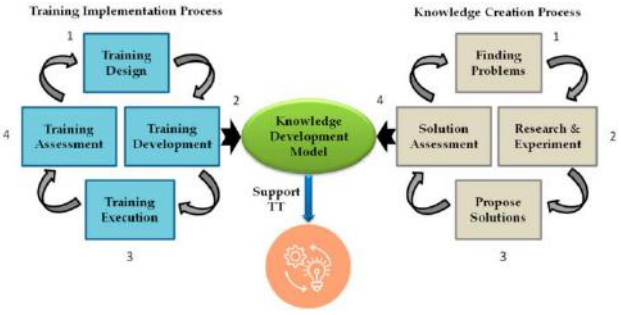

Fig.2 – Knowledge Development Model

Source: [15]

For [19], innovation hubs function as regional laboratories for technology businesses and entrepreneurs, exploring the concept of a "regulatory sandbox" as an

extension of the public policy environment to foster technology entrepreneurship.

Furthermore, research by [15] proposes a generic and flexible learning framework to assist digital innovation hubs in offering education, training and learning services that support the transfer of digital technology to companies, this proposal is shown in figure 2.

According to [20], as Innovation Hubs expand and reinforce the innovation ecosystem, they are considered as ecosystems of agents involved in digitalization, transforming themselves into platforms for testing advanced digital technologies.

Hubs, for [21], are in practice relational spaces, created amid interactions between global power structures, regional configurations, local cultural contexts, daily lived experiences of communities and individuals, among other things. Hubs should be studied as positioned in their local contexts.

II. METHODOLOGY

With the aim of analyzing the perception of those involved and impacted on the Culture of Innovation of an organization in the Greater ABC region of São Paulo-Brazil, which has a link with an Innovation Hub, this research will adopt an exploratory approach by case study in a qualitative and quantitative manner, with a non-probabilistic sample.

According to [22], exploratory research is conducted with the purpose of offering a preliminary overview of a given phenomenon.

Exploratory research is especially valuable for obtaining initial ideas and developing a preliminary understanding of the research problem, assisting in the formulation of hypotheses and in the development of a more structured research design for subsequent studies[23].

According to [24], the case study can include quantitative elements, as well as details. And it is not just a form of qualitative research, the use of quantitative and qualitative data together with the need to define a “case” are just some of the ways to demonstrate that the case study goes far beyond qualitative research.

For [25], non-probabilistic samples are constituted accidentally or intentionally, without the random selection of elements..

For this study, the population will be from an organization in the retail sector: The retail group was founded in 1952 by a Polish immigrant who arrived in Brazil after World War II. Initially, he worked as a peddler, selling products door-to-door, mainly to people who were leaving a certain region of Brazil, which inspired the company's name. In 1957, he opened the first physical store in São Caetano do Sul, São Paulo [26]. Another part of the population will be considered from the Innovation Hub, with which the organization has a partnership: The innovation company was founded in 2018, with the objective of fostering the innovation ecosystem in Latin America. Initially, it operated through three physical hubs with acceleration programs for startups, quickly becoming a reference in the technology and innovation market [27].

For quantitative data collection, a 10-question scaled questionnaire was conducted with the organization's employees. According to [28], a questionnaire is a data collection technique characterized by the application of a structured set of questions to a specific group of individuals. In this case, the Likert scale was used, as according to [29], Likert scales are commonly used to measure attitudes and perceptions, providing a range of responses to a given question or statement.

For qualitative data collection, structured interviews were conducted using a 9-question form with the manager of the Innovation Hub and the innovation area of the organization. According to [25], interviews can be exploratory or used to obtain data. While exploratory interviews are relatively structured, interviews for collecting information are highly structured.

III. RESULTS AND DISCUSSION

Statistics is a widely used tool that allows researchers to not only describe data, but also to evaluate new possibilities for relationships and perform future analyses based on this information, providing valuable findings, and supporting research conclusions [30]. Frequency distribution involves organizing a set of data into classes or categories and counting the number of occurrences, the frequencies, within each class. This method allows researchers to identify patterns and trends in the data, which is essential for more in-depth analyses [31].

The responses showed a general tendency to concentrate on intermediate values (Neutral and Agree). This may suggest that most respondents partially agree with the statements about the culture of innovation, although it may suggest that some employees may not be fully aware of or involved with the company's innovation issues, with a variability in perception.

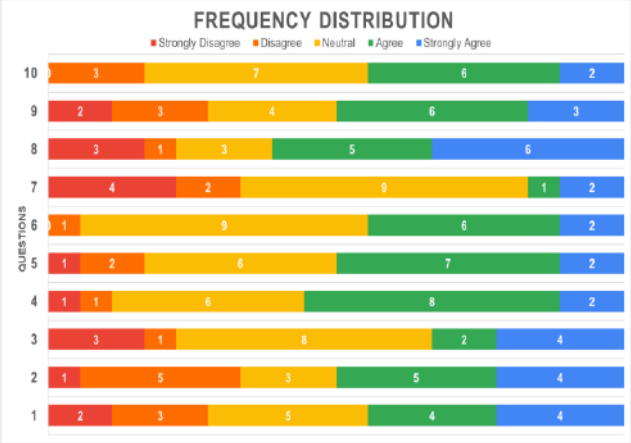

Fig.3 – Distribution of quantitative questionnaire responses

Table.1: – Table of mean and standard deviation of Responses

#	Theme	Questions	Mean	Standard Deviation
1	Innovation Processes	The organization I work for has an Innovation Department/Center structured with innovation models and processes.	3.28	1.32
2	Innovation Ecosystem	The organization I work for has partnerships with Innovation Hubs/Research and Development institutions.	3.33	1.28
3	Innovation Ecosystem	The organization I work for has startup acceleration or incubation programs.	3.17	1.34
4	Innovation Processes	The organization I work for has a long-term vision to remain or become a leader in the sector through innovation.	3.50	0.99
5	Innovation Culture	The organization I work for understands that innovative projects involve risks and knows how to deal with these risks and likely failures.	3.39	1.04
6	Innovation Culture	The latest innovations launched by the organization I work for have achieved great results in the market.	3.50	0.79
7	Innovation Processes	The organization I work for has a history of patents and intellectual property in the market.	2.72	1.23
8	Innovation Culture	The organization I work for encourages a culture of innovation among its employees.	3.56	1.46
9	Innovation Culture	The organization I work for constantly invests in emerging technologies and market trends.	3.28	1.27
10	Innovation Processes	The organization I work for can quickly adapt to market changes and new demands from our consumers.	3.39	0.92

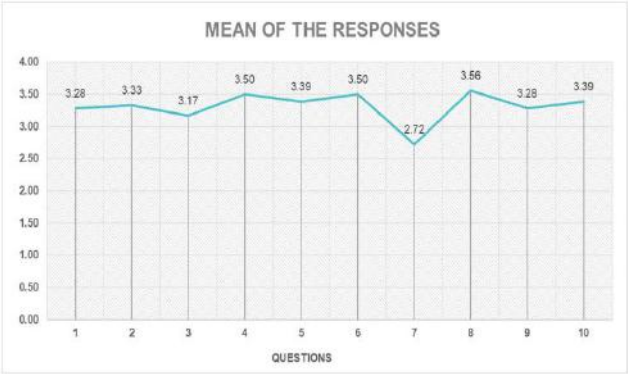

Fig.4 – Mean of the responses.

The mean and standard deviation of these responses were also analyzed. The mean, according to [31], represents the sum of all values in a data set divided by the total number of observations. For [32], the standard deviation indicates how dispersed the values of a data set are in relation to the mean, providing information about the variability of the data.

The averages for the questions range from 2.72 to 3.56, indicating that the perception of the participants is more mixed. While some areas are seen more positively (average of 3.56), other areas have a more neutral or even slightly negative perception.

The average of 3.56, observed in one of the questions, suggests that this specific area is seen more positively, which may indicate a certain degree of acceptance or alignment with innovative practices.

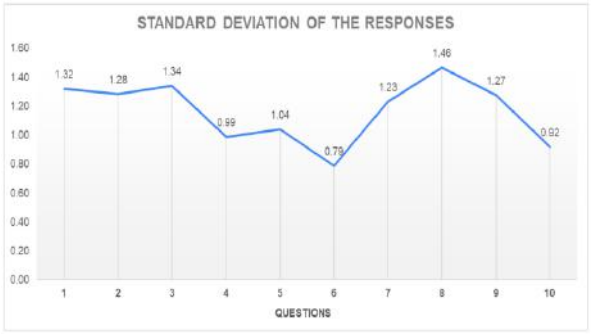

Fig.5 – Standard deviation of the responses.

Standard deviations range from 0.79 to 1.46, indicating that although the overall perception is slightly positive, there is significant variation in employee perceptions.

A higher standard deviation (1.46) suggests that there is considerable diversity of perceptions in certain areas, which may point to differences in the experience, understanding, or perception of innovation culture among employees.

The combination of slightly positive means with significant standard deviations suggests that although the majority of employees have a positive view of innovation culture, there is still considerable variability in perceptions.

According to [33], while the mean provides a central measure of the data, the standard deviation complements this information by indicating the consistency of the data in relation to the mean. This combination is essential for the interpretation of research results, as it allows researchers to understand both the typical value and the variability of the data.

For the qualitative data, a thematic content analysis was carried out, according to [23] qualitative interpretation is a reflective process that demands the researcher to construct

complex meanings from the data, needing to take into account the theoretical and practical context of the research.

Table.2- Interview Question Guide

Theme	Questions
Innovation Culture	8. What training or development programs are offered to support the dissemination of innovation within the organization?
	9. How are employees who significantly contribute to the dissemination of innovation recognized and rewarded?
	5. What is the role of executive leadership in supporting innovation and the innovation hub?
Innovation Ecosystem	1. What are the main objectives of an innovation hub in its relationship with the company?
	2. What are the main benefits that an innovation hub can bring to the company?
	7. How does the innovation hub collaborate with other areas of the company?
Innovation Processes	3. What are the criteria for selecting projects or ideas to be developed within the innovation hub?
	4. What metrics are used to measure the success and impact of innovation initiatives in the hub?
	6. How does the hub engage and motivate employees to actively participate in the innovation process?

Regarding the topic of innovation culture, in the interviewees' view, innovation training in the organization is treated as a complementary and informative activity, but it is not yet fully integrated as a structured part of the innovation strategy. There is a disconnection between recognition and reward for participants in the innovation culture. Although recognition exists, it is not fully structured or financially incentivized in a comprehensive manner, which can limit employees' motivation to engage in innovation initiatives. The role of executive leadership is fundamental to the success of innovation, but there is a need to maintain engagement in the long term. Innovation requires committed leadership that promotes a culture of calculated risk and continuous learning.

As with the innovation process, the interviewees analyzed the evolution of selection criteria as reflecting the company's adaptation to market demands and its own maturity. The initial lack of criteria may have generated inefficiencies, but the introduction of governance shows an effort to structure the innovation process. Likewise, the decentralization of knowledge and the promotion of a critical culture are important steps to engage employees. However, there was no clear strategy to ensure that all employees were aligned and motivated to actively participate in the innovation process.

In the ecosystem theme, interviewees indicated that collaboration is seen as a key to the success of innovation initiatives. Integrating the Hub with other areas of the company allows for an exchange of knowledge and perspectives, which is essential for effective innovation. However, the effectiveness of this collaboration depends on engagement and communication between areas. The Innovation Hub offers both tangible and intangible benefits. It not only improves processes and strategies, but also promotes a cultural change that values continuous learning and innovation. However, to maximize these benefits, a coordinated effort between the Hub and the organization is necessary.

IV. CONCLUSION

This study investigated the perception of those involved and impacted on the Culture of Innovation in an organization in the Greater ABC region, linked to an Innovation Hub. The combined analysis of quantitative and qualitative data revealed valuable insights into how participants perceive the different aspects of the culture of innovation in the organization.

Participants demonstrated an understanding of the importance of the culture of innovation, recognizing it as fundamental to the success and competitiveness of the organization. However, there is a perception that support mechanisms, such as training, recognition and incentives, are not sufficiently structured or integrated to promote a culture of innovation effectively, and there was notable variability in perceptions. Participants indicated that leadership needs to play a more active role in promoting a culture of innovation, creating an environment where creativity and experimentation are encouraged and rewarded. At times, there was even a slightly negative perception of innovation processes, which may indicate that they are not uniformly understood or applied within the organization. In summary, the participants' perception suggests that, although the organization is on the right track in adopting innovative practices and connecting with an Innovation Hub, there is still work to be done to ensure that the culture of innovation is fully integrated, communicated and supported at all levels. Future initiatives should focus on aligning the objectives between the Hub and the organization, as well as strengthening the internal mechanisms that support and encourage a culture of innovation, such as training, recognition and success metrics. Leadership plays a crucial role in transforming this perception into action, ensuring that the culture of innovation becomes an intrinsic part of the organization's day-to-day activities.

ACKNOWLEDGEMENTS

The authors would like to thank the Master's program in Innovation Management Engineering at UFABC for their support.

REFERENCES

[1] Aithal, R. K. (2015). Book essay on Unrelenting Innovation: How to create a culture for market dominance. Journal of Business Research, 68(2), 322-325. https://doi.org/10.1016/j.jbusres.2014.07.001

[2] Barale, R. F., & Santos, B. R. D. (2017). Cultura organizacional: una revisión sistemática de la literatura. Revista Psicologia Organizações e Trabalho, 17(2), 129-136.. https://doi. org/10.17652/rpot/2017.2. 12854.

[3] Bessi, V. G. (2015). Estudo da inovação e da cultura organizacional em indústrias de pequeno e médio porte da região do Vale do Rio dos Sinos, no Rio Grande do Sul. Gestão & Planejamento-G&P, 16(2).

[4] Bock, A. J., Opsahl, T., George, G., & Gann, D. M. (2012). The effects of culture and structure on strategic flexibility during business model innovation. Journal of Management studies, 49(2), 279-305. https://doi.org/10.1111/j.1467-6486.2011.01030.x

[5] Schein, E. H. (2009). Cultura organizacional e liderança. São Paulo: Atlas.

[6] Cameron, K. S. (2011). Diagnosing and changing organizational culture: Based on the competing values framework.

[7] Allaire, Y., & Firsirotu, M. E. (1984). Theories of organizational culture. Organization studies, 5(3), 193-226. https://doi.org/10.1177/017084068400500301

[8] Wagner III, J. A., & Hollenbeck, J. R. (2020). Comportamento organizacional. Saraiva Educação SA.

[9] Tidd, J., & Bessant, J. (2015). Gestão da inovação-5. Bookman Editora.

[10] Freitas, A., Riascos, L., Andrade, A., Faco, J., & Gallotta, B. (2021). Innovation in small & medium enterprises in São Paulo. http://dx.doi.org/10.46254/SA02.20210160.

[11] Da Silva, E. L., & Pinheiro, L. V. (2014). O Brasil e as pesquisas em inovação aberta: Um estudo a partir dos Grupos de Pesquisa do CNPq | Open innovation research in Brazil: a study on CNPq Research Groups. Liinc em revista, 10(2). https://doi.org/10.18617/liinc.v10i2.727

[12] Chesbrough, H. W. (2003). Open innovation: The new imperative for creating and profiting from technology. Harvard Business Press.

[13] Christensen, J. F., Olesen, M. H., & Kjær, J. S. (2005). The industrial dynamics of Open Innovation—Evidence from the transformation of consumer electronics. Research policy, 34(10), 1533-1549. https://doi.org/10.1016/j.respol.2005.07.002

[14] Rissola, G., & Sörvik, J. (2018). Digital innovation hubs in smart specialisation strategies. Publications Office of the European Union, Luxembourg. https://dx.doi.org/10.2760/475335

[15] Sarraipa, J., Zamiri, M., Marcelino-Jesus, E., Artifice, A., Jardim-Goncalves, R., & Moalla, N. (2023). A learning framework for supporting Digital Innovation Hubs. Computers, 12(6), 122. https://doi.org/10.3390/computers12060122

[16] Rosolem, A. M. (2024). Identificação dos pré-requisitos para a abertura de um hub de inovação: avaliação da aptidão do município de Jaboticabal–SP. https://hdl.handle.net/11449/258531

[17] Nature. Nature Research Intelligence. Nature Portfolio. Available in: https://www.nature.com/articles/d42473-023-00420-1. Accessed: May. 2025.

[18] Bittencourt, B. A., Helale, J., Visentini, A. L. F., & Martins, B. W. (2025). The role of individual orchestrators of innovation hubs: A multiple case study in the south of Brazil. International Journal of Innovation, 13(1). https://doi.org/10.5585/2025.27160

[19] Hemphill, T. A. (2023). Technology entrepreneurship and innovation hubs: Perspectives on the universal regulatory sandbox. Science and Public Policy, 50(2), 350-353. https://doi.org/10.1093/scipol/scac072

[20] Georgescu, A., Avasilcai, S., & Peter, M. K. (2021). Digital Innovation Hubs—The present future of collaborative research, business and marketing development opportunities. In Marketing and Smart Technologies: Proceedings of ICMarkTech 2020 (pp. 363-374). Singapore: Springer Singapore. https://doi.org/10.1007/978-981-33-4183-8_29

[21] Jiménez, A., & Zheng, Y. (2021). Unpacking the multiple spaces of innovation hubs. The Information Society, 37(3), 163-176. https://doi.org/10.1080/01972243.2021.1897913

[22] Gil, A. C. (2002). Como elaborar projetos de pesquisa (Vol. 4, p. 175). São Paulo: Atlas.

[23] Creswell, J. W. (2014). Investigação Qualitativa e Projeto de Pesquisa-: Escolhendo entre Cinco Abordagens. Penso Editora.

[24] Yin, R. K. (2015). Estudo de Caso-: Planejamento e métodos. Bookman editora.

[25] Prodanov, C. C., & De Freitas, E. C. (2013). Metodologia do trabalho científico: métodos e técnicas da pesquisa e do trabalho acadêmico-2ª Edição. Editora Feevale.

[26] HPG. Available at: https://hpg.com.br/historia-das-casas-bahia-quem-e-o-dono-ministro-e-curiosidades.html. Accessed: May 2025.

[27] DISTRITO.ME. Who We Are. Available at: https://distrito.me/quem-somos/. Accessed: May 2025.

[28] De Brito, L. (2012). Pequeno guia de inquérito por questionário. IESE. https://tinyurl.com/yc24h84j

[29] Jamieson, S. (2004). Likert scales: How to (ab) use them?. Medical education, 38(12), 1217-1218.

[30] Field, A. (2020). Descobrindo a estatística usando o SPSS-5. Penso Editora.

[31] Triola, M. F. (2008). Introdução à estatística. In Introdução à estatística (pp. xxvi-310).

[32] Malhotra, N. K. (2019). Pesquisa de Marketing-: uma orientação aplicada. Bookman Editora.

[33] Morettin, P. A., & Bussab, W. D. O. (2023). Estatística básica. ISBN: 9786587958491

International Journal of Advanced Engineering Research and Science (IJAERS)
Peer-Reviewed Journal
ISSN: 2349-6495(P) | 2456-1908(O)
Vol-12, Issue-5; May, 2025
Journal Home Page Available: https://ijaers.com/
Article DOI: https://dx.doi.org/10.22161/ijaers.125.3

DreamTalk-DMT: A Lightweight Sparse Mechanism Model with Dynamic Thresholds

Jia Zhang[1,*], Lin Po Shang[2]

[1]Department of Electronic Information Engineering, Electronic Information Science and Technology major, Guangdong University of Petrochemical Technology, China
[2]Department of Energy and Power Engineering, Process Equipment and Control Engineering major, Guangdong University of Petrochemical Technology, China
*Corresponding author:19578022107@163.com

Received: 11 Apr 2025,

Receive in revised form: 09 May 2025,

Accepted: 15 May 2025,

Available online: 20 May 2025

***Keywords*— Diffusion model; Dynamic threshold sparsification; Mutual information constrained optimization; Decoupled decoder; Cross-modal feature fusion module**

***Abstract*—** *Aiming at the shortcomings of the DreamTalk 2D digital human synthesis model in computational efficiency and expression generation fineness, this paper proposes an optimization method combining adaptive sparsity and cross-modal feature enhancement. By introducing a dynamic threshold sparsity mechanism into the diffusion model, the sparsity ratio was dynamically adjusted based on the learnable threshold and Exponential Moving Average (EMA), and the Mutual information Constraint (MI Constraint) was combined to minimize the information loss, which reduced the calculation amount of the model while retaining key features. The model architecture is improved, and the decoupled decoder is designed to decompose the facial expression into the upper and lower regions for independent processing. The dynamic linear layer is combined to realize parameter adaptation under the style condition, and the detail expression of expression generation is improved. In addition, Tacotron speech features and Wav2Vec acoustic features are fused to enhance the synchronization of speech and expression, and skip connections are used to optimize the information transmission efficiency.*

I. INTRODUCTION

From the perspective of technology evolution, digital human synthesis technology has experienced a significant transformation from traditional methods based on physical models to data-driven deep learning methods. Initially, DaViT regress 3DMM parameters from the input image to roughly scout the shape and texture of the face. Although 3DMM provides valuable information, its linear nature limits its realism.[1] Subsequently, an innovative approach developed by Buhari et al.[2] combined graph theory and FACS to extract useful features (68 landmark points) that can distinguish between various microexpressions.[3] The development of deep learning technology, methods based on Generative Adversarial networks (GAN) have made breakthroughs in the field of image generation, such as the StarGAN-VC model, which has attracted people's attention because it can solve this problem using only a single generator. However, there is still a gap between real and converted speech.[4] Diffusion Model has aroused a new upsurge of research in the field of digital human synthesis due to its theoretical completeness and generation quality advantages. Among them, DreamTalk model, as the landmark achievement in the field of speech-driven expression synthesis, is an audio-driven framework based on two-stage diffusion, which uses emotional conditional diffusion model and lip refinement network[5] to improve facial emotional expression while maintaining high video quality. DREAM-Talk represents a major leap forward in the field of emotional conversational face generation, enabling the creation of realistic and emotionally engaged

digital human representations in a wide range of applications.[5]

Many scientific research institutions and enterprises continue to make efforts in digital generation technology and other related fields. In the direction of expression generation, VASA-1, a diffusion-based global facial dynamics and head motion generation model proposed by Microsoft Research Asia, can not only generate lip movements perfectly synchronized with audio, but also generate a large number of facial nuances and natural head movements, providing high video quality through realistic facial and head dynamics IC. Online generation of 512×512 videos at up to 40 FPS with negligible startup latency is also supported.[6]; OTAvatar[7] proposed by Ma et al., OTAvatar invert the portrait image into a motion-free identity code, and then use the identity code and motion code to modulate an efficient CNN to generate a three-plane formula volume. Finally, the image is generated by volume rendering, and the identity and motion in the latent code are decoupled by a novel anti-phase decoupling strategy. The face image is constructed based on generalized controllable three-plane rendering. In addition, the Make-A-Video model[8] launched by Meta AI tries to model the multi-modal generation of text-speech-image in a unified way. Although it shows strong potential in creative content generation, there are still technical bottlenecks in the accurate synchronization of voice and expression.

At present, in the aspect of film and television special effects, the application of digital human is more and more widely, and the fidelity of image and motion has been improved. The continuous expansion of digital human application scenarios to strong interaction fields such as real-time broadcast, virtual idol interaction, and intelligent education, the limitations of existing technologies have become increasingly prominent. Aided by the diffusion model mechanism, the DreamTalk model represents a major leap forward in the field of emotional talk face generation, enabling the creation of realistic and emotionally engaging digital human representations in a wide range of applications[9]. However, with the expansion of application scenarios and the improvement of requirements, its defects gradually appear. In terms of computational efficiency, the model parameters are dense, and in real-time interaction scenarios, the memory footprint is high and the reasoning time is long, which seriously affects the interaction fluency. For expression generation, it is difficult for a single decoder to accurately simulate the differentiated motion of the eyebrow, mouth and other regions, and synthesize expression detail distortion. In cross-modal fusion, the simple feature concatenation method cannot deeply explore the complex relationship between speech prosody and expression dynamics, and the matching degree of expression and speech emotion is not good.

To address the above technical challenges, this study proposes a dynamic threshold sparsification and decoupling generation framework based on information theory and dynamic system theory. By introducing the learnable sparse threshold and Exponential Moving Average (EMA) mechanism[10], combined with the mutual information loss function[11], the framework reduced the floating-point operation efficiency while ensuring that the key information was not lost. The decoupled decoder was designed, the facial expression space was divided into the upper and lower halves, and the dynamic linear layer was used to realize the adaptive adjustment of parameters to improve the naturalness of expression. The gated fusion module of Tacotron acoustic features and Wav2Vec speech representation is constructed, and the gradient transfer path is optimized by combining jump connection, which greatly improves the accuracy of speech-expression synchronization, and provides an innovative solution for the practical development of digital human technology.

II. DREAMTALK

In the field of speech-driven expression synthesis of digital human, DreamTalk model uses the diffusion mechanism[5], uses the Transformer-based EmoDiff network, and performs temporal denoising learning of 3D expression under the conditions of audio, portrait and emotional style, and realizes the end-to-end generation of speech to expression. Excellent results are achieved on the VoxCeleb dataset, which alleviates the mode collapse problem of traditional GAN. The diffusion mechanism adopted by the method is derived from the denoising Diffusion Probability Model (DDPM)[12], which is based on the Markov chain[13]. The data generation is realized through the process of adding Gaussian noise forward and reverse iterative denoising. Compared with traditional generative models, diffusion models have more solid theoretical foundation and stronger conditional generation ability, and have shown significant advantages in the field of multimodal generation, which provides important technical support for models such as DreamTalk. denoising diffusion probabilistic model (DDPM) is a class of generative models based on probabilistic diffusion process. In recent years, remarkable progress has been made in the field of deep learning and generative models. The core idea of diffusion model is to treat the process of data generation as a random process that gradually changes from simple distribution (e.g., Gaussian distribution) to

complex data distribution. Diffusion models usually include two processes: the Forward Diffusion Process and the Reverse Process. However, both of them are a parameterized Markov chain in nature, which has stationary property. That is, if a probability changes with time, it will tend to a stationary distribution under the action of the Markov chain, and the longer the time, the more stable the distribution will be. It was this stationarity that allowed him to gradually restore the image, given a neural network that predicted the noise.

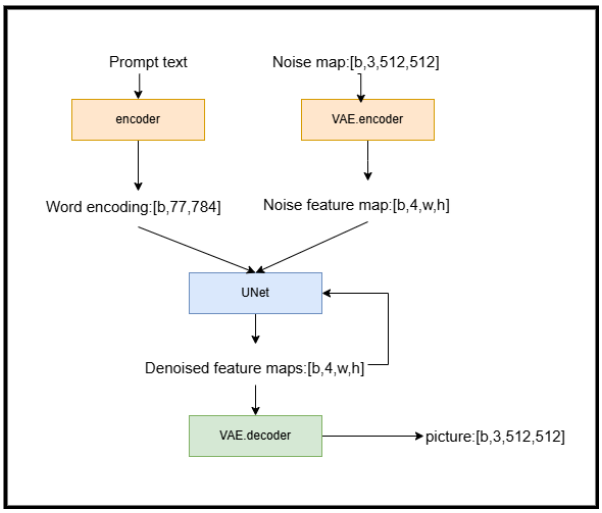

Fig.1 Diffusion Model generation process

The Forward Diffusion Process is a process that continuously adds noise to the data to be trained. The process usually starts from a simple distribution (e.g., Gaussian distribution, etc.), and through multiple rounds of small cardinality noise, the image data to be trained is closer to a complex data distribution. Meanwhile, at each step, the model predicts the noise at the next step based on the current data state and noise level, thus gradually pushing the data into a high-dimensional and complex distribution space.

In the forward process, given the initial data distribution x_0~q(x), the noise with standard deviation β_t is gradually added to the initial data according to the schedule to obtain the noise data.

$$q(x_t \mid x_{t-1}) = N(x_i; \sqrt{1-\beta_t}x_{t-1}, \beta_t I) \quad (1)$$

Where t represents the final time, as t continues to increase, the noise data gradually approaches the Gaussian distribution.

However, the efficiency of stepwise iteration based on Equation (1) is very low, and the training process consumes a lot of time. To improve the efficiency of computing, introducing the $\alpha_t = 1-\beta_t$, $\overline{\alpha_t} = \prod_{s=0}^{t} \alpha_s$, type (1) can be converted to:

$$q(x_t \mid x_0) = N\left(x_i; \sqrt{\overline{\alpha}_t}x_{01}, (1-\overline{\alpha_t})I\right) \quad (2)$$

The noisy data x_t at any time t can be obtained。

Reverse Diffusion Process is a process that gradually recovers useful information from noisy data.

The goal is to gradually recover the distribution of the original data from the pure noise state (the final result of the forward diffusion process). It is the opposite of the forward diffusion process and tries to learn how to remove the noise added at each time step so as to recover the original data.

The backward diffusion process takes advantage of the fact that the way noise is added in the forward diffusion process is known, and gradually restores the noisy data to the original data by training a neural network to predict how much noise should be subtracted at each step.In the backward diffusion process, the neural network is constructed to fit $p_\theta(x_{t-1}|x_t)$, and the original data is gradually recovered from the noise, which can be expressed as follows.

$$p_\theta(x_{t-1}|x_t) = \mathrm{N}(x_{t-1}; \mu_\theta(x_t,\mathrm{t}), \sum_\theta(x_t,\mathrm{t})) \quad (3)$$

Where θ is the neural network parameter, $\mu_\theta(x_t,\mathrm{t})$ and $\sum_\theta(x_t,\mathrm{t})$ are the mean and variance, respectively.

The training process in the diffusion model is achieved by optimizing the variational lower bound of the negative log-likelihood with p_θ. To simplify the training process, the variance of the model is set to a constant and the coefficients of the loss function are removed, so the loss function is:

$$L(\theta) = \mathbb{E}_{t,x_t,\epsilon 1}\left[\left|\left|\epsilon - \epsilon_\theta\,(x_t,t)\right|\right|^2\right] \quad (4)$$

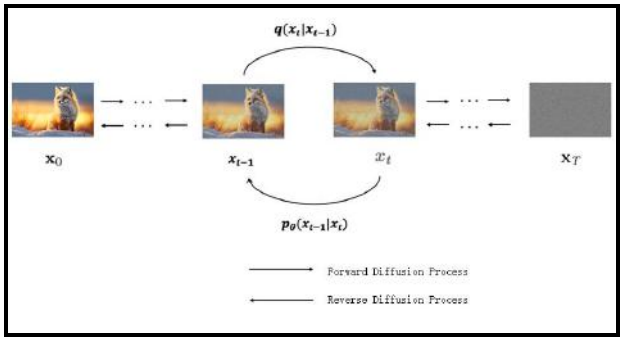

Fig.2 Diffusion Process

III. IMPROVED MODEL ARCHITECTURE AND KEY TECHNOLOGIES

Aiming at the technical bottlenecks of DreamTalk model in terms of computational efficiency, expression generation accuracy and cross-modal fusion, this study proposes a dynamic threshold sparsification-decoupling

generation framework (DTS-DG). The framework realized systematic optimization through four core modules. At the level of efficiency optimization, the dynamic sparse threshold and EMA dynamic adjustment mechanism were used, and the mutual information loss function was combined to reduce the amount of calculation while ensuring the loss of information. In the cross-modal fusion dimension, the gated fusion module of Tacotron[14] and Wav2Vec features[15] is constructed, supplemented by skip connection to optimize the gradient transfer path and enhance the depth correlation between speech and expression. In the aspect of expression generation, the upper and lower half decoupling decoder is designed, and the parameters are adaptively adjusted by the dynamic linear layer, which significantly improves the accuracy of expression detail description and emotion synchronization, and provides a new solution for speech-driven digital human synthesis technology.

Through the four-layer optimization system, the improved model achieves a significant improvement in computational efficiency and generalization ability while maintaining the naturalness of speech synthesis, which provides a new technical path for the lightweight of end-to-end speech synthesis models.

3.1 ynamic threshold sparsification mechanism

When the original dreamtalk model deals with high-dimensional features, there are problems such as large consumption of computing resources and slow inference speed. A large number of redundant parameters not only increase the computational burden, but also may lead to overfitting. In view of this, this study introduces a dynamic threshold sparsification mechanism, which dynamically screens features based on a dynamic sparse mask. By setting a learnable threshold, the feature dimensions that contribute less to the model are automatically identified and eliminated.

The computational efficiency of the improved model is significantly improved, and the number of parameters and reasoning time are reduced compared with the original model, which effectively alleviates the bottleneck of computing resources. At the same time, the generalization ability of the model is enhanced because the redundant information interference is reduced. In addition, the dynamic threshold sparsification mechanism ensures that the model can still maintain a high level of performance while being lightweight by retaining key features, which facilitates the deployment in practical applications.

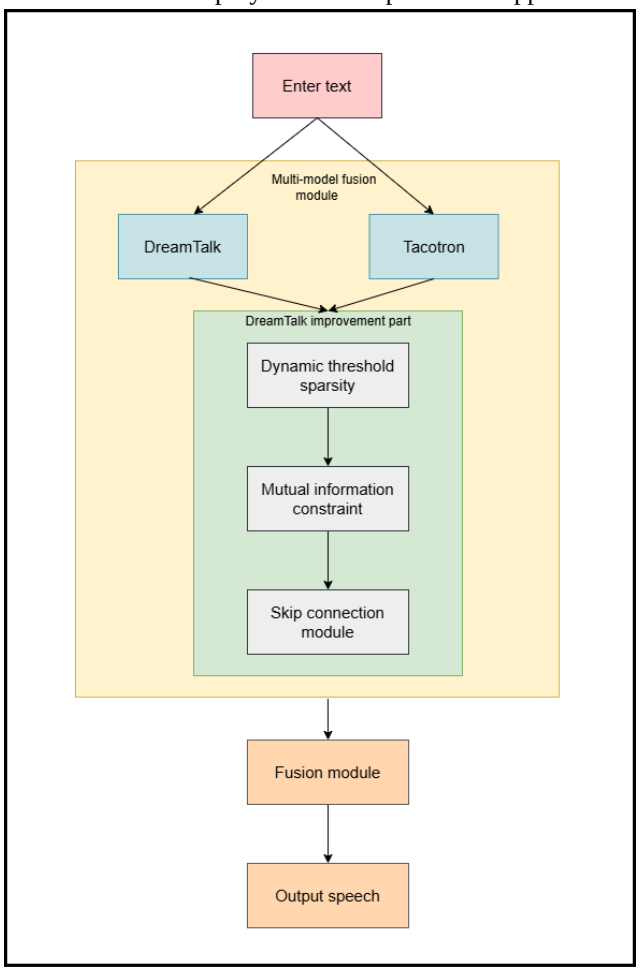

Fig.3 Model framework

Under the key requirements of model computational efficiency optimization, the dynamic threshold sparsification mechanism becomes one of the core innovations of this research. The mechanism aims to solve the problem that the traditional fixed sparsity method cannot adapt to the dynamic changes of features in the process of model training. By introducing a learnable threshold and combining with the Exponential Moving Average (EMA) technology, the dynamic adjustment of the sparsity ratio of model parameters is realized, and the calculation amount is reduced while the key information is retained to the maximum extent, ensuring that the model performance is not significantly affected.

In the training process of the diffusion model, the data characteristics show a complex change trend with the advancement of time steps. To effectively capture these changes and adjust the sparsification strategy accordingly, we design a dynamic threshold calculation method based on learnable threshold and EMA. First, we define a learnable threshold parameter θ, which is optimized through backpropagation during model training. To map

the values of θ to a reasonable range, we use the sigmoid function [16] to convert it to θ', i.e.

$$\theta' = \frac{1}{1+e^{-\theta}} \quad (5)$$

The value range of θ' is limited to the interval of (0,1), which enables the threshold to be adjusted in a reasonable dynamic range.

At the same time, in order to track the dynamic changes of features, we introduce EMA[10] to calculate the mean value μ_t of the absolute values of features. EMA is a commonly used time series smoothing technique, which is able to dynamically update statistics based on historical information and current data. In this study, μ_t is calculated as follows.

$$\mu_t = \alpha\mu_{t-1} + (1-\alpha)\mathbb{E}(|x_t|) \quad (6)$$

α is the smoothing coefficient of EMA, which is usually set to a value close to 1, and α=0.9 was taken in this study. This means that the calculation of μ_t is more dependent on the historical mean μ_{t-1}, but at the same time, it is also adjusted according to the expectation $\mathbb{E}(|x_t|)$ of the absolute value of the feature at the current time. In this way, μ_t can better reflect the overall trend of the absolute value of the feature, and it is somewhat robust to sudden outliers.

Based on the computed θ' and μ_t, we generate the dynamic threshold $\theta' \cdot \mu_t$ and construct the sparse mask M_t accordingly. For each element $x_t[i]$ in the feature vector x_t, the element $M_t[i]$ of the sparse mask M_t is generated according to the following rules:

$$M_t[i] = \begin{cases} 1, & if\ |x_t[i]| > \theta' \cdot \mu_t \\ 0, & otherwise \end{cases} \quad (7)$$

When $|x_t[i]|$ is greater than the dynamic threshold, the value of $M_t[i]$ is 1, and the corresponding element is retained in the sparsification process. Otherwise, $M_t[i]$ is 0, and the corresponding element is set to zero, thus sparsifying the feature vector x_t. This dynamic threshold setting allows the sparsification process to be dynamically adjusted according to the importance and distribution of features. The key features that have larger absolute values and contribute more to the model output are more likely to be retained; However, the relatively unimportant features are sparsified to reduce the amount of calculation.

During backpropagation, to ensure that the sparsified model can still learn effectively, we only perform gradient updates on the corresponding parameters with a value of 1 in the sparse mask M_t. This not only ensures that the model can continue to be optimized in the case of parameter compression, but also avoids the invalid calculation of the sparsified (zeroed) parameters, which further improves the computational efficiency.

Through the above dynamic threshold sparsifying mechanism, the model can dynamically adjust the sparsity ratio of the parameters during the training process, and flexibly balance the computational efficiency and model performance under different training stages and data feature distributions. This mechanism not only effectively reduces the computational burden of the model and improves the inference speed, but also ensures the accuracy and stability of the model in tasks such as expression generation by retaining key information. In practical applications, this mechanism enables the model to maintain good performance under limited computing resources when dealing with large-scale data and complex tasks.

3.2 Mutual information constrained optimization mechanism

In the process of dynamic threshold sparsification, the original dreamtalk model is easy to cause the loss of feature information, which affects the model's ability to capture key semantic and emotional information, and leads to the decline of the accuracy and integrity of the generated results.

In order to solve this problem, based on Mutual Information[17] and Kullback-Leibler Divergence theory[18] in information theory, this study constructs a mutual information constrained optimization mechanism. Mutual information was proposed by Shannon in 1948 to quantify the dependence between two random variables. KL divergence was defined by Kullback and Leibler in 1951 as a measure of how different two probability distributions are.

The basic definition of KL divergence is as follows.

$$D_{KL}(p||q) = \Sigma_x \quad p(x)\log\frac{p(x)}{q(x)} \quad (8)$$

Here, p(x) and q(x) represent two probability distributions, and the formula measures the difference between p(x) and q(x) by calculating the weighted sum of log ratios over all values x.

The basic definition of mutual information is based on joint distribution and marginal distribution, which is expressed as follows.

$$I(X;Y) = D_{KL}(p(X,Y)||p(X)p(Y)) \quad (9)$$

That is, the mutual information is equal to the KL divergence between the joint probability distribution p(X,Y) and the product p(X)p(Y) of the marginal probability distributions, which reflects the amount of information shared between two random variables X and Y.

In this study, the original feature distribution is denoted as $q(x_t)$, and the feature distribution under the action of sparse mask Mt is denoted as $p(x_t|M_t)$. Based on the above

theory, the mutual information loss function is constructed as follows.

$$\mathcal{L}_{\mathrm{MI}} = \mathbb{E}[\mathrm{KL}(p(x_t|M_t) \parallel q(x_t))] = \mathbb{E}[\sum_{i=1}^{D} \quad p(i)\log \frac{p(i)}{q(i)}] \tag{10}$$

This formula quantifies the information loss during dynamic threshold sparsification by calculating the KL divergence of the feature distribution before and after sparsification. In the actual calculation, because it is difficult to estimate the probability distribution directly, the feature mean and variance are used to approximate the distribution. In the training process, $\mathcal{L}_{\mathrm{MI}}$ is incorporated into the total loss function, and the model parameters and sparse threshold are optimized through back propagation, which effectively retains key information while reducing the amount of calculation and maintaining the performance of the model.

After introducing this mechanism, the model performs well in information retention, the retention rate of key features is improved, and the performance degradation caused by information loss is effectively avoided. At the same time, the mutual information constraint optimization mechanism makes the model more accurately balance the computational efficiency and information retention in the sparsification process, which provides a guarantee for the stable training and efficient operation of the model.

3.3 (Multi-model Fusion network) Cross-modal feature fusion module

The original dreamtalk model has the problems of insufficient synchronization and insufficient feature fusion when processing speech and facial expression features, which leads to the inability to accurately match the generated facial expression and speech, and poor expression naturalness and dynamic correlation. The cross-modal feature fusion module constructed in this study strengthens the dynamic association between speech and expression by deeply fusing Tacotron speech features and Wav2Vec acoustic features.

After the introduction of this module, the model achieves a significant improvement in speech-expression synchronization, and the time deviation between lip movements and speech phonemes is reduced, which greatly improves the phenomenon of phonetic and painting synchronization. In addition, the cross-modal feature fusion module effectively enhances the network's ability to express multimodal information through the gate mechanism and skip connection[19], so that the model can better capture the complex mapping relationship between speech and expression.

On the basis of computational efficiency optimization, this study constructs a cross-modal feature fusion module to solve the problem of speech and expression synchronization. The Tacotron model is used to extract the 512-dimensional speech feature f_{taco} containing prosodic and semantic information, while the Wav2Vec model is used to obtain the 1024-dimensional feature f_{w2v} focusing on acoustic details, providing multi-dimensional speech information for fusion.

The module adopts the gating mechanism to realize feature fusion, and learns from the idea that the LSTM gating unit[20] controls the information flow through the Sigmoid function ($\sigma(x) = \frac{1}{1+e^{-x}}$). Firstly, the two features are concatenated and linear transformed, and then the gating signal g is generated by the Sigmoid function: $g = \sigma(\mathrm{Linear}([f_{\mathrm{w2v}}; f_{\mathrm{taco}}]))$. Based on this, the fusion feature $f_{\mathrm{fusion}} = g \cdot f_{\mathrm{w2v}} + (1-g) \cdot f_{\mathrm{taco}}$ is obtained by weighted summation, so that the model can adaptively adjust the feature weight according to the speech characteristics. In addition, the jump connection $f_{\mathrm{final}} = f_{\mathrm{fusion}} + f_{\mathrm{input}}$ of ResNet is introduced to ensure the effective transmission of key information, improve the expression ability of the network, and realize the deep correlation between speech features and expression generation.

3.4 Decouple the decoder

The original dreamtalk model uses a single decoder to process facial expression generation, which is difficult to accurately model the movement of different facial regions. It is easy to interfere with emotional expression and mouth movement, resulting in unnatural local

expressions and loss of details. In this study, based on the decoupled generation network designed by FACS theory[21], the facial expression space is divided into the upper and lower half regions, which are processed independently and modeled by the dual-branch structure respectively.

The introduction of decoupled decoder effectively solves the defects of the original model. In the generation of eye expressions, the movements of eyebrows and eyelids are more consistent with emotional semantics, and the emotional expression is more accurate. In terms of mouth movement generation, the synchronization between mouth shape and speech is further enhanced, and the speech-expression synchronization error is reduced. At the same time, the structure avoids the interference between the actions of different regions, which greatly improves the naturalness and accuracy of local expressions. The generated facial expressions are more vivid and realistic, and have more advantages in detail processing.

Considering that a single decoder is difficult to accurately simulate the movement of different facial regions, this study designs a decoupled generation network based on FACS theory, and divides the facial expression space into the upper and lower half regions for independent processing. The upper half is responsible for emotional expression, while the lower half is closely related to speech articulation.

The decoupled decoder adopts a dual-branch structure, each branch is equipped with a dynamic linear layer, and its design refers to the idea of conditional normalization. The eyebrow decoder uses $W_{eye-brow} = \mathrm{Softmax}(\frac{MLP(s_{emo})}{T}) \cdot \mathbf{W}_{shared-emo}$ to generate a weight matrix based on s_{emo}. According to the acoustic features $f_{acoustic}$, the mouth decoder uses $W_{mouth} = \mathrm{Softmax}(\frac{MLP(f_{acoustic})}{T}) \cdot \mathbf{W}_{shared-mouth}$

Determine the parameters, including $\mathrm{Softmax}(x_i) = \frac{e^{x_i}}{\sum_{j=1}^{n} e^{x_j}}$. Finally, the output of the upper and lower halves is concatenated to avoid the mutual interference between emotional expression and mouth movement, realize the accurate control of eye emotional transmission and mouth speech synchronization, and significantly improve the naturalness and detail accuracy of expression generation.

IV. EXPERIMENTAL ANALYSIS

4.1 Experimental Environment and experimental data set

In this study, an end-to-end training approach is used to jointly optimize modules such as speech feature extraction, cross-modal feature fusion, and expression generation. In the early stage of training, the parameters of pre-trained models such as Tacotron and Wav2Vec are fine-tuned with a small learning rate to adapt them to the speech feature extraction task of this study. Then, the cross-modal feature fusion module was gradually introduced to decouple the decoder, and the alternating training strategy was adopted. The parameters of the expression generation network were fixed, and the feature fusion module was optimized to enhance the correlation between speech and expression features. Then the feature fusion module is fixed, and the decoupled decoder is trained to improve the quality of expression generation. In the training process, the Early Stopping method is used to avoid overfitting, and the training rounds are dynamically adjusted according to the expression naturalness index on the validation set.

The dataset used in this experiment is VoxCeleb. The VoxCeleb dataset is an open source dataset maintained by the Visual Geometry Group at the University of Oxford. The dataset is derived from speech clips in YouTube videos related to celebrities. It is split into VoxCeleb1, which has more than 100,000 voice clips of 1,251 celebrities, and VoxCeleb2, which is much larger, with more than 1 million voice clips of 6,112 celebrities and each clip is at least 3 seconds. It is characterized by a high diversity of speech, including different races, accents, ages, and complex backgrounds, while being of high quality and carefully screened. It has a wide range of applications in speech recognition, speaker verification, speech sentiment analysis, speech synthesis and other fields, which provides rich and high-quality data resources for speech-related research and application.

The experimental platform environment configuration used in this experiment is shown in *Table 1*

Table 1 Experimental environment

Name	version informatio
Operating system	Microsoft Windows11
CPU	12th Gen Intel(R) Core(TM) i7-12700
GPU	NVIDIA GeForce RTX 4060 Ti
Memory capacity	16GB
Deep Learning FrameworkPython	PyTorch 3.10.14
CUDA	11.8
PyTorch	2.1.2
TorchVision	0.16.2

4.2 Comparative analysis of data

We use a variety of evaluation metrics to evaluate the experimental results, and the experimental results are shown in Table 3, which show the experimental results of the four methods SadTalker, Wav2lip, TANGO and Ours, respectively. In this paper, SSIM, SIFT and PSNR are selected as the performance evaluation metrics, which measure the quality of the 2D digital human video generated based on the diffusion model from different perspectives, thus providing a comprehensive evaluation of the performance of the method.

SSIM is a full-reference image quality assessment index, which measures the similarity of images from three aspects: brightness, contrast and structure. SSIM values range from [0,1], with higher values indicating lower image distortion. Therefore, for the similarity curve of video frames, a higher SSIM value is better, and a flatter curve is better, because it means that the similarity

between video frames does not change much and the video quality is stable.

Table 2 Comparison of experimental results of different methods

Methods	SSIM↑	LPIPS↓	PSNR↑
DMT	0.7970	0.1093	28.2298
DreamTalk	0.6973	0.4582	20.3429
SadTalker	0.6693	0.5348	12.8915
Wav2lip	0.8470	0.1277	34.6643
TANGO	0.8758	0.1359	29.0019

LPIPS is a deep learning-based image similarity evaluation metric, which evaluates image similarity by comparing perceptual differences between image patches. The smaller the LPIPS value, the more similar the images. For the similarity curve of video frames, a lower LPIPS value is better, and a flatter curve is better, which indicates that the perceptual difference between video frames is small and the video quality is high.

PSNR is a commonly used metric to evaluate video and image quality, which is calculated by comparing the original signal with the distorted signal. A higher PSNR value indicates less distortion of the video frame. For the similarity curve of video frames, the higher the PSNR value, the better, the upward of the curve indicates that the video quality is improving, and the downward of the curve indicates that the video quality is decreasing.

The experimental results show that the model proposed in this study outperforms the previous methods in many aspects. The cross-modal feature fusion module realized the deep fusion of speech features through the gate mechanism and skip connection, which significantly improved the synchronization. The decoupled decoder separated the upper and lower half of the facial motion based on FACS theory, and combined with the dynamic linear layer to enhance the expression detail generation ability. The dynamic threshold sparsification and mutual information constrained optimization mechanism greatly reduce the computational complexity under the premise of controllable information loss. When mutual information constrained optimization is disabled, the inference time of the model decreases but the performance index deteriorates significantly. These results prove that the collaborative design of model components is the key to achieve efficient and natural expression generation.

V. CONCLUSION

In this study, the DreamTalk speech synthesis model is optimized, and the performance of the model is significantly improved by introducing techniques such as adaptive threshold sparsification method, mutual information constraint, multi-model fusion and skip connection. In terms of speech synthesis quality, computational efficiency and generalization ability, the improved model is significantly better than the traditional DreamTalk model and other comparison models.

However, there are still some shortcomings in this study. In the process of multi-model fusion, the current simple average fusion method essentially treats the output of each model with equal weight, which fails to fully consider the differences in the advantages of different models in processing specific speech features or scenes, and it is difficult to maximize the effectiveness of each model in complex speech synthesis tasks. In the field of cross-modal applications, although the speech-image matching has been improved, there is still a large room for improvement in the quality and diversity of image generation. There is a gap between the generated image and the real image and user expectation in detail texture, color richness and creative expression. When the adaptive sparsization method faces extreme data distribution, such as a small number of abnormal speech samples or a serious imbalance of data feature distribution, the stability of the model will be affected, and problems such as fluctuations in the quality of synthesized speech and abnormal parameter update may occur.

To address these shortcomings, future research will be carried out in several directions. In the aspect of multi-model fusion, the fusion strategy based on attention mechanism and dynamic weight allocation will be deeply explored. By constructing an intelligent evaluation system, the model can automatically allocate the weight of each sub-model according to the characteristics of the input speech, and give full play to the advantages of different models. In the field of cross-modal research, we plan to combine generative adversarial networks and self-supervised learning technology to further explore the potential correlation between speech and image, build a more powerful cross-modal mapping model, improve the quality and diversity of image generation, and realize more creative and realistic image generation driven by speech. For the adaptive sparsification method, a dynamic adjustment threshold strategy and an abnormal data detection mechanism are introduced. By real-time monitoring of data distribution characteristics, the sparsification process is dynamically optimized, and the stability of the model in extreme data environments is enhanced, so as to further improve the overall performance

and application range of the model, which provides more powerful support for the development of speech synthesis technology and cross-modal research.

ACKNOWLEDGEMENTS

This paper received funding from "Guangdong University of Petrochemical Technology College Student Innovation and Entrepreneurship Project No. 24A014".

REFERENCES

[1] Priyadharshini, A. R., & Annamalai, R. (2024). Identification and Reconstruction of Human Faces into 3D Models Using SSD-Based and Attention Mesh Models in Real-Time. *SN Computer Science*, *5*(8), 1-9.

[2] Buhari, A. M., Ooi, C. P., Baskaran, V. M., Phan, R. C., Wong, K., & Tan, W. H. (2020). FACS-based graph features for real-time micro-expression recognition. *Journal of Imaging*, *6*(12), 130.

[3] Chauhan, A., & Jain, S. (2024). FMeAR: FACS Driven Ensemble Model for Micro-Expression Action Unit Recognition. *SN Computer Science*, *5*(5), 598.

[4] Kaneko, T., Kameoka, H., Tanaka, K., & Hojo, N. (2019). Stargan-vc2: Rethinking conditional methods for stargan-based voice conversion. *arXiv preprint arXiv:1907.12279*.

[5] Zhang, C., Wang, C., Zhang, J., Xu, H., Song, G., Xie, Y., ... & Feng, J. (2023). Dream-talk: Diffusion-based realistic emotional audio-driven method for single image talking face generation. *arXiv preprint arXiv:2312.13578*.

[6] Xu, S., Chen, G., Guo, Y. X., Yang, J., Li, C., Zang, Z., ... & Guo, B. (2024). Vasa-1: Lifelike audio-driven talking faces generated in real time. *Advances in Neural Information Processing Systems*, *37*, 660-684.

[7] Ma, Z., Zhu, X., Qi, G. J., Lei, Z., & Zhang, L. (2023). Otavatar: One-shot talking face avatar with controllable tri-plane rendering. In *Proceedings of the IEEE/CVF Conference on Computer Vision and Pattern Recognition* (pp. 16901-16910).

[8] Singer, U., Polyak, A., Hayes, T., Yin, X., An, J., Zhang, S., ... & Taigman, Y. (2022). Make-a-video: Text-to-video generation without text-video data. *arXiv preprint arXiv:2209.14792*.

[9] Ma, Y., Zhang, S., Wang, J., Wang, X., Zhang, Y., & Deng, Z. (2023). DreamTalk: When Emotional Talking Head Generation Meets Diffusion Probabilistic Models. *arXiv preprint arXiv:2312.09767*.

[10] Chen, R., Pang, K., Wang, Z., Liu, Q., Tang, C., Chang, Y., & Huang, M. (2025). A self-supervised graph convolutional model for recommendation with exponential moving average. *Neural Computing and Applications*, 1-17.

[11] Zhao, S., Wang, Y., Yang, Z., & Cai, D. (2019). Region mutual information loss for semantic segmentation. *Advances in Neural Information Processing Systems*, *32*.

[12] Nair, N. G., Mei, K., & Patel, V. M. (2023). At-ddpm: Restoring faces degraded by atmospheric turbulence using denoising diffusion probabilistic models. In *Proceedings of the IEEE/CVF winter conference on applications of computer vision* (pp. 3434-3443).

[13] Hou, J., Lu, Y., Wang, M., Ouyang, W., Yang, Y., Zou, F., ... & Liu, Z. (2024). A Markov Chain approach for video-based virtual try-on with denoising diffusion generative adversarial network. *Knowledge-Based Systems*, *300*, 112233.

[14] Wang, Y., Skerry-Ryan, R. J., Stanton, D., Wu, Y., Weiss, R. J., Jaitly, N., ... & Saurous, R. A. (2017). Tacotron: Towards end-to-end speech synthesis. *arXiv preprint arXiv:1703.10135*.

[15] Schneider, S., Baevski, A., Collobert, R., & Auli, M. (2019). wav2vec: Unsupervised pre-training for speech recognition. *arXiv preprint arXiv:1904.05862*.

[16] Zhao, Y., & Li, X. (2024, September). Better approximation of sigmoid function for privacy-preserving neural networks. In *Journal of Physics: Conference Series* (Vol. 2852, No. 1, p. 012007). IOP Publishing.

[17] A Mutual Information Based Approach for Feature Subset Selection and Image ClassificationA Mutual Information Based Approach for Feature Subset Selection and Image Classification.

[18] Xu, H., Li, Y., Zhang, M., & Tong, P. (2024). Sonar image segmentation using a multi-spatial information constraint fuzzy C-means clustering algorithm based on KL divergence. *International Journal of Machine Learning and Cybernetics*, 1-18.

[19] Chen, H., Lu, X., Li, S., & He, L. (2025). Improving aluminum surface defect super-resolution with diffusion models and skip connections. *Materials Today Communications*, *42*, 111297.

[20] Wang, W., Han, D., Duan, X., Yong, Y., Wu, Z., Ma, X., ... & Dai, K. (2024). Fast-Activated Minimal Gated Unit: Lightweight Processing and Feature Recognition for Multiple Mechanical Impact Signals. *Sensors*, *24*(16), 5245.

[21] Gilbert, M., Demarchi, S., & Urdapilleta, I. (2021). FACSHuman, a software program for creating experimental material by modeling 3D facial expressions. *Behavior Research Methods*, *53*(5), 2252-2272.

International Journal of Advanced Engineering Research and Science (IJAERS)
Peer-Reviewed Journal
ISSN: 2349-6495(P) | 2456-1908(O)
Vol-12, Issue-5; May, 2025
Journal Home Page Available: https://ijaers.com/
Article DOI: *https://dx.doi.org/10.22161/ijaers.125.4*

Mathematical Modeling and Simulation of an Alkaline Electrolyzer for Hydrogen Production

Andrianaivoarivelo Jaolalaina Arisoa[1], Andrianjatovo Falinirina[2], Rafanjanirina Eulalie Odilette[3], Randriamanantany Zely Arivelo[4]

[1]Department of Physics, Faculty of Sciences, University of Antananarivo
jaolalaina@gmail.com, https://orcid.org/0009-0005-2323-2933
[2]Department of Physics, Faculty of Sciences, University of Antananarivo
afalinirina@gmail.com , https://orcid.org/0009-0009-0523-6788
[3]Department of Physics, Faculty of Sciences, University of Antananarivo
rafanjanirina@yahoo.fr
[4]Department of Physics, Faculty of Sciences, University of Antananarivo
zelyran@yahoo.fr

Received: 09 Apr 2025,

Receive in revised form: 07 May 2025,

Accepted: 13 May 2025,

Available online: 20 May 2025

***Keywords*— Green hydrogen, Alkaline electrolysis, Water electrolysis, Mathematical modeling, MATLAB/Simulink simulation, Electrolyzer performance, Ohmic loss and activation overpotential, Hydrogen production.**

***Abstract*—** *In the context of energy transition and the growing interest in green hydrogen as a sustainable fuel, this study presents a comprehensive mathematical modeling of an alkaline water electrolyzer. The paper investigates the fundamental physical and electrochemical processes involved in hydrogen generation, covering electric, thermodynamic, and electrochemical models. Key parameters such as electrolyte concentration, conductivity, membrane resistance, and gas bubble effects are incorporated. Simulation results using MATLAB/Simulink are provided to illustrate the behavior of the system under varying operational conditions. The findings contribute to the optimization of hydrogen production systems through accurate model-based design.*

I. INTRODUCTION

Hydrogen is increasingly recognized as a crucial pillar in the global transition toward a low-carbon energy future [1]. As countries and industries seek sustainable alternatives to fossil fuels, hydrogen stands out for its versatility, abundance, and clean combustion properties—producing only water vapor when used in fuel cells or combustion engines. Its application spans various sectors, including transportation, power generation, chemical manufacturing, and energy storage, making it a keystone for decarbonizing hard-to-abate industries and stabilizing renewable-dominated power grids [2].

A key determinant of hydrogen's environmental impact lies in the method of its production. Today, a significant portion of global hydrogen is still derived from fossil fuels, particularly through steam methane reforming (SMR), which results in substantial CO_2 emissions [3]. To achieve climate targets outlined in international agreements such as the Paris Accord, a paradigm shift toward low-emission or zero-emission hydrogen production is imperative. Among the various technologies available, water electrolysis emerges as a particularly promising solution, especially when powered by renewable electricity from solar, wind, hydro, or other sustainable sources. This method, often referred to as "green hydrogen" production, offers the potential for a

closed-loop energy cycle with minimal environmental footprint[4].

Water electrolysis involves the decomposition of water molecules (H_2O) into hydrogen (H_2) and oxygen (O_2) gases through the application of an electric current. Several electrolysis technologies have been developed over the years, including Proton Exchange Membrane (PEM) electrolysis, Solid Oxide Electrolysis (SOE), and Alkaline Water Electrolysis (AWE)[5] Among these, alkaline electrolysis remains one of the most mature and commercially viable options. It benefits from a long operational history, relatively simple system design, and the use of non-noble, low-cost catalysts such as nickel and iron-based materials. Furthermore, the scalability and reliability of AWE systems make them attractive for both centralized and decentralized hydrogen production facilities.

Despite its maturity, the alkaline electrolysis process presents several technical and scientific challenges that must be addressed to enhance efficiency, reduce capital and operational costs, and enable seamless integration into renewable energy systems [6]. Key areas of improvement include minimizing energy losses due to overpotentials, managing heat and mass transfer within the electrolyzer cell, and ensuring long-term stability under dynamic operating conditions. Achieving these objectives requires not only experimental advancements but also the development of accurate and comprehensive mathematical models capable of capturing the complex physical, chemical, and electrical behaviors of the system.

Modeling and simulation play a pivotal role in understanding and optimizing electrolyzer performance. By translating the underlying physical phenomena into mathematical expressions, models allow for predictive analysis, system design, sensitivity studies, and control strategy development. In the context of alkaline electrolysis, an effective model must integrate various interdependent domains: electrochemical kinetics governing the anode and cathode reactions, thermal dynamics affecting reaction rates and efficiency, and electrical parameters that determine cell voltage, current density distribution, and overall energy consumption [7].

This article presents a detailed and integrated mathematical model of an alkaline water electrolyzer. The model encompasses three key dimensions: electrical modeling, which establishes the relationship between applied voltage and current density while accounting for activation, ohmic, and concentration overpotentials; thermal modeling, which considers heat generation from internal resistances and electrochemical inefficiencies, along with heat dissipation via conduction, convection, and radiation; and electrochemical modeling, which describes the fundamental electrode reactions influenced by operating parameters such as electrolyte concentration, temperature, and pressure.

By simulating the behavior of the electrolyzer under various conditions—including different operating temperatures, current densities, and load profiles—the model provides critical insights into performance optimization. These simulations not only reveal the interplay between thermal and electrochemical dynamics but also highlight the impact of design choices on efficiency, hydrogen production rate, and operational stability.

Furthermore, the model has been implemented and validated using MATLAB/Simulink, offering a flexible framework for future expansion and integration into larger energy systems, such as hybrid renewable-hydrogen grids or sector-coupled infrastructures. Through parametric studies and sensitivity analyses, the model also facilitates informed decision-making for system design, control, and scaling.

II. ALKALINE ELECTROLYZER MODELING

2.1. Electrolyte Properties

In alkaline water electrolysis systems, the electrolyte serves as the primary medium for ionic conduction, bridging the electrochemical gap between the anode and cathode. Among various candidate electrolytes, potassium hydroxide (KOH) is most widely used due to its favorable properties, including high ionic conductivity, chemical stability, and compatibility with commonly used electrode materials. The hydroxide ions (OH^-) in the KOH solution are the primary charge carriers, moving from the cathode to the anode under the influence of an electric field. Their transport is essential for sustaining the redox reactions that occur at the electrodes: water is oxidized to oxygen at the anode, and reduced to hydrogen at the cathode. The ability of the electrolyte to facilitate efficient ion movement, while minimizing resistive losses, is central to the performance and energy efficiency of the electrolysis cell.

The physical properties of the KOH solution its concentration, density, ionic conductivity, and electrical resistance play critical roles in determining system behavior. These properties are not static; they evolve dynamically with changes in operating conditions, particularly temperature, electrolyte composition, and the presence of gas bubbles generated during electrolysis. To accurately simulate and predict the behavior of alkaline electrolyzers under real-world conditions, it is necessary to develop robust mathematical models that capture these

interdependencies with precision. Such models enable researchers and engineers to perform parametric studies, design optimization, and control strategy development for large-scale hydrogen production systems.

A fundamental quantity in electrolyte modeling is the molar concentration of KOH in the aqueous solution, which defines the number of moles of solute per liter of solution. In practice, commercial KOH solutions are typically described in terms of weight percentage (% w/w), which is more convenient for manufacturing and handling. However, physical and electrochemical models require molar concentration as input. Therefore, the first step in electrolyte characterization involves converting between weight percentage and molarity. This conversion depends on the density of the solution, which varies with both temperature and KOH concentration. The conversion is mathematically expressed as the equation (1):

$$C = \frac{10.\rho.\omega}{M} \quad (1)$$

where C is the molar concentration (mol/L), ω is the weight fraction (unitless), ρ is the density of the solution in g/cm³, and M is the molar mass of KOH (56.11 g/mol). Accurate calculation of C from www requires empirical correlations or tabulated data that provide solution density for various temperatures and concentrations. These correlations are typically derived from experimental measurements and interpolated to cover the desired operating range.

The density of the KOH solution itself is another crucial parameter, influencing not only the concentration conversion but also mass transport, buoyancy-driven convection, and hydrodynamic behavior within the cell. Density increases nonlinearly with concentration due to the progressive dissociation of KOH into K^+ and OH^- ions and their hydration by water molecules. However, the effect of temperature is inverse: as temperature increases, the kinetic energy of molecules disrupts hydrogen bonding and ionic hydration shells, leading to thermal expansion and reduced solution density. Empirical models typically represent density as a quadratic function of temperature at fixed concentrations, or as a surface fit over both variables equation (2).

$$\rho(T, C) = a + bT + cT^2 \quad (2)$$

where T is the temperature in °C, C is the molarity, and a, b, and c are empirically determined coefficients. Accurately modeling density is essential not only for thermodynamic calculations but also for determining natural convection currents and bubble rise velocities, which affect gas-liquid separation and mass transport within the cell.

Closely related to the density is the ionic conductivity of the KOH solution. This property defines the electrolyte's ability to transport charged species specifically, the hydroxide ions under an applied electric field. Conductivity depends strongly on both temperature and KOH concentration, and exhibits a non-linear behavior with respect to both. At low concentrations, increasing the KOH content leads to an increase in ion concentration and therefore higher conductivity. However, beyond a certain concentration (typically around 6 to 8 mol/L), conductivity reaches a peak and begins to decline. This is because the increased viscosity and interionic interactions at high concentrations impede ion mobility. Similarly, conductivity increases with temperature, as the thermal agitation enhances the diffusion coefficients of ions and reduces the solution's viscosity. This temperature effect can be modeled using Arrhenius-type equations or empirically fitted polynomial expressions. For instance, one widely used correlation is:

$$\kappa(T, C) = \kappa_0(C).[1 + \alpha(C)(T - T_0)] \quad (3)$$

where $\kappa(T, C)$ is the conductivity in S/m, κ_0 is the reference conductivity at a baseline temperature T_0, and is the temperature coefficient of conductivity, which varies with concentration. Accurate modeling of κ is essential for calculating ohmic losses in the cell and optimizing cell voltage for minimal energy consumption.

The electrical resistance of the electrolyte is inversely related to its conductivity and is governed by the classical formula (4):

$$R_{el} = \frac{d}{\kappa.A} \quad (5)$$

where R_{el} is the electrolyte resistance in ohms, d is the distance between electrodes, A is the cross-sectional area of conduction, and κ is the ionic conductivity. However, this expression assumes a homogenous medium, which is not the case during actual electrolysis, where gas bubbles of hydrogen and oxygen are continuously generated at the cathode and anode, respectively. These bubbles are non-conductive and occupy a fraction of the electrolyte's volume, thereby reducing the effective area available for ionic conduction. The presence of gas voids leads to increased local resistance and non-uniform current density distribution across the electrode surfaces. To account for this, the effective conductivity κ_{eff} is often modeled using Bruggeman's correction at the equation (6):

$$\kappa_{eff} = \kappa.(1 - \varepsilon)^n \quad (6)$$

where ε is the gas void fraction (volume of bubbles/total volume), and n is an empirical exponent typically ranging from 1.5 to 2.5 depending on the morphology of the bubbles. The void fraction itself depends on several factors including current density, surface roughness, electrode orientation, temperature, and pressure. High current densities generate more gas and lead to larger bubble formation rates, exacerbating the increase in resistance. Therefore, a comprehensive electrolyte model must dynamically update ε based on operating conditions to yield realistic resistance estimates.

In parallel to the electrolyte, the membrane in alkaline water electrolysis systems plays an equally pivotal role in determining the cell's performance, energy efficiency, and operational safety. While the electrolyte facilitates ionic conduction between the electrodes, the membrane physically separates the anode and cathode compartments, preventing the intermixing of hydrogen and oxygen gases while still permitting the transport of hydroxide ions (OH^-). This selective permeability is critical not only for product purity but also to avoid the formation of explosive gas mixtures. Moreover, the membrane contributes substantially to the overall cell resistance, as its microstructure and material composition directly influence the internal ohmic losses. Consequently, a detailed understanding of the membrane's physical characteristics and their influence on ionic conduction is essential for accurate electrochemical modeling and system design.

The effective performance of the membrane is governed by a combination of its chemical stability in caustic environments and its microstructural properties, including porosity, tortuosity, thickness, and surface area. Among these, porosity and tortuosity are particularly significant because they define the efficiency of ion transport through the membrane matrix. Porosity, typically expressed as a dimensionless volume fraction, represents the portion of the membrane that consists of interconnected voids or channels through which the electrolyte can diffuse. A higher porosity generally promotes greater ionic mobility by providing more conductive pathways, thereby decreasing internal resistance. However, excessive porosity can weaken the membrane mechanically or increase gas crossover, thereby compromising system reliability. Tortuosity, on the other hand, quantifies the geometric complexity of the ion transport paths. Even with high porosity, a highly tortuous structure can hinder effective ion conduction by increasing the actual distance that ions must travel, thus reducing the membrane's effective conductivity.

To model the impact of membrane structure on ionic transport, the effective conductivity σ_{eff} is commonly estimated using empirical or semi-empirical formulations that incorporate porosity **ε** and tortuosity **τ**. One of the most widely applied models is the Bruggeman correlation, which approximates effective conductivity as the equation (7):

$$\sigma_{eff} = \sigma_0 . \frac{\varepsilon}{\tau} \quad (7)$$

where σ_0 is the intrinsic conductivity of the bulk electrolyte (typically concentrated KOH), **ε** is the porosity, and **τ** is the tortuosity. This relationship reveals that even if the electrolyte is highly conductive, the microstructure of the membrane can significantly impede ion flow, thereby increasing the resistive losses within the cell. Both porosity and tortuosity are influenced by the membrane's fabrication method, aging, and the presence of fouling or gas bubble accumulation, all of which need to be considered in dynamic electrochemical models.

Temperature and electrolyte concentration further influence ionic conductivity, not just at the bulk electrolyte level but also within the membrane. As temperature increases, the viscosity of the KOH solution decreases and the mobility of hydroxide ions increases, which in turn enhances conductivity. However, the same temperature rise may also accelerate membrane degradation or increase gas permeability, which introduces trade-offs in design. Furthermore, the concentration of KOH impacts the number of available charge carriers, but only up to an optimal point beyond which ion pairing and viscosity effects begin to hinder transport. The conductivity behavior as a function of temperature and concentration within porous media follows similar nonlinear trends as observed in bulk solution but must be adjusted to reflect the microenvironment within the membrane.

From a structural perspective, the electrical resistance of the membrane is also a function of its thickness L and its effective surface area A. This relationship is captured by Ohm's law, equation (8), for a resistive medium:

$$R = \frac{L}{\sigma_{eff} \cdot A} \quad (8)$$

Here, increasing membrane thickness linearly increases resistance, while a larger active surface area contributes to lower resistance by distributing current over a broader region. In practical design, membrane thickness must be optimized to balance electrical performance with mechanical robustness. Thinner membranes typically offer lower resistance and thus lower voltage losses, but may be prone to rupture, delamination, or increased gas crossover under high-pressure operation. Surface area, in contrast, can be enhanced through the use of structured supports or flow field designs that increase membrane exposure without compromising integrity.

Over time, electrochemical operation can degrade membrane performance through physical wear, chemical attack, or deposition of impurities. These aging effects alter porosity, tortuosity, and mechanical strength, often resulting in increased resistance and reduced ionic selectivity. Models that predict long-term membrane behavior must therefore incorporate degradation kinetics and material fatigue, in addition to real-time operating parameters like current density, pressure, and electrolyte renewal rate. Moreover, the interaction of evolving gas bubbles with the membrane surface particularly under high current density can introduce non-uniformities in ion transport and localized resistance spikes.

To address the trade-offs inherent in membrane design, modern research is increasingly focused on composite and nanostructured membranes that combine desirable properties such as high ionic conductivity, mechanical strength, and chemical resistance. These include hybrid membranes incorporating inorganic fillers like zirconia or titania nanoparticles, which reduce tortuosity and enhance hydroxide ion pathways, as well as multilayer membranes that separate structural and transport functions. Such innovations aim to decouple conductivity from permeability and durability, pushing the boundaries of electrolysis efficiency.

Electrodes constitute the reactive interfaces where the core electrochemical transformations of water splitting occur—namely, the oxygen evolution reaction (OER) at the anode and the hydrogen evolution reaction (HER) at the cathode. In alkaline water electrolysis, the most commonly used electrode materials are based on nickel or nickel alloys due to their excellent catalytic activity in alkaline environments, mechanical robustness, relatively low cost, and compatibility with concentrated potassium hydroxide (KOH) electrolytes. The accurate modeling of electrode behavior is critical for predicting system efficiency, voltage requirements, and dynamic response to load variations. Electrode parameters influence not only the kinetics of charge transfer reactions but also the distribution of electric fields, current densities, and temperature gradients within the electrolyzer.

From an electrical standpoint, the electrodes must exhibit high intrinsic conductivity to minimize ohmic losses associated with in-plane and through-plane electron transport. The electrical conductivity (σ-e) of nickel-based materials typically ranges between 1×10^7 to 1.5×10^7 S/m at room temperature, depending on alloy composition and microstructure. Conversely, the resistivity (ρ_e), which is the reciprocal of conductivity, must be sufficiently low to ensure that current can be supplied to the electrochemical interface without significant voltage drop. The total resistive loss across an electrode, therefore, depends not only on the material's bulk resistivity but also on its geometric configuration (thickness and surface area), and its contact resistance with adjacent components such as the current collectors, porous transport layers, and the membrane.

Beyond their role as conductors, electrodes are sites of charge transfer where electrons from the external circuit interact with hydroxide ions and water molecules to drive the HER and OER. These interfacial processes are not instantaneous and involve overcoming energy barriers commonly referred to as activation overpotentials (η_{act}). Activation overpotentials represent the additional voltage required to surmount the kinetic limitations of the electrode reactions and initiate electron transfer. In electrochemical modeling, the Tafel approximation is often used to describe the nonlinear relationship between the overpotential and the resulting current density. For a single-step, rate-determining electrochemical reaction, the Tafel equation is given as the equation (9):

$$\eta_{act} = a + b.log_{10}(j) \quad (9)$$

where η_{act} is the activation overpotential (V), j is the current density (A/m²), a is the Tafel intercept (related to exchange current density), and b is the Tafel slope, which depends on temperature, number of electrons involved, and transfer coefficient. The slope b typically ranges between 30–120 $mV/decade$ for common alkaline reactions, and reflects the sensitivity of the reaction rate to applied overpotential.

The exchange current density j_0, embedded in the Tafel intercept, is a critical kinetic parameter that quantifies the intrinsic catalytic activity of the electrode material. It corresponds to the rate of the forward and reverse reactions at equilibrium (zero net current) and is strongly dependent on electrode surface area, morphology, electrolyte concentration, and temperature. For HER on nickel in alkaline media, j_0 values typically lie between 10^{-3} and 10^{-1} A/m², while for the more sluggish OER, values are generally lower, necessitating the use of dopants or composite materials like Ni-Fe or Ni-Co alloys to improve catalytic activity.

To improve overall performance, electrode surfaces are often engineered to increase the electrochemically active surface area (ECSA), which enhances the number of reactive sites and reduces the effective current density per unit area. This is achieved through techniques such as roughening, nanostructuring, or the use of porous and

foam-based substrates. The true current density, which affects reaction kinetics, must therefore be corrected for the real surface area rather than the geometric one, equation (10):

$$j_{real} = \frac{j_{geo}}{Ecsa/A_{geo}} \quad (10)$$

where j_{geo} is the measured current density based on geometric area A_{geo}, and $Ecsa$ is the electrochemically active surface area. Accurate modeling of activation losses requires realistic estimations of ECSA, which can be experimentally determined via cyclic voltammetry or impedance spectroscopy.

In addition to activation overpotentials, concentration overpotentials may arise due to mass transport limitations near the electrode surface, particularly at high current densities. Although these are typically less pronounced in well-mixed alkaline systems, their inclusion is essential for high-fidelity simulations. For porous electrodes, diffusion within the electrode matrix must also be considered, often modeled using the Nernst-Planck equation coupled with Darcy's law to capture electrochemical and fluid dynamic interactions.

Furthermore, the thermal and chemical stability of electrode materials under sustained operation is critical for long-term durability. High operating temperatures, aggressive chemical environments, and fluctuating loads can lead to corrosion, catalyst leaching, or changes in surface morphology, all of which degrade electrode performance over time. These degradation mechanisms can be incorporated into dynamic aging models, where parameters such as exchange current density and surface roughness evolve as functions of time, temperature, and electrochemical cycling.

In advanced models, the interfacial behavior of electrodes can also include double-layer capacitance and charge transfer resistance, which are particularly relevant for transient and impedance-based analyses. These components are typically represented in equivalent circuit models using resistor-capacitor (RC) networks and fitted to experimental electrochemical impedance spectroscopy (EIS) data.

2.2. Electrical and Electrochemical Model

Building upon the electrode-level phenomena described previously, the total cell voltage in an alkaline electrolyzer can be decomposed into a series of fundamental contributions that reflect the physical and electrochemical realities of water splitting. These include the reversible thermodynamic voltage, kinetic losses at the electrode interfaces, resistive losses across ionic and electronic conductors, and corrections for non-standard operating conditions. A comprehensive electrochemical model must capture these contributions to reliably simulate electrolyzer behavior under various load and environmental conditions.

At the core of this model lies the reversible cell voltage E_{rev} in equation 11, which represents the minimum theoretical voltage required to split water molecules under standard conditions (25°C, 1 atm, unit activity). It is determined from the Gibbs free energy change ΔG° of the overall electrochemical reaction. The reversible voltage serves as the thermodynamic lower limit for water electrolysis and is given by:

$$E_{rev} = \frac{\Delta G^{\circ}}{nF} \quad (11)$$

where n is the number of electrons transferred per molecule of H_2 (typically 2), and F is Faraday's constant. This value typically ranges around 1.23 V under standard conditions, but does not account for losses arising from electrode kinetics, transport resistances, or system configuration.

Superimposed on this ideal voltage are the ohmic losses V_{ohmic}, at the *equation 12*, which result from resistances encountered by both ionic and electronic charge carriers. These include the bulk electrolyte resistance (governed by KOH or NAOH concentration and temperature), the ionic resistance of the membrane, and resistive contributions from electrode contacts and gas bubbles formed at high current densities. The effective ohmic drop is calculated via:

$$V_{ohmic} = I.R_{total} = I.(R_e + R_m + R_b) \quad (12)$$

where R_e, R_m, and R_b are the resistances of the electrolyte, membrane, and gas bubble-induced blockage, respectively. These losses scale linearly with current and represent a significant portion of total voltage consumption, especially in high-efficiency systems operating at elevated currents.

Another major contributor to the cell voltage is the activation overpotential η_{act} (equation 13) at both the anode and cathode, arising from the finite rate of electrochemical reactions at the electrode-electrolyte interface. As outlined in *Section 2.3*, this kinetic barrier is typically modeled using the Tafel approximation, which links the overpotential to the logarithm of the current density:

$$\eta_{act} = a + b.\log(j) \quad (13)$$

These overpotentials differ significantly between the oxygen evolution reaction and hydrogen evolution

reaction, with oxygen evolution reaction typically being more sluggish and requiring higher overpotentials due to its complex, multi-electron transfer mechanism. The accurate estimation of these losses requires careful consideration of material-specific kinetic parameters such as the exchange current density and Tafel slope, both of which are sensitive to surface structure, temperature, and electrolyte composition.

To account for non-standard operating conditions, the cell voltage must also incorporate a Nernstian correction that adjusts the theoretical voltage to reflect actual partial pressures of hydrogen and oxygen, as well as hydroxide ion concentration. The Nernst *equation 14* provides this adjustment:

$$R_{Nerst} = E^o + \frac{RT}{nF}\ln\left(\frac{a_{product}}{a_{reactants}}\right) \quad (14)$$

Here, *R* is the universal gas constant, *T* is the absolute temperature, and *a* represents the activity (partial pressure) of the species involved. This correction is critical when simulating industrial conditions where pressures and concentrations differ significantly from standard-state assumptions.

Combining these contributions, the total operating cell voltage is expressed as the equation 15:

$$V_{cell} = E_{rev} + \eta_{anode} + \eta_{cathode} + V_{ohmic} + \Delta_{Nernst} \quad (15)$$

This expression forms the backbone of any predictive electrochemical model and allows for parametric studies on system performance as a function of material properties, current density, temperature, and electrolyte composition. The model can be further refined by incorporating temperature dependence of each term, dynamic behavior under load cycling, and degradation factors for long-term operation.

In conclusion, the electrical and electrochemical model serves as a critical extension of electrode-level analysis, integrating thermodynamic, kinetic, and transport phenomena to provide a full picture of voltage requirements and energy efficiency in alkaline electrolysis. Accurate representation of each component is essential for guiding the design of high-performance electrolyzers and enabling reliable techno-economic assessments.

2.3. Thermodynamic Model

The thermodynamic model underpins the fundamental energy requirements of water electrolysis by focusing on the intrinsic energetics of the water splitting reaction. Unlike the electrochemical model, which addresses the voltage losses associated with practical system components, the thermodynamic model isolates the ideal energy input based on changes in enthalpy (ΔH) and entropy (ΔS) associated with the reaction. These thermodynamic quantities define the energy content and disorder change as water molecules are dissociated into hydrogen and oxygen gases, and are crucial for understanding the theoretical efficiency limits of the electrolytic process.

At the heart of the thermodynamic model lies the distinction between the Gibbs free energy change (ΔG) and the enthalpy change (ΔH) of the reaction. The Gibbs free energy represents the minimum electrical work needed to split water under reversible, isothermal, and isobaric conditions, while the enthalpy encompasses the total energy, both electrical and thermal required to drive the reaction. The standard enthalpy change for the overall reaction (equation 16) at 25°C is approximately +285.8 kJ/mol, and the corresponding Gibbs free energy change is +237.2 kJ/mol[8]. These values demonstrate that a portion of the energy required for water electrolysis can be supplied as heat, especially under elevated temperature operations.

$$H_2O \rightarrow H_2 + \tfrac{1}{2}O_2 \quad (16)$$

This thermodynamic analysis leads to the concept of the thermoneutral voltage E_{th} in the equation 17, which represents the voltage at which the supplied electrical energy is exactly balanced by the total enthalpic demand of the reaction, without any net heat generation or absorption. The thermoneutral voltage is defined by:

$$E_{th} = \frac{\Delta H}{nF} \quad (17)$$

where ΔH is the enthalpy change per mole of reaction, n is the number of electrons transferred ($n = 2$ for hydrogen generation), and F is Faraday's constant. At standard conditions, E_{th} is approximately 1.48 V. This value is higher than the reversible voltage (typically $\approx 1.23\ V$), highlighting the gap between the minimum electrical input (from ΔG) and the total energy requirement (from ΔH), which can be partially compensated by thermal energy input in high-temperature systems.

The difference between the thermoneutral voltage and the reversible voltage provides a framework for evaluating the efficiency and energy integration potential of electrolyzer systems. Operating at voltages close to the thermoneutral value enables thermally balanced operation, where no excess heat is required or released, while operation below this value necessitates external heat input to sustain the reaction. Conversely, if the cell is operated above the thermoneutral voltage, excess heat is generated, which may require active cooling and presents opportunities for cogeneration or heat recovery.

Furthermore, temperature-dependent variations in ΔG and ΔH must be taken into account when modeling thermodynamic behavior across a range of operating temperatures. These dependencies influence both the thermodynamic efficiency and the practical feasibility of operating the system under non-standard conditions, such as in high-temperature electrolysis. The integration of these parameters into a comprehensive thermodynamic framework allows for accurate prediction of the energy flows in the system and supports the optimization of thermal and electrical input in hybrid energy scenarios.

The thermodynamic model provides essential insight into the fundamental energy landscape of water electrolysis by establishing the theoretical bounds of energy input based on enthalpy and entropy changes. The concept of the thermoneutral voltage bridges the gap between ideal reversible operation and real energy demands, forming a foundational element for the design, optimization, and thermal integration of advanced alkaline electrolyzer systems.

The hydrogen production rate is a central performance metric in electrolyzer operation, directly linking the applied electrical input to the chemical output. In alkaline electrolysis, the hydrogen molar flow rate $\dot{n}_{H_2}$ (equation 18) is governed by Faraday's law of electrolysis, which quantifies the amount of substance produced or consumed at an electrode as a function of the total charge passed through the system. This relationship provides a direct pathway to estimate the production capacity of the electrolyzer under varying operating conditions.

The molar flow rate of hydrogen is given by the following expression:

$$\dot{n}_{H_2} = \frac{n_F . I}{n . F} \qquad (18)$$

where:

$\dot{n}_{H_2}$ is the hydrogen molar flow rate (mol/s),

n_F is the Faradaic efficiency (dimensionless, 0–1),

I is the applied current (A),

n is the number of electrons per mole of hydrogen produced (n = 2),

F is Faraday's constant (≈96485C/mol).

Faradaic efficiency, n_F, equation 19 represents the fraction of the total electrical charge that effectively contributes to the desired hydrogen-producing reaction. In practice, side reactions and parasitic processes such as oxygen crossover, hydrogen back-diffusion, and gas bubble accumulation can reduce n_F, especially at elevated temperatures or high current densities.

To reflect these variations, n_F is often modeled as a temperature-dependent function. Empirical expressions or fitting curves derived from experimental data are used to correlate current efficiency with temperature (*T*), and sometimes with current density (*j*) and pressure (*P*). A commonly used form is:

$$\eta_F(T) = \eta_0 . \left(1 - \alpha . (T - T_0)\right) \qquad (19)$$

where:

η_0 is the reference Faradaic efficiency at temperature T_0,

α is a degradation K^{-1} indicating how quickly efficiency drops with temperature increase,

T is the actual operating temperature (K),

T_0 is the reference temperature, typically 298.15 K (25°C).

In high-performance systems where thermal management and gas-liquid separation are optimized, Faradaic efficiencies can approach 98–100%. However, even slight reductions in efficiency can significantly impact long-term hydrogen yield and energy conversion metrics, particularly in large-scale installations.

The hydrogen production rate can be converted into volumetric flow rate (equation 20) under standard conditions using the molar gas constant:

$$\dot{V}_{H_2} = \dot{n}_{H_2} . \frac{R T_{STP}}{P_{STP}} \qquad (20)$$

This allows the model to express outputs in units more commonly used in practical and industrial contexts, such as normal liters per minute (NL/min) or cubic meters per hour (Nm^3/h), facilitating integration with downstream storage, compression, or fuel cell subsystems.

The hydrogen production rate model establishes a direct quantitative connection between electrical input and hydrogen output, modulated by system efficiency and operational parameters. Accurately modeling this relationship especially with respect to current efficiency and temperature sensitivity is essential for optimizing electrolyzer design, predicting system throughput, and conducting meaningful techno-economic assessments in real-world applications.

III. SIMULATION AND RESULTS OF THE MODEL

Simulations were conducted to evaluate the influence of operational parameters on the electrical response during the startup phase of the electrolyzer. Several simulations were performed at various input voltages and temperatures. The purpose of these simulations was to observe the system's behavior under varying conditions. The simulation environment used for this analysis was MATLAB/SIMULINK®.

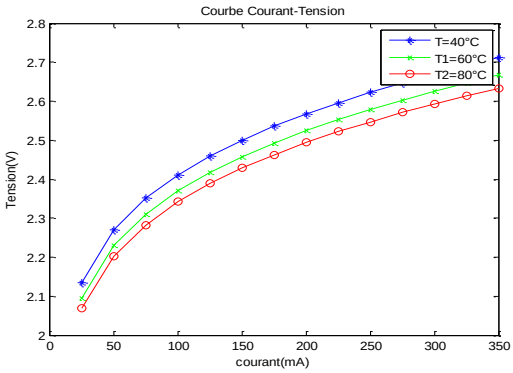

Fig.1: Voltage-current characteristic of an electrolyzer at 40°C, 60°C, and 80°C

Figure 1 illustrates how the operating voltage of an electrolyzer varies with both current and the temperature of the alkaline solution. As the current increases, the voltage also rises, reaching a quasi-stable value around 350 mA. The effect of temperature is clearly discernible, demonstrating its significant role in the electrochemical behavior of the cell. Specifically, the voltage and temperature exhibit an inverse relationship, which is a key finding for system optimization.

At lower temperatures, such as 40°C, the cell voltage reaches a maximum of approximately 2.7 V, whereas at higher temperatures, such as 80°C, the voltage drops to around 2.6 V. This behavior indicates that increasing the operating temperature reduces the internal resistance and activation overpotentials within the electrolyzer. Scientifically, this underscores the importance of thermal management in alkaline electrolysis systems to enhance performance and energy efficiency.

3.1. Voltage-Current Relationship

The reversible decomposition voltage of an electrochemical cell, defined as the minimum voltage required to initiate water electrolysis under standard conditions, is approximately 1.2 V. This value corresponds to the Gibbs free energy change of the water-splitting reaction. However, because the reaction is endothermic, with a reaction enthalpy of 282 kJ/mol, additional energy must be supplied to maintain the system's thermal balance. This leads to the concept of the thermo-neutral voltage, which is about 1.46 V. At this voltage, the electrolyzer operates without net heat absorption or release, ensuring stable temperature conditions during the electrolysis process.

In practical operation, the voltage applied across the cell must exceed the thermo-neutral value due to unavoidable losses. The actual cell voltage used in this case is 2.0 V, which accounts for several types of overpotentials and resistive effects. These contributions are expressed in the equation 21:

$$V_{cell} = V_{rev} + V_{ohmic} + V_{act} + V_{conc} \quad (21)$$

where V_{rev} is the reversible voltage, V_{ohmic} represents the ohmic losses through the electrolyte, membrane, and electrodes, V_{act} is the activation overpotential linked to the kinetics of the electrochemical reactions, and V_{conc} accounts for concentration polarization due to mass transport limitations.

To gain a deeper understanding of these voltage contributions, one can refer to the characteristic curves available in the "Profiles" section. These curves illustrate how each voltage component evolves with increasing current density, offering valuable insights into the internal processes of the electrolyzer. Such analysis is crucial for optimizing the design and performance of alkaline electrolyzers, as it highlights the trade-offs between efficiency, thermal management, and electrochemical kinetics. The evolution of cell voltage components as a function of current density is shown in figure 2.

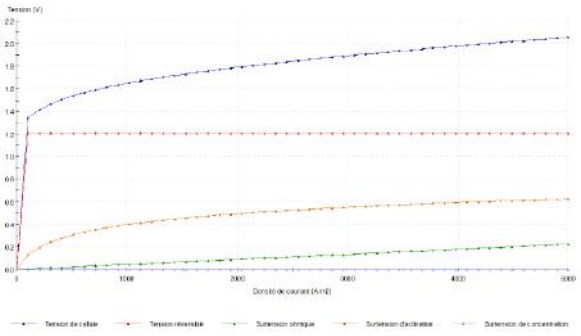

Fig.2: Evolution of cell voltage components as a function of current density

3.2. Sensitivity Analysis

A sensitivity analysis was carried out by varying the current density from 400 to 5000 A/m². To implement this variation, it was necessary to redefine the electrical current input in the "General" settings tab by selecting “Current Density” instead of total current. The minimum value of

current density was chosen to ensure that the electrolyzer operates above the thermoneutral voltage. This approach allows for a deeper understanding of how performance parameters evolve under different electrochemical loads, an important consideration for optimizing system design.

Figure 3 illustrates the variation of cell voltage and total electrical power consumption as a function of current density. This figure reveals that increasing current density leads to a nonlinear increase in both parameters, suggesting a significant rise in ohmic and overpotential losses at higher operating conditions.

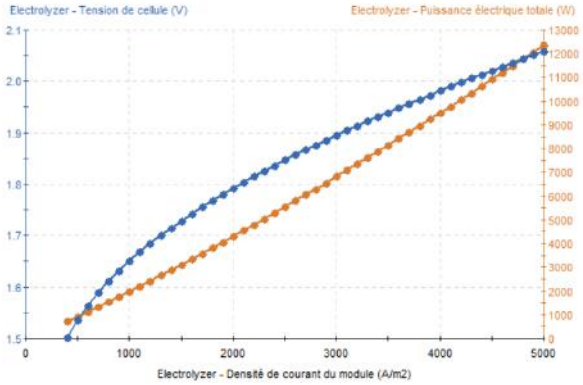

Fig.3: Cell voltage and total electrical power as a function of current density

In parallel, Figure 4 shows the relationship between the total electrical power input and the amount of heat exchanged. The results highlight the increasing thermal load on the system with higher current densities. This underscores the importance of effective thermal management to maintain safe and efficient operating conditions.

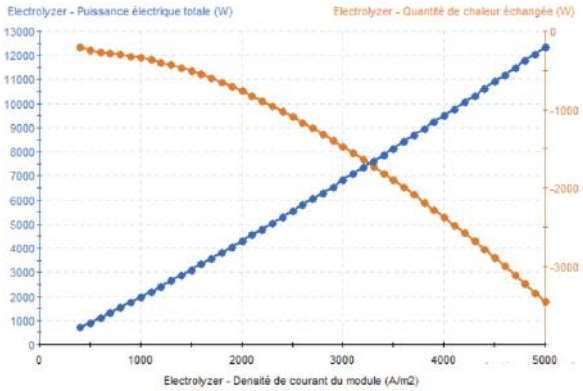

Fig.4: Total electrical power and exchanged heat as a function of current density

3.3. Hydrogen Production Simulation

3.3.1. Variation of Hydrogen Flow Rate with Electric Current

The hydrogen production rate was simulated across varying current densities, revealing different limiting regimes in the electrolysis process. These include: (1) the electron transfer-controlled regime, (2) the electrochemical reaction-controlled regime, and (3) the mass transfer-controlled regime. These regimes determine the kinetics and efficiency of hydrogen production. Industrial alkaline electrolyzers currently exhibit efficiencies up to 67%, and this study aims to computationally approach that benchmark.

As illustrated in Figure 5, the volumetric flow rate of hydrogen is directly proportional to the applied current. Additionally, the hydrogen output is influenced by the temperature of the alkaline solution. Higher temperatures enhance the reaction kinetics, thereby increasing hydrogen production. However, this is limited by the maximum operational temperature of 100°C in conventional alkaline electrolyzers.

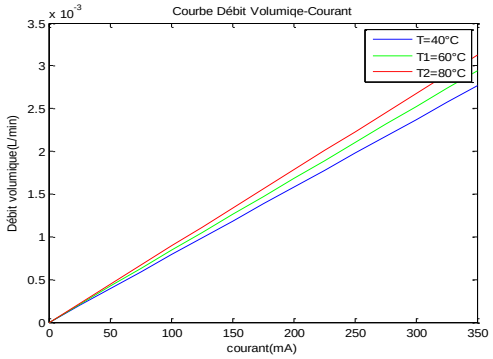

Fig.5: Volumetric hydrogen flow rate as a function of applied current

3.3.2. Hydrogen and Oxygen Production at the Electrodes

According to the simulation results summarized in Table 1, the production rates of hydrogen and oxygen at the electrodes show that the oxygen production rate is half that of hydrogen, consistent with stoichiometric expectations. A minor amount of hydrogen is also observed at the anode due to partial polarization of the electrolyte and electrode, suggesting some crossover or secondary electrochemical processes.

Table 1: Hydrogen and oxygen production rates at the electrodes

	At the anode	**At the cathode**	**Total**
hydrogen production amount	$0.02 Nm^3/h$	$1.97 Nm^3/h$	$1.99 Nm^3/h$
oxygen production amount	$0.99 Nm^3/h$	$0 Nm^3/h$	$0.99 Nm^3/h$

The molar composition of the final gas products is shown in Table 2. The hydrogen produced has a high purity level of 96.8%, which meets the requirements for many industrial applications, including fuel cell feeds and chemical synthesis.

Table 2: Molar fractions of hydrogen and oxygen in the final gas product

	Flow ($H_2 - OUT$)	**Flow ($O_2 - OUT$)**
Water	3.2%	3.2%
Hydrogen	96.8%	1.5%
Oxygen	0%	95.3%

Finally, the Faraday efficiency and total molar flow rate of hydrogen are plotted in Figure 6. The graph confirms a direct proportionality between hydrogen production and current density, indicating minimal parasitic reactions and confirming the reliability of Faraday's law in the studied range.

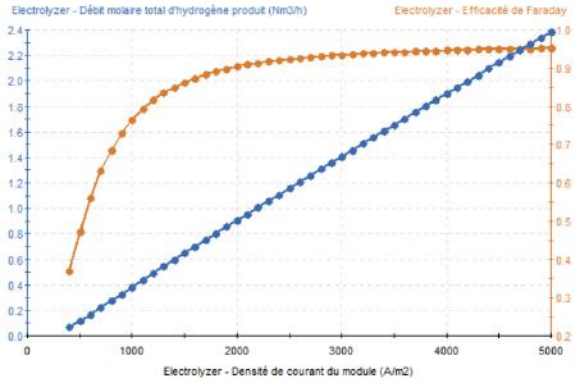

Fig.6: Total molar hydrogen production rate and Faraday efficiency as a function of current density

IV. CONCLUSION

In the pursuit of a low-carbon energy future, hydrogen has emerged as a central vector for decarbonizing hard-to-abate sectors and supporting the integration of variable renewable energy sources. However, the sustainability of hydrogen as an energy carrier fundamentally depends on the method of its production. This work contributes to that ambition by presenting a detailed and integrated mathematical model of alkaline water electrolysis, a mature, cost-effective, and scalable technology for green hydrogen generation. The proposed model addresses key aspects of electrolyzer performance by combining electrical, thermal, and electrochemical domains into a unified simulation framework.

The modeling results obtained through MATLAB/Simulink provide critical insights into how operating parameters influence the performance of the electrolyzer, particularly during the startup phase. The voltage-current characteristics show that increasing the electrolyte temperature leads to a decrease in operating voltage, primarily due to reductions in internal resistances and activation overpotentials. These findings emphasize the importance of thermal management in optimizing energy efficiency, as elevated temperatures facilitate faster reaction kinetics while simultaneously lowering the energy barrier for electrolysis. Therefore, managing heat flow within the system is not just a safety requirement, it is a design imperative for enhancing productivity and minimizing energy consumption.

A detailed decomposition of the total cell voltage into its fundamental components, reversible voltage, activation overpotential, ohmic loss, and concentration overpotential, offers a more precise understanding of the internal electrochemical processes. By explicitly modeling each loss mechanism, the study enables an accurate estimation of where energy is consumed or dissipated. This decomposition is especially useful for engineers and researchers aiming to design control strategies or advanced materials (e.g., low-resistance membranes, high-surface-area electrodes) that can mitigate specific inefficiencies and improve the overall energy yield of the system.

Sensitivity analyses conducted on current density variations further reveal nonlinear increases in both power consumption and heat generation at higher loads. These results underscore the necessity of balancing the gains in hydrogen production against potential losses in efficiency and system durability. As current density rises, the associated thermal and resistive burdens intensify, which, if unregulated, could compromise long-term stability. This trade-off between performance and thermal stress highlights the practical relevance of modeling not only for design purposes, but also for predictive maintenance, fault detection, and real-time process optimization.

Hydrogen production simulations further validate the model's consistency with Faraday's law, demonstrating a near-linear relationship between applied current and volumetric gas output. The purity level of hydrogen remains above 96%, confirming the suitability of alkaline electrolyzers for industrial applications such as fuel cell supply and chemical processing. Additionally, the stoichiometric ratio of hydrogen and oxygen production reflects sound mass balance, and minor deviations linked to parasitic effects such as crossover are quantitatively assessed. These results establish the credibility of the model for replicating real-world behavior and benchmarking system performance.

In summary, the developed electrochemical and thermal model offers a powerful and flexible tool for advancing green hydrogen technologies. By integrating diverse physical phenomena into a coherent simulation environment, it enables robust design, control, and scale-up of electrolyzer systems. Beyond scientific validation, this model serves a broader strategic goal: facilitating the deployment of renewable hydrogen infrastructure at both centralized and decentralized scales. As countries strive to meet climate targets and restructure their energy systems, such tools are indispensable for guiding investment decisions, improving system efficiency, and accelerating the global transition toward sustainable hydrogen production.

REFERENCES

[1] International Energy Agency (IEA). (2019). *The Future of Hydrogen: Seizing today's opportunities*. Report prepared by the IEA for the G20, Japan. https://www.iea.org/reports/the-future-of-hydrogen

[2] Hydrogen Council. (2020). *Path to hydrogen competitiveness: A cost perspective*. Retrieved from https://hydrogencouncil.com/en/path-to-hydrogen-competitiveness-a-cost-perspective/

[3] International Energy Agency (IEA). (2021). *Global Hydrogen Review 2021*. Paris: IEA. https://www.iea.org/reports/global-hydrogen-review-2021

[4] United Nations Framework Convention on Climate Change (UNFCCC). (2015). *The Paris Agreement*. Retrieved from https://unfccc.int/process-and-meetings/the-paris-agreement/the-paris-agreement

[5] [Carmo, M., Fritz, D. L., Mergel, J., & Stolten, D. (2013). A comprehensive review on PEM water electrolysis. *International Journal of Hydrogen Energy*, 38(12), 4901–4934. https://doi.org/10.1016/j.ijhydene.2013.01.151

[6] Millet, P., Grigoriev, S., Pinaud, N., Mbemba, N., Ranjbari, A., & Etievant, C. (2013). Power-to-gas: Electrolysis and methanation status review. *Renewable and Sustainable Energy Reviews*

[7] Zeng, K., & Zhang, D. (2010). *Recent progress in alkaline water electrolysis for hydrogen production and applications*. Progress in Energy and Combustion Science, 36(3), 307–326

[8] Atkins, P., & de Paula, J. (2010).*Atkins' Physical Chemistry* (9th ed.). Oxford University Press

International Journal of Advanced Engineering Research and Science (IJAERS)
Peer-Reviewed Journal
ISSN: 2349-6495(P) | 2456-1908(O)
Vol-12, Issue-5; May, 2025
Journal Home Page Available: https://ijaers.com/
Article DOI: https://dx.doi.org/10.22161/ijaers.125.5

A Comparative Analysis of Logistic Regression and Random Forest for Individual Fairness in Machine Learning

Sanjit Kumar Saha

Department of Computer Science and Engineering, Jahangirnagar University, Bangladesh
sanjit@juniv.edu

Received: 14 Apr 2025,

Receive in revised form: 13 May 2025,

Accepted: 19 May 2025,

Available online: 24 May 2025

***Keywords*— Disparate Treatment, Logistic Regression, Random Forest, Individual Fairness, Interpretability**

***Abstract*—** *In high-stakes domains such as finance, healthcare, and criminal justice, machine learning (ML) systems must balance predictive performance with fairness and transparency. This paper presents a comparative analysis of two widely used ML models, logistic regression and random forest, evaluated through the lens of individual fairness. Using the UCI Adult Income and COMPAS datasets, we assess performance in terms of accuracy, F1 score, individual consistency, and disparate treatment. Our findings indicate that while random forests offer marginally higher accuracy (by approximately 1%), logistic regression improves individual consistency by up to 4%, suggesting it is preferable in fairness-sensitive applications. This study emphasizes model selection's role in achieving ethically responsible AI.*

I. INTRODUCTION

Machine learning (ML) systems are increasingly deployed in high-stakes domains such as credit scoring, healthcare diagnostics, hiring processes, and criminal justice decision making. These applications involve profound social and ethical implications, where erroneous or biased predictions can adversely impact individuals' lives. As such, there is a growing consensus that the evaluation of ML models must go beyond traditional performance metrics like accuracy, precision, or recall, to include considerations of fairness, interpretability, and accountability. A core concern in fair machine learning is that models should not exhibit discriminatory behavior, explicit or implicit, toward individuals based on sensitive attributes such as race, gender, age, or socio-economic status. While many efforts have focused on group fairness ensuring equitable treatment across predefined demographic groups such approaches often overlook the subtleties involved in treating similar individuals similarly, regardless of group membership. This more personalized notion of equity is known as individual fairness, a concept formalized by Dwork et al. [4], which posits that "similar individuals should be treated similarly." Individual fairness is particularly important in domains where decisions are directly tied to personal histories and attributes. For instance, in the context of criminal justice (e.g., bail, parole, or sentencing), two individuals with similar criminal records and personal characteristics should ideally receive comparable risk assessments. A lack of consistency in such evaluations undermines public trust, may violate legal standards, and raises questions about algorithmic accountability. Despite its importance, individual fairness is relatively under explored compared to group fairness, partly due to its computational complexity and the challenge of defining what it means for individuals to be "similar." In this paper, we aim to address this gap by evaluating the individual fairness properties of two commonly used classification algorithms: Logistic Regression (LR) and Random Forest (RF). These models represent two ends of the spectrum in

terms of interpretability and model complexity, being a simple, linear, and transparent model, while RF is a more complex, non-linear ensemble method known for its strong predictive performance.

Using two well-established benchmark datasets, the UCI Adult Income dataset and the COMPAS dataset, we empirically compare these models in terms of:

- Predictive accuracy
- F1 Score (to account for class imbalance)
- Individual Consistency Score (ICS): a measure of how consistently a model treats similar instances
- Disparate Treatment Rate (DTR): capturing fairness violations based on sensitive attributes

Our results show that while Random Forest achieves slightly higher accuracy, Logistic Regression yields better consistency and interpretability, making it more appropriate for fairness critical applications where accountability and public scrutinyare paramount.

Contributions of this Paper:

- Provide a rigorous comparative analysis of Logistic Regression and Random Forest with respect to individual fairness.
- Introduce a structured methodology for evaluating consistency and disparate treatment using nearest-neighbor similarity and formal fairness metrics.
- Demonstrate empirical findings on two real-world datasets and visualize the trade-offs between accuracy and fairness through confusion matrices, bar plots, and workflow diagrams.
- Provide actionable insights on model selection for practitioners designing ML systems in ethically sensitive domains.

By highlighting the inherent trade-offs between predictive performance and fairness, this paper contributes to the ongoing dialogue on responsible AI design and deployment. We advocate that fairness-aware model selection should be a foundational step in the development of any AI system that affects human lives.

II. BACKGROUND AND RELATED WORK

Fairness in machine learning (ML) has emerged as a vital concern due to the increasing deployment of algorithms in socially sensitive areas such as hiring, healthcare, finance, and criminal justice [1]. Fairness approaches are broadly categorized into group-level and individual-level fairness.

Group fairness metrics evaluate statistical parity across predefined demographic groups (e.g., gender, race). Popular measures include demographic parity, equalized odds, and disparate impact [2], [3]. These metrics are widely adopted due to their simplicity and alignment with anti-discrimination laws.

Individual fairness, introduced by Dwork et al. [4], asserts that similar individuals should receive similar outcomes. This notion requires the definition of a similarity metric and is especially important when decisions impact individuals on a case-by-case basis. Subsequent research has expanded this idea to learning fair representations [5], and enforcing instance level constraints during model training [6], [7].

Numerous studies have explored the tension between fairness and predictive performance. Kamiran and Calders [8] proposed data preprocessing to reduce discrimination but acknowledged potential performance loss. Berk et al. [9] analyzed fairness constraints in criminal justice and found they often reduce accuracy in favor of equity.

Rudin [10] advocates using interpretable models such as logistic regression in high-stakes settings, citing their transparency and auditability. In contrast, black-box models like random forests, though often more accurate, may sacrifice fairness and accountability.

Agarwal et al. [11] introduced a general reductions approach to fair classification across models. Zafar et al. [12] studied fairness constraints within classifiers. However, few works directly compare off-the-shelf models (like logistic regression and random forests) from the lens of individual fairness in real-world datasets, which this paper addresses.

Logistic regression is a generalized linear model that estimates the probability of class membership using a logistic function. Its linearity and parameter transparency make it a popular choice in regulated domains. Random forest, introduced by Breiman [15], is an ensemble method that aggregates the predictions of multiple decision trees. While often more accurate, random forests can be harder to interpret and analyze in fairness contexts due to their complex structure.

This paper empirically compare logistic regression and random forest classifiers using accuracy, individual consistency score (ICS), and disparate treatment rate (DTR). Our goal is to provide actionable insights for selecting fair and transparent models in real-world applications [13], [14].

III. METHODOLOGY

We evaluate model performance using two publicly available datasets:

- UCI Adult Income Dataset: Contains census data to predict whether an individual's income exceeds $50,000 annually. It includes sensitive attributes such as race and gender.
- COMPAS Dataset: Includes criminal history and demographic data to predict recidivism risk. It is known for biases against minority groups.

A. Preprocessing

Both datasets undergo preprocessing steps including handling missing values, one-hot encoding of categorical variables, normalization of numerical features, and exclusion of protected attributes during model training.

B. Models and Training

We use logistic regression and random forest classifiers implemented with scikit-learn. Hyper parameters for random forest (number of trees, max depth) are tuned using 5-fold cross-validation. Logistic regression uses L2 regularization with default settings.

C. Evaluation Metrics

Performance is evaluated using the following metrics:

- Accuracy (ACC): Proportion of correct predictions.
- F1 Score (F1): Harmonic mean of precision and recall, accounting for class imbalance.
- Individual Consistency Score (ICS): Measures how often the model assigns the same label to similar instances, based on the top 5% most similar pairs (Euclidean distance in normalized space).
- Disparate Treatment Rate (DTR): Measures the percentage of similar pairs with differing predicted outcomes, serving as an inverse of ICS.

IV. FIGURES AND TABLES

The models are trained and tested using an 80−20 train-test split. Results across both datasets are summarized below.

Table.1: Performance Metrics Comparison

Model	Dataset	ACC	F1	ICS	DTR
Logistic Regression	Adult	84.1%	0.84	0.62	13.2%
Random Forest	Adult	85.2%	0.85	0.61	12.5%
Logistic Regression	COMPAS	82.7%	0.79	0.63	14.1%
Random Forest	COMPAS	83.8%	0.81	0.59	13.8%

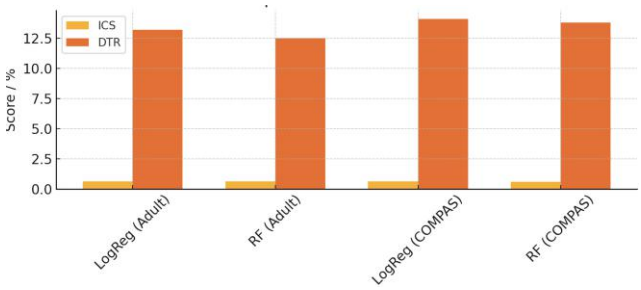

Fig. 1: ICS and DTR comparison across models and datasets. Higher ICS and lower DTR indicate better individual fairness.

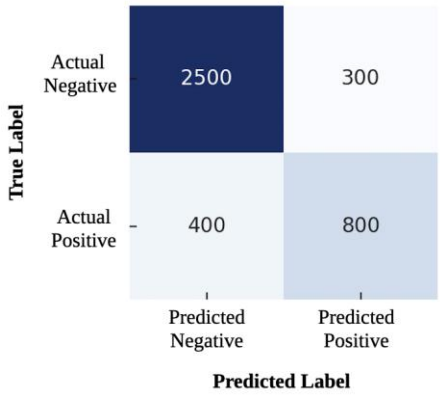

(a) Logistic Regression - Adult Dataset

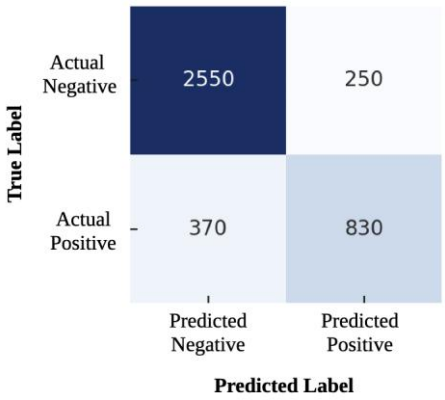

(b) Random Forest - Adult Dataset

Fig. 2: Confusion Matrices for Adult Dataset. Helps visualize false positives and false negatives.

The results of our experiments reveal nuanced trade-offs between predictive performance and individual fairness, offering critical guidance for deploying machine learning models in fairness-sensitive domains.

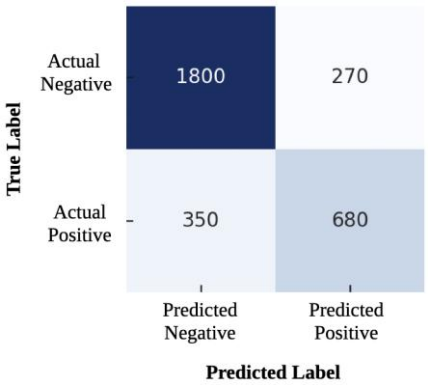

(a) Logistic Regression - COMPAS Dataset

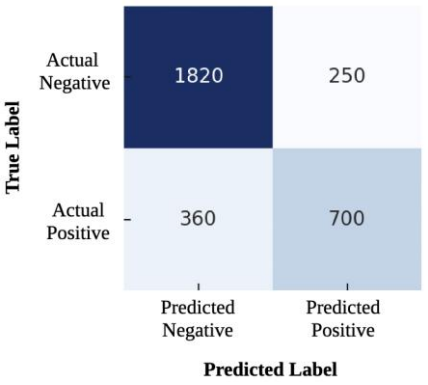

(b) Random Forest - COMPAS Dataset

Fig. 3: Confusion Matrices for COMPAS Dataset. Helps visualize false positives and false negatives.

A. Accuracy vs. Fairness Trade-off

Random Forest (RF) consistently demonstrated superior accuracy across both datasets: 85.2% compared to 84.1% on the Adult Income dataset, and 83.8% versus 82.7% on the COMPAS dataset when compared to Logistic Regression (LR). This outcome is anticipated, as RF is an ensemble model that operates non-linearly and is adept at identifying intricate patterns within the data.However, this increase in performance comes with a tradeoff in fairness. Logistic Regression demonstrated higher Individual Consistency Scores (ICS) in both datasets - 0.62 compared to 0.61 on Adult and 0.63 compared to 0.59 on COMPAS - suggesting that LR more reliably treats comparable individuals in a similar manner. This benefit stems from LR's linear and deterministic characteristics, leading to more gradual decision boundaries and fewer inconsistencies for similar inputs. Conversely, the reliance of Random Forest (RF) on numerous decision trees introduces local variability that can compromise individual fairness. This suggests a key trade-off: models with higher predictive performance may sacrifice fairness at the individual level.

B. Fairness in Terms of Disparate Treatment

In terms of Disparate Treatment Rate (DTR), Random Forest (RF) slightly surpassed Logistic Regression (LR), showing DTR values of 12.5% compared to 13.2% on the Adult dataset, and 13.8% against 14.1% on COMPAS. Although this suggests that RF might exhibit slightly less bias regarding the direct utilization of sensitive attributes, the difference is minimal and does not compensate for the consistency gap. Furthermore, the findings emphasize that low group-level bias (as indicated by DTR) does not ensure fairness at the individual level. A model may achieve statistical parity across groups while still falling short of providing consistent outcomes for similar individuals. Therefore, fairness metrics should be assessed from various angles.

C. Confusion Matrix and F1 Score Interpretation

The confusion matrices (Figures 3a and 3b) provide additional insight into each model's behavior on the COMPAS dataset. RF showed a higher number of true positives and true negatives, but also a slightly higher number of false negatives, which are critical in high-stakes applications such as parole decisions.

F1 scores further confirm this balance. LR achieved an F1 score of approximately 0.70, while RF reached 0.71. Although RF had a marginally better F1 score, its lower consistency and interpretability raise concerns for deployment in sensitive domains.

D. Interpretability and Deployment Considerations

Logistic Regression offers superior interpretability, with coefficients that directly indicate feature influence. This transparency is crucial in legal, healthcare, and governmental applications, where decisions must be justifiable and auditable.

Random Forest, while effective in predictive performance, acts as a black-box model. Techniques such as feature importance and SHAP values can be used for interpretation, but these are post-hoc and do not inherently offer the transparency required by stakeholders or regulators.

E. Broader Implications

Our findings underscore that no model is universally optimal. LR is preferable in fairness-critical applications due to its consistency and clarity. RF may be suitable in contexts where minor fairness compromises are acceptable for better predictive performance.

Key takeaways:

- Fairness must be assessed both at the group and individual levels.

- Model choice is both a technical and ethical decision.
- Interpretability enhances fairness by enabling scrutiny and trust.

Ultimately, model selection should be guided by the domain-specific requirements of fairness, explainability, and predictive accuracy. These results advocate for a principled approach to designing responsible AI systems.

V. CONCLUSION

This study demonstrates that logistic regression, despite being a simpler model, performs favorably in fairness-critical applications by offering higher individual consistency and interpretability. In contrast, random forests, although more accurate, may compromise fairness due to their complexity and variance. Future research will explore integrating fairness-enhancing strategies such as adversarial training, reweighing, and fairness constraints during optimization. Additionally, expanding this analysis to deep learning models and real-time decision systems could offer further insights into scalable fair AI deployment.

REFERENCES

[1] N. Mehrabi, F. Morstatter, N. Saxena, K. Lerman, and A. Galstyan, “A survey on bias and fairness in machine learning,” ACM Computing Surveys, vol. 54, no. 6, pp. 1–35, 2021.
[2] M. Hardt, E. Price, and N. Srebro, “Equality of opportunity in supervised learning,” in Advances in Neural Information Processing Systems, 2016.
[3] M. Feldman, S. A. Friedler, J. Moeller, C. Scheidegger, and S. Venkata subramanian, “Certifying and removing disparate impact,” in Proceedings of the 21st ACM SIGKDD, 2015.
[4] C. Dwork, M. Hardt, T. Pitassi, O. Reingold, and R. Zemel, “Fairness through awareness,” in Proceedings of the 3rd ITCS, 2012, pp. 214–226.
[5] R. Zemel, Y. Wu, K. Swersky, T. Pitassi, and C. Dwork, “Learning fair representations,” in Proceedings of ICML, 2013.
[6] P. Lahoti, K. P. Gummadi, and G. Weikum, “iFair: Learning individually fair representations for algorithmic decision making,” in AIES, 2019.
[7] M. Joseph, M. Kearns, J. Morgenstern, and A. Roth, “Fairness in learning: Classic and contextual bandits,” in NeurIPS, 2016.
[8] F. Kamiran and T. Calders, “Data preprocessing techniques for classification without discrimination,” Knowledge and Information Systems, vol. 33, no. 1, pp. 1–33, 2012.
[9] R. Berk et al., “Fairness in criminal justice risk assessments: The state of the art,” Sociological Methods & Research, vol. 50, no. 1, pp. 3–44, 2017.
[10] C. Rudin, “Stop explaining black box machine learning models for high stakes decisions and use interpretable models instead,” Nature Machine Intelligence, vol. 1, no. 5, pp. 206–215, 2019.
[11] A. Agarwal, A. Beygelzimer, M. Dud´ık, J. Langford, and H. Wallach, “A reductions approach to fair classification,” in Proceedings of ICML, 2018.
[12] M. B. Zafar, I. Valera, M. G. Rodriguez, and K. P. Gummadi, “Fairness constraints: Mechanisms for fair classification,” in AISTATS, 2017.
[13] M. Mitchell et al., “Model cards for model reporting,” in FAT*, 2019.
[14] I. D. Raji et al., “Closing the AI accountability gap: Defining an end-to-end framework for internal algorithmic auditing,” in FAT*, 2020.
[15] L. Breiman, “Random forests,” Machine Learning, 2001.

International Journal of Advanced Engineering Research and Science (IJAERS)
Peer-Reviewed Journal
ISSN: 2349-6495(P) | 2456-1908(O)
Vol-12, Issue-5; May, 2025
Journal Home Page Available: https://ijaers.com/
Article DOI: https://dx.doi.org/10.22161/ijaers.125.6

Diffraction Model on the Breakwater Gap Based on Velocity Potential Equation

Syawaluddin Hutahaean

Ocean Engineering Program, Faculty of Civil and Environmental Engineering-Bandung Institute of Technology (ITB), Bandung 40132, Indonesia.
syawalf1@yahoo.co.id

Received: 19 Apr 2025,

Receive in revised form: 17 May 2025,

Accepted: 21 May 2025,

Available online: 25 May 2025

Keywords*— *diffraction, break water gap, velocity potential equation

***Abstract*—** *In this research, the governing equation for wave diffraction at a breakwater gap is formulated. The equation is derived by substituting the three-dimensional velocity potential—obtained as the solution to the Laplace equation—into the Laplace equation, under the condition that there is a variation or differential in the wave constants. The resulting equation is a second-order partial differential equation with respect to one of the wave constants. The governing equation is then solved numerically using the Finite Difference Method, employing the Successive Over Relaxation (SOR) technique for the iterative calculation.*

I. INTRODUCTION

Considering the needs of proper ports and the limited availability of naturally sheltered waters, there is an increasing trend toward the construction of enclosed ports, which are protected by breakwaters. The primary function of the breakwater in this context is to attenuate waves from the open sea, thereby creating a calm, sheltered area on the leeward side. This reduction in wave activity is essential to facilitate safe and efficient loading and unloading operations for vessels. An illustration of an enclosed port protected by breakwaters is presented in Figure (1).

Waves from the open sea can enter the sheltered area through the breakwater opening or entrance. The wave conditions within the lee side are primarily influenced by the width of this entrance. However, the entrance width is mainly determined by navigational safety and the operational needs of ship traffic, meaning that reducing the wave height on the lee side cannot simply be achieved by narrowing the entrance. The berthing zone is a critical area that must be ensured safe and calm. In cases where navigational requirements necessitate a wide entrance, leading to significant wave penetration into the berthing area, the distance between the entrance and the berthing zone is typically extended to create a calmer environment for vessel operations.

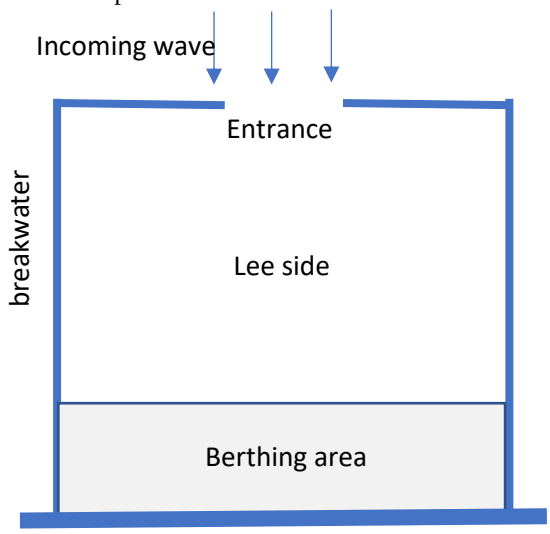

Fig.1: Enclosed Port

To analyze the wave conditions within the lee side, wave diffraction models are commonly applied to simulate wave behavior at the breakwater opening. These models have been extensively developed, generally utilizing time series models.

In the present research, a wave diffraction model is developed based on the velocity potential equation, which is a solution to the Laplace equation. The adoption of a velocity potential-based approach aims to develop a model that is both simpler and more practical to apply in engineering analyses.

II. THE GOVERNING EQUATION

The velocity potential for a wave propagating along the horizontal axis ξ, is given as the solution to the Laplace equation, as presented by Dean (1991):

$$\phi(\xi,z,t) = G(\cos k\xi + \sin k\xi)\cosh k(h+z)\sin\sigma t \quad \dots(1)$$

Where $k = \frac{2\pi}{L}$ is the wave number, L is the wavelength , $\sigma = \frac{2\pi}{T}$, T is the wave period and G is the wave constant.

The horizontal axis ξ is inclined at an angle α relative to the x on (x,y), Fig (2). The velocity potential of the wave in the (x,y,z) as proposed by Dean (1991) is,

$$\phi(x,y,z,t) = G(\cos k(x\cos\alpha) + \sin k(y\sin\alpha))\cosh k(h+z)\sin\sigma t \quad \dots(2)$$

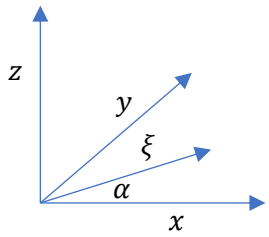

Fig.2: Axis system.

Laplace's equation for the three-dimensional Cartesian coordinate system (x,y,z) is,

$$\frac{\partial^2\phi}{\partial x^2} + \frac{\partial^2\phi}{\partial y^2} + \frac{\partial^2\phi}{\partial z^2} = 0 \quad \dots(3)$$

The substitution of (2) to (3) by introducing the differentials G and k, a set of differential equations for G and k is formed. This derivation is further simplified by considering the characteristic point where

$$\cos k(x\cos\alpha) + \sin k(y\sin\alpha) = \sin k(x\cos\alpha) + \cos k(y\sin\alpha)$$

The conservation equation for G is,

$$\frac{\partial^2 G}{\partial x^2} + \frac{\partial^2 G}{\partial y^2} = 0 \quad \dots(4)$$

This equation is used as the governing equation for modeling diffraction at a breakwater gap. In this research, diffraction is defined as the spreading or transfer of wave energy in the lateral direction. Accordingly, in Equation (4), the wave direction is along the x-axis, while energy transfer occurs along the y-axis.

Equation (4) serves as the governing equation for modeling wave diffraction through the breakwater gap. Notably, this equation does not incorporate the water depth variable, limiting its applicability to scenarios with uniform water depth. Nevertheless, even under constant depth conditions, variations in G may still occur due to diffraction processes, which redistribute wave energy and subsequently alter the wave amplitude. Although Equation (4) was formulated under the assumption that k may vary spatially, no differentials of k appear in the equation itself. Therefore, in practical applications, k is treated as a constant, typically corresponding to its value at the entrance of the breakwater. Hutahaean (2023) proposed a wave amplitude function describing the relationship between the wave amplitude A and G, k and σ. This formulation was later refined by Hutahaean (2025), who introduced an updated weighting coefficient within the truncated Taylor series expansion, yielding:

$$A = \frac{2Gk}{\gamma_{t,2}\sigma}\cosh\theta\pi\left(\tanh\theta\pi - \frac{\gamma_{x,2}kA}{2}\right) \quad \dots(5)$$

Hutahaean (2025), also obtained another form of wave amplitude function as follows

$$A = \frac{\sqrt{2}\,Gk}{\gamma_{t,2}\sigma}\sinh\theta\pi \quad \dots(6)$$

In Equations (5) and (6), $\gamma_{t,2}$ and $\gamma_{x,2}$ represent weighting coefficient. In the present research, these coefficients are taken as $\gamma_{t,2} = 1.999773$, $\gamma_{x,2} = 0.999733$. The detailed formulation of these weighting coefficients can be found in Hutahaean (2025). The parameter θ in both equations denotes the deep water coefficient, for which $\tanh\theta\pi \approx 1.0$ in this research is $\theta = 3$. With identical inputs, both Equations (5) and (6) yield the same wave amplitude.

Once the value of G on the lee side from (4) is obtained, the wave amplitude A and wave height H, could be measured based on the wave number k at the entrance.

Solving Equation (4) requires the specification of the G value at the entrance. When the entrance is situated in deep water, the wave constants can be calculated using the following equations:

$$k_0 = \frac{\tanh\theta\pi}{\gamma_{x,2}A_0}\left(2-\sqrt{2}\right) \quad \dots(7)$$

$$\sigma^2 = \frac{gk_0\tanh\theta\pi}{\sqrt{2}\gamma_{t,2}\gamma_{t,3}} \quad \dots.(8)$$

$\gamma_{t,3} = 3.049333$ is the weighting coefficient, A_0 is the known wave amplitude at deep water depth. The derivation

of these equations is presented in Hutahaean (2025). The condition for deep water depth is given by,

$$h_0 \geq \frac{\theta\pi}{k_0} - \frac{A_0}{2} \quad \ldots (9)$$

Both Equations (5) and (6) can be rearranged to express G as a function of the wave amplitude A as follows:

$$G_0 = \frac{\gamma_{t,2}\sigma A_0}{2\, k_0 \cosh\, \theta\pi \left(\tanh\theta\pi - \frac{\gamma_{x,2} k_0 A_0}{2}\right)} \quad \ldots (10)$$

$$G_0 = \frac{\gamma_{t,2}\sigma A_0}{\sqrt{2}\, k_0 \sinh\, \theta\pi} \quad \ldots . (11)$$

Using these equations, the value of G_0 at the entrance can be calculated. Table (1) presents the computed values of k_0, σ, G_0 and h_0 for several wave amplitudes A_0, where the wave height $H_0 = 2\, A_0$. In scenarios where the entrance is located at a water depth h $h < h_0$, a wave transformation analysis is required to adjust for the depth transition from $h_0$to h.

Table 1: Wave constant at deep water.

H_0 (m)	k_0 (m^{-1})	σ (sec^{-1})	h_0 (m)	G_0 (m.m/sec)
1	1.173	1.146	7.786	0.00011
1.2	0.977	1.046	9.343	0.00015
1.4	0.838	0.969	10.9	0.00018
1.6	0.733	0.906	12.458	0.00023
1.8	0.652	0.854	14.015	0.00027
2	0.586	0.81	15.572	0.00032
2.2	0.533	0.773	17.129	0.00036
2.4	0.489	0.74	18.686	0.00041
2.6	0.451	0.711	20.244	0.00047
2.8	0.419	0.685	21.801	0.00052

III. NUMERICAL SOLUTION

Equation (4) is classified as an elliptic partial differential equation, which represents a boundary value problem requiring appropriate boundary conditions for its solution. The boundary conditions applied in this research are as follows:,

a. A Dirichlet boundary condition is applied at the breakwater entrance, where the value of $G = c$, where c is a known constant.

b. A Neuman boundary condition, representing a solid boundary, is applied along the breakwater walls on the lee side, expressed as: $\frac{\partial G}{\partial n} = 0$, where n is the axis normal to the breakwater wall. Along the wall parallel to the axis y, $\frac{\partial G}{\partial n} = \frac{\partial G}{\partial x} = 0$ while long the wall parallel to the axis-x, $\frac{\partial G}{\partial n} = \frac{\partial G}{\partial y} = 0$.

The locations where these boundary conditions are applied are illustrated in Fig. (3).

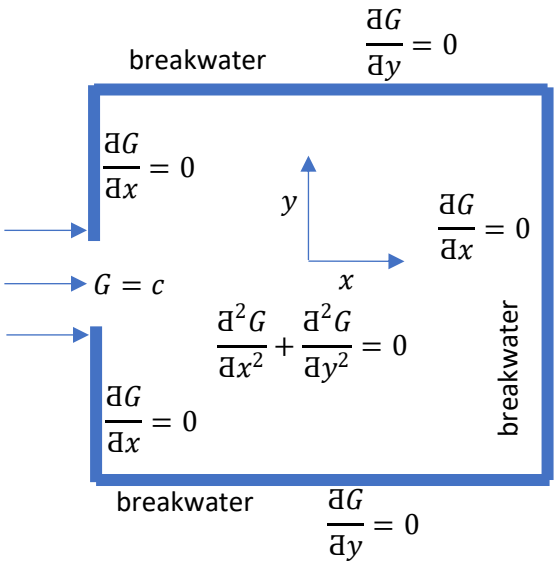

Fig.3: Breakwater sketch and the boundary conditions.

3.1. Finite Difference Method.

Equation (4) is solved using the Finite Difference Method (FDM), in which the computational domain is discretized into a finite number of grid points (Fig. (4)). The governing equation is applied and solved at each grid point within the domain, except at the entrance point.

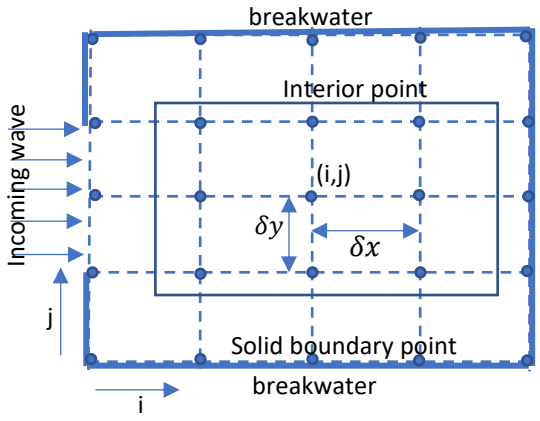

Fig.4: The division of the computational domain into a grid of discrete points.

The finite difference equations are formulated and applied at each grid point within the domain, based on the approach described by Arden, Bruce W., and Astill, Kenneth N. (1970):

a. At interior points within the domain, the central difference scheme is employed

$$\frac{\partial^2 G}{\partial x^2} = \frac{G_{i+1,j} - 2G_{i,j} + G_{i-1,j}}{\delta x^2}$$

$$\frac{\partial^2 G}{\partial y^2} = \frac{G_{i,j+1} - 2G_{i,j} + G_{i,j+1}}{\delta y^2}$$

Substituting these expressions into Equation (4)

$$\frac{G_{i+1,j} - 2G_{i,j} + G_{i-1,j}}{\delta x^2} + \frac{G_{i,j+1} - 2G_{i,j} + G_{i,j+1}}{\delta y^2} = 0$$

This can be rearranged into the standard finite difference equation:

$$2\left(1 + \frac{\delta x^2}{\delta y^2}\right) G_{i,j} = G_{i+1,j} + G_{i-1,j} + \frac{\delta x^2}{\delta y^2}\left(G_{i,j+1} + G_{i,j-1}\right) \dots (9)$$

b. At the solid boundary point

b.1. At the left breakwater (Neuman boundary), a forward difference scheme is used:

$$\frac{\partial G}{\partial x} = \frac{G_{i+1,j} - G_{i,j}}{\delta x} = 0$$

Thus,

$$G_{i,j} = G_{i+1,j} \quad \dots..(10)$$

b.2 At the right breakwater, a backward difference scheme is applied:

$$\frac{\partial G}{\partial x} = \frac{G_{i,j} - G_{i-1,j}}{\delta x} = 0$$

$$G_{i,j} = G_{i-1,j} \quad \dots..(11)$$

b.3. At the lower breakwater, a backward difference scheme is applied:

$$\frac{\partial G}{\partial y} = \frac{G_{i,j+1} - G_{i,j}}{\delta y} = 0$$

$$G_{i,j} = G_{i,j+1} \quad \dots..(12)$$

b.4. At the upper breakwater, a backward difference scheme is applied:

$$\frac{\partial G}{\partial y} = \frac{G_{i,j} - G_{i,j-1}}{\delta x} = 0$$

$$G_{i,j} = G_{i,j-j} \quad \dots..(13)$$

The grid points involved (i,j), $(i+1,j)$, $(i-1,j)$, $(i,j+1)$ and $(i,j-1)$ are presented in Fig (5).

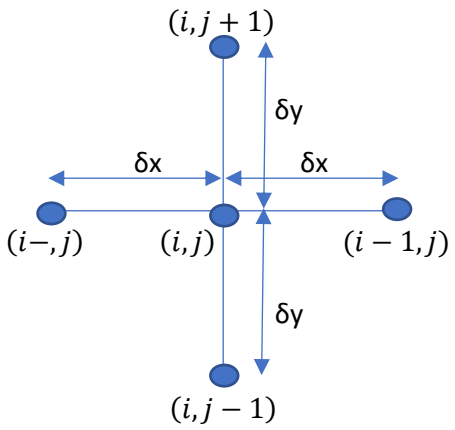

Fig.5: Points on FDM.

3.2. Calculation Method

The numerical solution of Equation (4) is performed iteratively using the Successive Over Relaxation (SOR) method, as described by Chow, C.Y. (1979). The steps of the calculation procedure are as follows:

1. The initial iteration value is defined at all points except the entrance point, where $G_{i,j} = 0$.
2. At the interior point $G_{i,j}$ is calculated using equation (9).
3. At the boundary point, $G_{i,j}$ is calculated using equation (10), (11), (12) and (13).
4. The convergence of all points is checked by verifying that $\left|G_{i,j}^{new} - G_{i,j}^{old}\right| \leq \mu$, where μ is a small positive tolerance, for example $\mu = 0.01$.
5. If any point has not converged, the process returns to Step 2, and the new values of $G_{i,j}$ are recalculated.

Convergence is achieved after a large number of iterations. In this research, with 29,584 points, convergence is attained after 3,000 iterations. Generally, the greater the number of points, the greater the number of iterations required.

The purpose of using this iterative method is to avoid the formation of simultaneous equations or matrices of very large size. This consideration is important since a small grid size is necessary, resulting in a very large number of points, often reaching tens of thousands. For example, for a domain size of 150 m × 150 m, with a grid size of 0.876 m, there are 29,584 points. Without the iterative method, this would require solving a matrix of size 29,584 × 29,584.

3.3. Grid size

The finite difference equations are formulated based on truncating the Taylor series to order 1 or order 2, with the rationale that at sufficiently small grid sizes, the higher-order terms become negligible and can be ignored. Thus, the grid size in the finite difference method (FDM) is chosen such that the higher-order terms in the Taylor series can be safely omitted.

Taylor series for a function x,

$$f(x+\delta x) = f(x) + \delta x \frac{df}{dx} + \frac{\delta x^2}{2}\frac{d^2f}{dx^2} + \frac{\delta x^3}{3!}\frac{d^3f}{dx^3} + \cdots$$

For the Taylor series to be truncated at first order only, the following condition must hold,

$$\left|\frac{\frac{\delta x^2}{2}\frac{d^2f}{dx^2} + \frac{\delta x^3}{3!}\frac{d^3f}{dx^3} + \cdots}{\delta x \frac{df}{dx}}\right| \leq \varepsilon_x \qquad \ldots(14)$$

As a first approximation, it is assumed that δx is very small $\left|\frac{\delta x^3}{3!}\frac{d^3f}{dx^3} + \frac{\delta x^4}{4!}\frac{d^4f}{dx^4} + \cdots\right| \ll \left|\frac{\delta x^2}{2}\frac{d^2f}{dx^2}\right|$. Therefore, equation (14) can be simplified as

$$\left|\frac{\frac{\delta x^2}{2}\frac{d^2f}{dx^2}}{\delta x \frac{df}{dx}}\right| \leq \varepsilon_x$$

Or,

$$\left|\frac{\frac{\delta x}{2}\frac{d^2f}{dx^2}}{\frac{df}{dx}}\right| \leq \varepsilon_x$$

Equation (4) is derived from the Laplace equation, whose solution is a sinusoidal function. Therefore, the function $f(x)$ is taken as a sinusoidal function.

$f(x) = \cos kx$

$$\frac{df}{dx} = -k \sin kx$$

$$\frac{d^2f}{dx^2} = -k^2 \cos kx$$

$$\left|\frac{\frac{\delta x}{2} k \cos kx}{\sin kx}\right| \leq \varepsilon$$

At the characteristic point where $\cos kx = \sin kx$,

$$\frac{\delta x}{2} k \leq \varepsilon_x$$

considering $k = \frac{2\pi}{L}$ and taking the equality sign yields,

$$\delta x = \frac{\varepsilon_x}{\pi} L \qquad \ldots(15)$$

Equation (15) gives a very small grid size. To allow for a larger grid size, the Taylor series expansion is extended up to the fourth order, under the assumption that,

$$\left|\frac{\delta x^5}{5!}\frac{d^5f}{dx^5} + \frac{\delta x^6}{6!}\frac{d^6f}{dx^6} + \cdots\right| \ll \left|\frac{\delta x^2}{2}\frac{d^2f}{dx^2} + \frac{\delta x^3}{3!}\frac{d^3f}{dx^3} + \frac{\delta x^4}{4!}\frac{d^4f}{dx^4}\right|$$

Equation (14) becomes,

$$\left|\frac{\frac{\delta x^2}{2}\frac{d^2f}{dx^2} + \frac{\delta x^3}{3!}\frac{d^3f}{dx^3} + \frac{\delta x^4}{4!}\frac{d^4f}{dx^4}}{\delta x \frac{df}{dx}}\right| \leq \varepsilon_x \qquad \ldots(16)$$

Following similar steps, the equation for δx is obtained as a cubic polynomial,

$$\frac{\delta x}{2}\frac{2\pi}{L} - \frac{\delta x^2}{3!}\left(\frac{2\pi}{L}\right)^2 - \frac{\delta x^3}{4!}\left(\frac{2\pi}{L}\right)^3 - \varepsilon_x = 0 \quad .(17)$$

Table (1) presents the results of the grid size calculations for waves with a wavelength of 16,072 m. It is evident that the grid size obtained from equation (17) is larger than that from equation (15). This indicates that using a longer Taylor series allows for a larger grid size. Since equation (17) is formulated using a fourth-order Taylor series, it provides better accuracy than equation (15).

Table.2: Grid size calculation results

ε_x	δx_{15} (m)	δx_{17} (m)	$\frac{\delta x_{17} - \delta x_{15}}{\delta x_{13}} x100\%$
0.05	0.256	0.265	3.676
0.06	0.307	0.321	4.505
0.07	0.358	0.377	5.373
0.08	0.409	0.435	6.28
0.09	0.46	0.494	7.232
0.1	0.512	0.554	8.232
0.11	0.563	0.615	9.285
0.12	0.614	0.678	10.395
0.13	0.665	0.742	11.571
0.14	0.716	0.808	12.817
0.15	0.767	0.876	14.144

Note : δx_{15}: calculated using equation (15)
δx_{17}: calculated using equation (17)

3.4. Model Results

For example, consider waves with a wave amplitude $A_0 = 1.5\,m$ or $H_0 = 3.0\,m$, a deep water wave constant $k_0 = 0.391$ m^{-1}, $L_0 = 16.072$ m, $T = 9.496$ sec., $\sigma = 0.662$ sec^{-1}, $G_0 = 0.000579$ m.m/sec. For this wave, the deep water depth is $h_0 = 23.358$ m. Diffraction analysis is performed at the breakwater entrance with an entrance width of 40.0 m, approximately 40.0 m≈2.5 L, and a lee side domain of 150 m × 150 m. The water depth is 25 m, which exceeds h_0, classifying the entrance and lee side as deep water;

therefore, no wave transformation analysis from deep water to the entrance is necessary.

Calculations are conducted using a grid size of $\delta x = \delta y = 0.876$ m, obtained based on an accuracy level $\varepsilon_x = 0.15$. The results of the diffraction analysis are presented in Fig. (6).

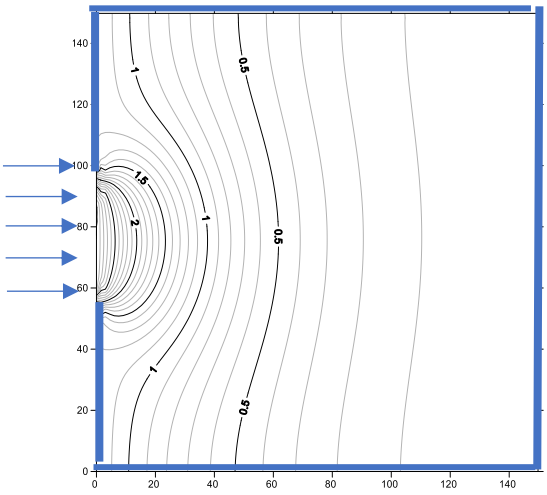

Fig.6: Wave height H contour

In the model results shown in Fig. (6), a very rapid decrease in wave height along the x-axis is observed, starting from an initial wave height $H = 3.0$ m at the entrance, the wave height reduces to 1.0 m at a distance of 30 m. This indicates that the energy transfer in the lateral direction—that is, perpendicular to the wave propagation direction—is excessively large. This behavior contrasts significantly with findings from Penney & Price (1952), Wiegel (1962), and the U.S. Army Coastal Engineering Research Center (1977), where wave height evolution in the wave direction is more gradual.

To align the diffraction results with previous research, equation (4) is modified as follows:

$$\frac{\partial^2 G}{\partial x^2} + \gamma \frac{\partial^2 G}{\partial y^2} 0 \quad \ldots (18)$$

Where γ is a coefficient smaller than 1.0. This coefficient, termed the lateral energy transfer coefficient, quantifies energy transfer in the direction perpendicular to the wave propagation.

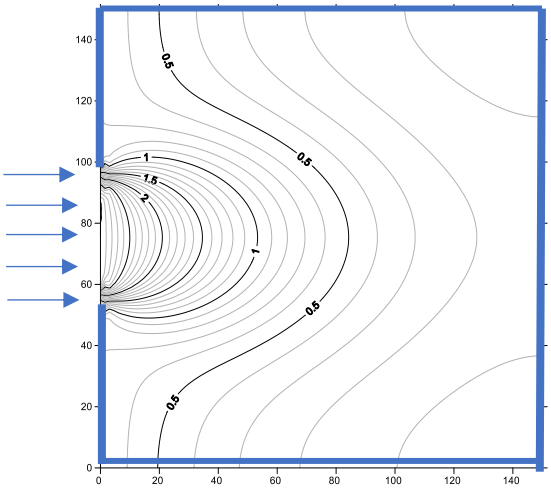

Fig.7: Wave height H contour using $\gamma = 0.25$

Therefore, equation (9) becomes

$$2\left(1 + \gamma \frac{\delta x^2}{\delta y^2}\right) G_{i,j} =$$

$$G_{i+1,j} + G_{i-1,j} + \gamma \frac{\delta x^2}{\delta y^2}\left(G_{i,j+1} + G_{i,j-1}\right) \ldots (19)$$

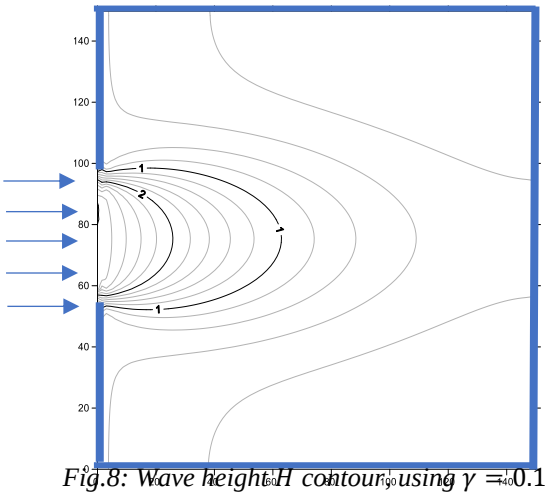

Fig.8: Wave height H contour using $\gamma = 0.125$

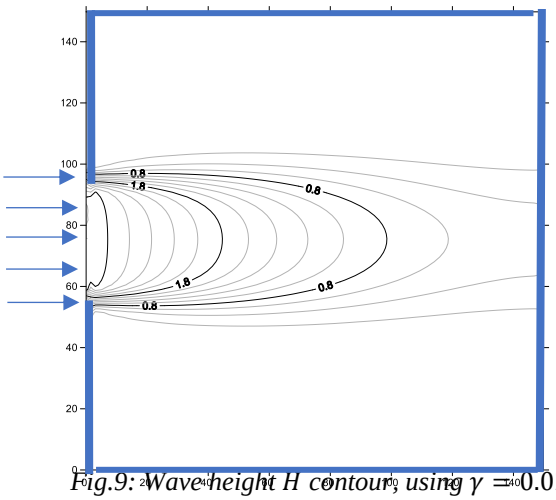

Fig.9: Wave height H contour, using $\gamma = 0.02$

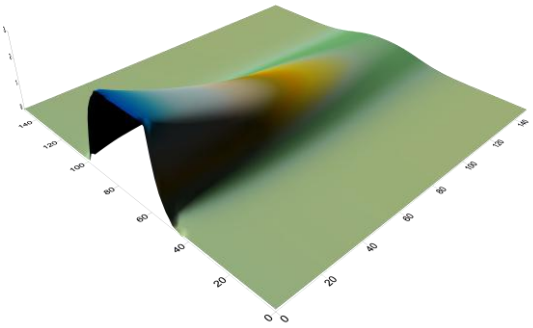

Fig.10: Wave height H contour, 3-D, using $\gamma = 0.02$

Fig. (7) shows the model results for $\gamma = 0.25$, Fig. (8) uses $\gamma = 0.125$, and Fig. (9) uses $\gamma = 0.02$. It is observed that decreasing γ slows the evolution of wave height in the wave direction, indicating a reduction in lateral energy transfer. The calculations using $\gamma = 0.02$ produce results most consistent with previous research findings. The small value of γ thus reflects that lateral energy transfer is minimal.

IV. WAVES FORMING AN ANGLE

In the application of equation (4), the horizontal-x axis must always be aligned with the incoming wave direction. For waves that approach at an angle relative to the breakwater axis, represented by the (ξ, η) coordinate system, the horizontal-x axis will form an angle with the breakwater's horizontal -ξ axis, as shown in Fig. (11). Under these conditions, the grid points generated in the (x, y) coordinate system become non-uniform and irregular.

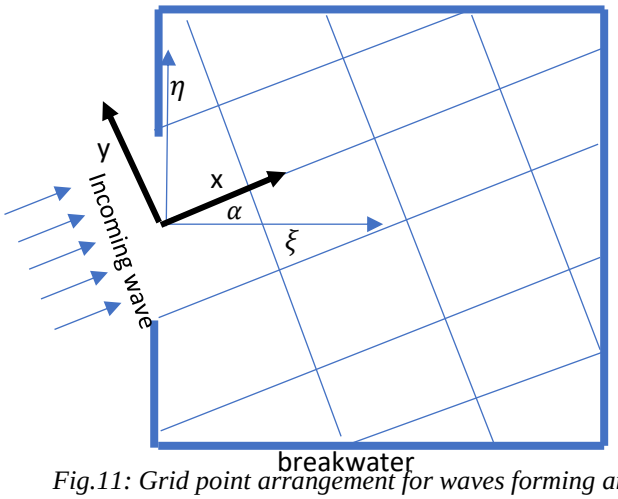

Fig.11: Grid point arrangement for waves forming an angle to the breakwater axis..

In such cases, advanced grid generation methods and numerical techniques that fall outside the scope of the present research are required.

V. CONCLUSION

Overall, the model developed in this research is capable of producing results that align well with previous research findings, indicating that the model can be considered reliable for wave diffraction analysis at breakwater gaps. However, this alignment has been achieved through the adjustment of the lateral energy transfer coefficient. Thus, obtaining reliable values for this coefficient requires further investigation, including laboratory-based physical model studies.

While the governing equation used is relatively simple, involving only a single variable, this simplicity results in an overestimation of lateral energy transfer. If the governing equation were to include the wave number, or the wave number along with the wave direction as variables, it is likely that a more accurate model of lateral energy transfer could be obtained—one that no longer requires an energy transfer coefficient. Consequently, it can be concluded that further research is still needed on the governing equation of the diffraction model.

REFERENCES

[1] Dean, R.G., Dalrymple, R.A. (1991). Water wave mechanics for engineers and scientists. Advance Series on Ocean Engineering.2. Singapore: World Scientific. ISBN 978-981-02-0420-4. OCLC 22907242.

[2] Hutahaean, S. (2023). Water Wave Velocity Potential on Sloping Bottom in Water Wave Transformation Modeling. International Journal of Advance Engineering Research and Science (IJAERS). Vol. 10, Issue 10; Oct, 2023, pp 149-157. Article DOI: https://dx.doi..org/10.22161/ijaers.1010.15.

[3] Hutahaean, S. (2023). New Weighted Taylor Series for Water Wave Energy Loss and Littoral Current Analysis. International Journal of Advance Engineering Research and Science (IJAERS). Vol. 12, Issue 1; Jan, 2025, pp 27-39. Article DOI: https://dx.doi..org/10.22161/ijaers.121.3.

[4] Arden, Bruce W. and Astill Kenneth N. (1970). Numerical Algorithms : Origins and Applcations. Philippines copyright (1970) by Addison-Wesley Publishing Company, Inc.

[5] Penney, W.G., Price, A.T. (1952). The Diffraction Theory of Sea Waves and The Shelter Afforded by Breakwaters. Philos. Trans. Roy. Soc. A, Vol.244 (882), pp. 236-253.

[6] Wiegel, R.L (1962). Diffraction of Waves by a Semi-infinite Breakwater. J. Hydraulics Div., ASCE, Vol.88, No. HYI, pp. 27-44.

[7] U.S. ARMY Coastal Engineering Research Center (1977). Shore Protection Manual, Vol.I, U.S. Government Printing Office, Washington, D.C.

International Journal of Advanced Engineering Research and Science (IJAERS)
Peer-Reviewed Journal
ISSN: 2349-6495(P) | 2456-1908(O)
Vol-12, Issue-5; May, 2025
Journal Home Page Available: https://ijaers.com/
Article DOI: https://dx.doi.org/10.22161/ijaers.125.7

Norms and Associated Health Hazard in Himalayan Water System: A Review

Shagolsem Dungo Meitei[1], Pydikondala Narasimha Satya Abhiram[1], Rohit Singh Sajwan[1]*, Veena Joshi[2]

[1]School of Applied and Life Sciences, Uttaranchal University, Dehradun, Uttarakhand, India
[2]Department of Chemistry, SRT Campus Badshahithaul, Tehri Garhwal, Uttarakhand, India

Received: 26 Apr 2025,
Receive in revised form: 21 May 2025,
Accepted: 27 May 2025,
Available online: 30 May 2025

***Keywords*— Radon, Uranium, WHO, AERB, Physicochemical.**

***Abstract*—** *Water is the most important element in our environment. Radionuclides such as Uranium and Radon are soluble in water and can pose a significant health hazard. This review provides a comprehensive analysis of the source, occurrence, impact on inhabitants and affecting factors in Uttarakhand state. As Uttarakhand is a water-rich region known for its abundant rivers, springs and groundwater, monitoring of radionuclide contamination is very crucial from a public health and environmental point of view. Districts Bageshwar and Pauri show the maximum uranium content, and Tehri and Rudraprayag show the maximum concentration of radon in water. Mainly, Geology is the main factor in Uttarakhand for uranium and radon anomalies. The result depicts that there is no significant health risk in Uttarakhand state. All dose rates from the uranium and radon are less than the recommended limit prescribed by UNSCEAR and WHO.*

I. INTRODUCTION

Radiation is a type of energy that is related to wave or particle movement. In our daily lives, we are constantly exposed to this radiation [1]. Various radiations have different properties: 1) Alpha radiations - the alpha particles are taken into the body by inhalation, ingestion or drinking, and they can produce biological effects on the body. 2) Beta radiation- Beta radiation is more penetrating than alpha particles, and it can penetrate easily into 1-2 cm of water. 3) Gamma rays- They are electromagnetic radiation. Uranium is a chemical element symbolized by U and with an atomic number of 92. Uranium is a silvery-grey metal. Uranium has several isotopes, but the isotope of choice in radioactivity and nuclear technology is Uranium-238. Processing and mining of uranium ore is the reason for the introduction of uranium into drinking water [2]. Consumption of uranium ore is the reason for the radiological effect on the kidney liver, and bone [3]. Uranium contains various isotopes. Some of the most prevalent among them include U-238, U-235 and U-234 [4].

Radiation in drinking water can originate from a number of sources, such as industrial processes, naturally occurring minerals in the crust of the earth, and radioactive material contamination [5]. Radium, uranium, and radon are the most frequently occurring radioactive elements in drinking water. From the uranium decay series, 2% of gamma comes from the uranium group, whereas the remaining 98% comes from the radium group [6]. Uranium's oxidation states vary from II to VI in the combined form. The reported divalent uranium compounds are uranium monofluoride and uranium disulfide. There are trivalent uranium compounds, such as hydrides, nitrides, sesquisulfides, halides and borohydrides [7].

Radon is an intermediate element of the Uranium decay series and is placed in the periodic table with the symbol Rn and atomic number 86. It is a colourless, odourless, noble gas and radioactive. Out of the three naturally occurring isotopes of radon, only radon-222 has a half-life long enough (3.82 days) to emanate out of the rock and soil in which it is generated [8]. The initial by-products of the decay of radium isotopes are radon isotopes. Its most stable

isotope, radon-222, is not stable, so radon is one of the rarest elements. Though it has a short half-life, radon will remain on Earth for a few billion years because it is constantly being generated as a by-product of the decay of the thorium-232 and uranium-238, two extremely common radionuclides with half-lives of a few billion years. Many other short-lived nuclides, known as "radon daughters", are produced during radon decay and naturally yield stable isotopes [9]. Small amounts of radon-220 are generated as an intermediate step in the decay chain of thorium-232, or the thorium series, which ultimately decays into stable lead-208 [10].

Studies have shown that the second largest cause of Lung cancer is radon, and it was discovered that uranium mines with extremely high radon exposure were at high risk of lung cancer. Chinese, North American, and European studies have also shown that even low levels of radon, such as those occurring indoors, can still be harmful to human health and cause lung cancer globally. The possibility of internal radiation exposure is the main reason why drinking water radioactivity exposure might be harmful to one's health. Over time, eating radioactive materials can cause them to build up in the body and irradiate surrounding tissues, raising the risk of cancer. Depending on the kind and amount of radioactive materials present, drinking water radioactivity can have different health impacts. Limits on permissible levels of radioactivity in drinking water are imposed by regulatory bodies in order to safeguard public health. Filtration, ion exchange, and reverse osmosis are examples of water treatment techniques that can be used to lower radioactivity levels in drinking water [11].

Drinking water contains a low concentration of radon, although the radon emitted during water use contributes slightly to the radon concentration indoors [12]. Research revealed that there is little chance of stomach cancer and other gastrointestinal cancers from radon in drinking water. Research on the cytogenetic and genetic consequences of indoor radon has produced conflicting findings; nonetheless, radon exposure in miners causes chromosomal abnormalities and gene mutations. Several in vitro cytogenetic investigations have shown that radon causes a variety of genetic and cytogenetic damage, which may contribute to the development of radon lung cancer [13].

II. MATERIAL AND METHOD

2.1 Radon in Water

2.1.1 RnDuo

In determining radioactive elements in water, the term RnDuo means that the radon and radium pair is important. Because radium (Ra) and radon (Rn) isotopes are able to cause health hazards, the monitoring of water supplies is common. There are several techniques, such as liquid scintillation counting and alpha spectroscopy are utilized to detect and measure these isotopes in water samples. Sustaining public health and ensuring that water quality standards are met requires continual monitoring of such radioactive elements. In order to test radioactive material in an intelligent manner, the most significant steps to utilise smart RnDuo are sample collection, preparation, instrument set-up, analysis, interpretation and reporting. This instrument detects the emitted alpha particles from Rn-222 and Rn-220 based on the principle of scintillation counting with ZnS (Ag). The device can be used for both short as well as long-term measurements. A pump is attached to the device to take air for the liquid sample pump should be left ON for around 5 min before beginning the sampling [14,15]

2.1.2 RAD7

A commonly employed radon detector for measuring indoor radon gas concentrations is the RAD7. RAD7 is the versatile and advanced method for a complete examination of radon in air, water and soil. RAD7 (DURRIDGE, USA) was used in this study. RAD7 utilised a solid-state alpha particle detector with a silicon ion-implanted detector with a solid-state device. The radioisotope's daughters form by characteristic radiation such as alpha, beta, and gamma decay. The alpha radiation Rn-222 and thoron were measured by the RAD7 and converted these alpha radiations into electrical signals. The instrument is most suitable for field applications, and it is supplied with a covered, robust carrying case for use in the field. The sample cell of 0.7 litre hemispherical volume in the RAD7. The hemisphere is lined on the inside thereof with an electrical conductor. The inside conductor is charged up to a potential of 2000-2500 V by the high voltage power circuit and makes the positively charged particles come to the detector. Rn-222 decays to the polonium-218 as the positively charged ion, and this short-lived polonium-218, after decay, on the active side of the detector, has a 50% probability of entering the detector and producing an electrical signal of a strength proportioned to the energy of the alpha particle. The signal in the detector is not uniform in strength since different isotopes do not give the same energy. The signal is amplified, filtered and arranged in strength by the instrument. The spectrum of this instrument can allow energies ranging from 0-10 MeV, as most of the decay products of radon and thoron produced alpha particles in the range of 6-9 MeV. The RAD7 operate in the following mode [16]

2.1.3 Uranium in Water

The presence of uranium in water, particularly in excess, may be a causative factor of health harm to human beings. Groundwater is contaminated by naturally occurring uranium in soil and rock [17]. Water contamination by uranium is also brought about by industrial processes like uranium mining and ore treatment. Because uranium is made up of radioactive components, exposure through the ingestion of consumed drinking water is capable of leading to health harm. Damage to the kidney, an increase in the risk of cancer development, and other health complications are linked to long-term uranium ingestion. The risk the radiation poses to the health of individuals is based on the amount of uranium in the water people are exposed to and the duration of exposure [18]. Because of the possible health hazard, uranium in water can be cancerous. Naturally or through man's actions like mining, uranium can find its way into water bodies. Ingestion of contaminated water with high uranium levels will result in some health complications like damage to the kidney as well as a high rate of chances of developing cancer [19].

2.1.4 Inductively Coupled Plasma Mass Spectrometry

Nowadays, one of the most quickly evolving tracer element techniques is inductively coupled plasma mass spectrometry (ICP-MS) [20]. Inductively Coupled Plasma Mass Spectrometry, or ICP-MS is a very effective analytical technique that unites the merits of mass spectrometry and plasma spectroscopy to detect and quantify trace elements and isotopes in different samples. The technique is founded on the introduction of a sample into an ICP torch, which atomizes, ionizes, and transforms it into a plasma state. The ions produced in the plasma are drawn and separated in the mass spectrometer according to their mass-to-charge ratio. Its advantages are low detection limits, high analysis speed, and the ability to analyze multiple isotopes. Scientists are employing ICP-MS for the analysis of U-238 in seawater increasingly since ICP-MS equipment became available [21].

2.1.5 Atomic Absorption Spectroscopy

Atomic Absorption Spectroscopy, abbreviated as AAS, is another intriguing technique for analyzing the elements present in a sample [22]. It quantifies the light absorbed by elements present in a sample by the transmission of light through it. The absorbed light quantifies the varying concentration levels of elements present in the sample. AAS is commonly applied in a laboratory to quantify metals in various materials, such as biological samples, environmental samples, and even food and drinks [23]. Because of its specificity and sensitivity, AAS (Atomic Absorption Spectroscopy) is one technique of uranium detection in water [24].

2.1.6 Assessment of Effective Dose

A useful method of estimating possible radiation exposure risk is effective dose assessment. In addition to the parts of the body that are exposed, it considers the nature of the radiation and the sensitivity of each body part to radiation. An effective dose is quantified in terms of a measurement called a sievert (Sv). For the protection of human beings from harmful doses of radiation, it is used to quantify the risk of health effects resulting from radiation exposure and in the establishment of safety standards [25].

The International Commission on Radiological Protection (ICRP) developed the effective dose as a risk-based hazard to human beings. It is the quantification of the radiation hazards of whole-body exposure to a non-uniform dose of radiation. The effective dose in radiation protection is a quantification that considers the varying radiation sensitivity levels of the body's tissues and organs [26]. Tissue weighting factors and radiation weighting factors are used in its calculation. The International Commission on Radiological Protection (ICRP) has established guidelines for the calculation of the effective dose. The dose absorbed in an organ or tissue times the radiation weighting factor is referred to as the organ equivalent dose. The ICRP offers the most common radiation and tissue weighting parameters in its publication, ICRP 103. These elements are required for accurately determining the effective dose.

III. RESULT AND DISCUSSION

2.2 Uranium and Radon in water

Table 1: Uranium and Radon concentrations in districts of Uttarakhand.

SN	Location	Uranium (ppb)			Radon (Bq/L)			Reference
		Min	Max	AM	Min	Max	AM	
1	Tehri	0.001	7.41	0.89	29.0	192.0	70	[27]
2	Dehradun	0.02	4.97	0.97	3.35	99.25	33.97	[28,29]
3	Almora	0.1	23.1	4.3				[30]
4	Pithoragarh	0.10	1.12	0.37	0.60	81.90	17.80	[31,15]
5	Nainital	0.10	27.40	4.40				[30]
6	Chamoli				2	47	11	[32]
7	Champawat	0.09	9.01	4.55				[31]
8	Bageshwar	0.10	28.40	14.25	3.40	101.30	34.80	[33]
9	Haridwar	0.35	27.53	7.14	0.36	2.64	1.5	[28,34]
10	Uttarkashi	0.01	21.57	2.86	1.11	183.86	19.67	[27,35]
11	Rudraprayag	0.001	6.03	0.71	1.7	400	67	[27,32]
12	Pauri Garhwal	0.01	67.45	5.78	0.43	0.73	0.68	[36]
13	Udham Singh Nagar	0.01	26.98	3.43				[37]

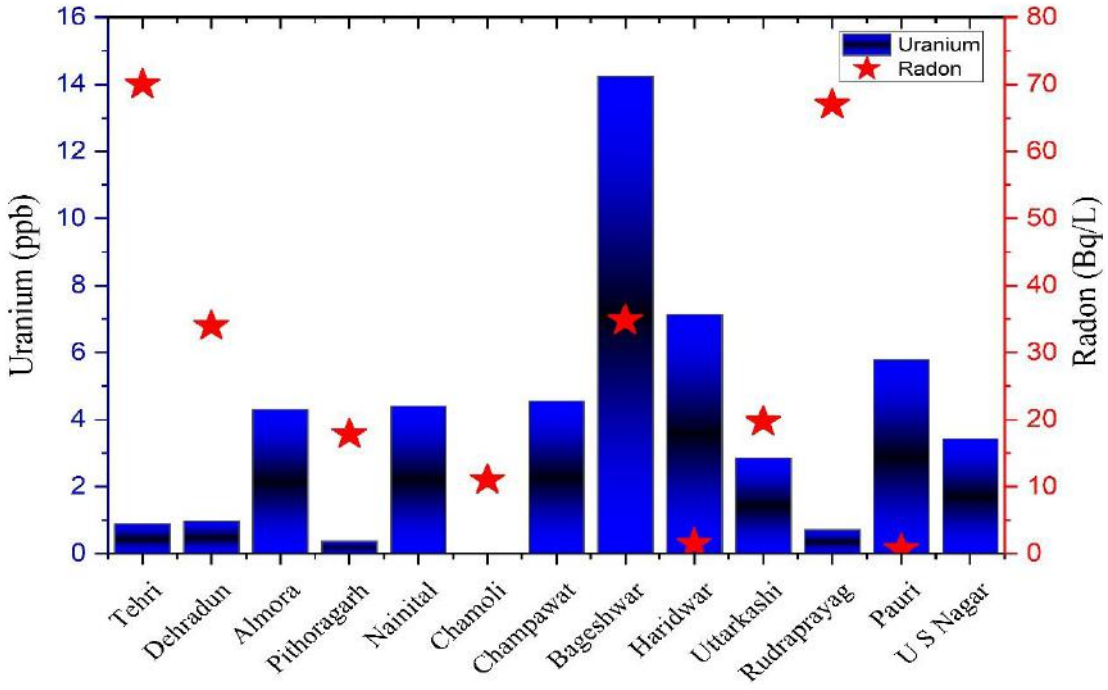

Fig 1. (A) Spatial Distribution of Uranium (B) Uranium and Radon levels in districts of Uttarakhand

The Uttarakhand state is rich in water resources. Table 1. depicts that the uranium concentration is evaluated from the water samples of all the districts of Uttarakhand. Pauri Garhwal, Haridwar, Bageshwar, and Nainital have relatively high average uranium levels. These regions are known to contain granitic rocks, metamorphic formations, and uranium-bearing minerals. When groundwater percolates through these rocks, uranium leaches into the

water. Uranium content in the water system in Uttarakhand varies from 0.37 ppb (Pithoragarh) to 14.25 ppb (Bageshwar), whereas radon values range from 0.68 Bq/L (Pauri) to 70.00 Bq/L (Tehri). Their elevation in that area is due to groundwater flowing through mineral-rich rocks, which raises uranium concentrations. The high uranium level in Bageshwar (up to 28.4 ppb, AM = 14.25 ppb) may be due to the area's underlying granitic and metamorphic rocks, which naturally contain higher uranium content. Weathering and leaching processes likely mobilize uranium into groundwater [33] noted such geogenic factors in their hydrogeochemical assessment of the region. Additionally, as uranium decays, radon gas is produced and can build up in buildings. Water in these areas might have an alkaline pH and oxidizing conditions, which enhance uranium solubility, leading to elevated concentrations. Districts like Dehradun**,** Tehri**,** Pithoragarh**,** and Rudraprayag show low uranium averages (<1 ppb)**.** These areas may be dominated by sedimentary deposits, which contain less uranium than igneous or metamorphic rocks. High rainfall and surface water influence in areas like Tehri and Dehradun can dilute uranium concentrations. Groundwater in these regions might flow through less mineralized zones, meaning fewer uranium sources are present in the aquifer. The Uranium content in all districts is well below the recommended level of 30 ppb and 60 ppb recommended by WHO and AERB, respectively.

Table 1 also presents radon concentration data (in Bq/L) in groundwater samples from various districts of Uttarakhand. The values show significant variability across the region, influenced by geological and environmental factors. Among the districts with reported radon data, Tehri stands out with the highest maximum value of 192.0 Bq/L and an average concentration of 70 Bq/L, followed closely by Rudrapryag (Max: 400 Bq/L, Avg: 67 Bq/L), These elevated levels are primarily due to the presence of uranium-rich rocks and geothermal activity common in Himalayan terrains, where radon gas accumulates in deep aquifers. In contrast, some regions like Haridwar report very low radon values (AM 1.5 Bq/L), as do Pauri Garhwal (Max: 0.73 Bq/L, Avg: 0.68 Bq/L). These areas lie in the foothills and plains, dominated by sedimentary formations and alluvial soils, which naturally contain less uranium and allow radon to escape more easily before entering water supplies. Additionally, water sources in these areas are typically shallower, reducing the contact time with radon-emitting rocks.

Comparing these values to the World Health Organization (WHO) guideline of 100 Bq/L, only Tehri and Bageshwar have reported maximum radon levels that exceed this limit. However, when compared to the much stricter USEPA proposed limit of 11 Bq/L, several districts, including Tehri, Bageshwar, Pithoragarh, and Uttarkashi, exceed safe levels, especially in terms of average concentration.

2.3 Water Quality Parameters

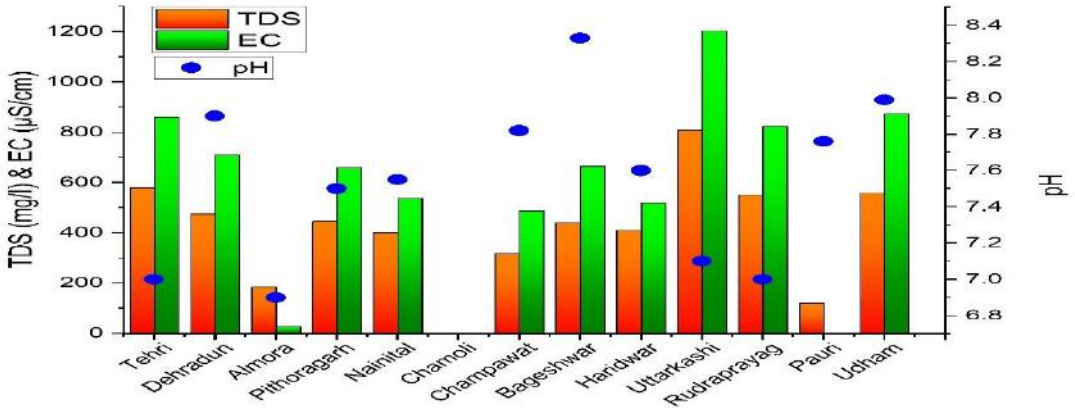

Fig 2. pH, TDS, EC level in Uttarakhand.

Table 2: Water Quality parameters in districts of Uttarakhand.

SN	District	pH	TDS (mg/l)	EC (µS/cm)	Reference
1	**Tehri**	7.0	578.1	859.0	[27]
2	**Dehradun**	7.9	475.24	709.24	[38]
3	**Almora**	6.9	183	26	[30]
4	**Pithoragarh**	7.5	444	657.6	[39]
5	**Nainital**	7.55	400	536.00	[40]
6	**Chamoli**				
7	**Champawat**	7.5	317.5	486	[31]
8	**Bageshwar**	8.33	438	663	[41]
9	**Haridwar**	7.6	408.3	518	[34]
10	**Uttarkashi**	7.1	807.2	1201.1	[27]
11	**Rudraprayag**	7.0	550.9	822.2	[27]
12	**Pauri Garhwal**	7.76	119		[42]
13	**Udham Singh Nagar**	7.99	558.4	872.5	[15]

Table 2 provides a comparative analysis of groundwater quality across various districts of Uttarakhand, focusing on physicochemical parameters like pH**,** Total Dissolved Solids (TDS), and Electrical Conductivity (EC) with the permissible limits of WHO. The pH levels in the districts vary from 6.9 to 8.33, which is predominantly in the WHO guideline range of 6.5 to 8.5 for potable water. The districts of Bageshwar, Dehradun, and Udham Singh Nagar have a pH that is slightly above 7 and hence are more susceptible to mobilization by uranium. This is due to the fact that uranium prefers to precipitate as soluble carbonate complexes in basic conditions, hence promoting an increased concentration of uranium in the water. However, some areas, such as Almora (with an average pH of 6.9) have slightly acidic water, which tends to favour radon solubility. As a gas, radon is easily dissolved in slightly acidic water, particularly where there are high granite contents that are prevalent in such regions.

The TDS values in the districts vary widely, with values ranging from 119 mg/L (in Pauri) to a striking 807.2 mg/L (in Uttarkashi). WHO suggests a desirable limit of 500 mg/L, with an upper permissible limit of 1000 mg/L. Districts like Tehri, Udham Singh Nagar, and Uttarkashi have higher TDS, indicating mineral-rich groundwater. Such high mineralization suggests that geochemical weathering is likely occurring in the area, which may lead to increased uranium mobilization from rocks into the groundwater. In regions with higher TDS, uranium can become more soluble, posing potential health risks. On the other hand, Almora, with a low TDS (183 mg/L), and Pauri Garhwal (with 119 mg/L), have low mineral content, meaning the groundwater has lower ionic strength. However, low TDS doesn't rule out the possibility of radon presence, especially if the geology is favourable (such as granite formations, which are common in Almora).

EC is a good indicator of the water's ionic content. WHO does not set a strict EC limit, but values above 750 µS/cm are considered high. The average EC ranges from 26 µS/cm in Almora to 1201.1 µS/cm in Uttarkashi. High EC values like those in Uttarkashi and Udham Singh Nagar suggest high mineralization of water, which might be related to geothermal activity or metamorphic rock interactions, which can increase the likelihood of uranium contamination. The high EC reflects the presence of dissolved salts and ions, which can carry uranium and other trace elements. Low EC values, as seen in Almora and Pauri Garhwal, suggest low ionic content and generally indicate a lower concentration of dissolved minerals. However, this does not completely eliminate the possibility of radon contamination, as radon can still be found in areas with low mineralization, particularly if the geology is conducive to radon release (e.g., granite).

2.4 Chemical Parameters in Water

Table 3: Statistical analysis of chemical parameters.

SN	Location	F^-	Cl^-	NO_3^-	SO_4^{2-}	PO_4^{3-}	Ca^{2+}	Mg^{2+}	K^+	Na^+	Reference
1	**Tehri**		19.65	0.72	28.2	0.58	39.5	26.95	13.95	9.25	[43]
2	**Dehradun**	1.58	10.07	3.46	132.77	1.03	85.22	37.01	1.71	10.24	[38]
3	**Almora**										
4	**Pithoragarh**	0.2	97.7	4.8	11.3	0.4	20.1	60.2	15.77	14.49	[39,44]
5	**Nainital**	0.06	5.2	4.6	39	0.12	57	21	1.8	6.6	[45]
6	**Chamoli**										
7	**Champawat**	0.19	113.44	21.05	13	1.30	27.57	25.06			[31]
8	**Bageshwar**	0.56	22.01	2.62	32.71		31	31.75	2.5	8	[41,46]
9	**Haridwar**	0.15	29.34	12.15	36.22		59.23	30.65	5.38	39.21	[35]
10	**Uttarkashi**						27.57	25.06			[30]
11	**Rudraprayag**		4.48	0.6	0.31	0.53	17.8	8.85			[47]
12	**Pauri Garhwal**	0.40	15	1.4	6		18	7.30	1.17	3.22	[42]
13	**Udham Singh Nagar**	0.79	81.05	4.26	48.4		66	46	6.5	58.35	[48]
14	**Permissible limits**	1.5	250	45	200	1	75	30	25	200	[49,50]

The table presents the concentration ranges of fluoride (F^-), chloride (Cl^-), nitrate (NO_3^-), sulphate (SO_4^{2-}), and phosphate (PO_4^{3-}) across various districts of Uttarakhand, and when analyzed against recommended values from WHO and BIS, it highlights potential geochemical environments that could influence the behaviour of uranium and radon in groundwater. For instance, the BIS permissible limit for fluoride is 1.5 mg/L, but Dehradun shows concentrations as high as 1.58 mg/L, and other regions also exceed safe levels—suggesting strong fluoride-bearing mineral interactions, which can also mobilize uranium through the formation of soluble UO_2F^+ complexes. Nitrate concentrations, which can accelerate the oxidation of U(IV) to the more soluble U(VI) form, are notably high in Champawat (up to 21.05 mg/L), pointing to both anthropogenic input and an environment conducive to uranium migration. Sulfate and phosphate also affect uranium mobility: extremely high sulfate values may contribute to complexation, while phosphate levels—like the 39 mg/L in Nainital—may lead to precipitation of low-solubility uranium-phosphate minerals. These areas also lie within or near regions of high uranium-bearing bedrock, like granites and metamorphic, which are sources of radon gas. Since radon is a decay product of uranium, its concentration in groundwater and indoor air is strongly influenced by uranium content and the permeability of the host rocks. Thus, districts such as Nainital, Dehradun, Pithoragarh, and Haridwar not only exhibit chemical signatures favourable for uranium mobility but are also geologically predisposed to elevated radon risk, warranting detailed hydrogeochemical and radiological assessments to ensure safe water quality and public health protection.

The presence of calcium is higher than the recommended values in Dehradun. The maximum value of calcium in water samples of different localities of Uttarakhand state ranges from 17.8-85.22 mg/l and the permissible limit is 75 mg/l. The values of magnesium ion are higher in some places like Dehradun (37.01mg/l), Pithoragarh (60.2mg/l), and Udham Singh Nagar (46mg/l) than the safety guidelines is 30mg/l in all the investigated areas of Uttarakhand except Rudraprayag (0.53mg/l), the values of magnesium ion in Rudraprayag are under the permissible limit.

The presence of potassium in the water samples of different districts of Uttarakhand varies from district to district. The value of potassium ions ranges from 1.17 - 15.77 a with a permissible limit of 25 mg/l. The value of Sodium metal ranges from 3.22-58.35 mg/l in the water samples of different districts of Uttarakhand that are under the permissible limits (200).

2.5 Associated Health risk in Uttarakhand by radioactive elements

According to the World Health Organization, the recommended annual effective dose for radon exposure should not exceed 1 mSv (1000 µSv/year), while the United Nations Scientific Committee on the Effects of Atomic

Radiation suggests that ingestion of uranium should remain below 100 µSv/y. Among the surveyed regions, Bageshwar and Haridwar are getting the highest value. In Bageshwar, the Excess Cancer Risk (ECR) value varied between 3×10^{-8} and 894 $\times 10^{-8}$ with a mean value of 50.0 $\pm 21 \times 10^{-8}$. The computed values of ECR were well within the safe limit for radiological risk. The concentration of uranium in drinking water was less than the reference limit suggested by USEPA and WHO but in 20% of samples the concentration of uranium was greater than the limits suggested by ICRP [33]. Also, in the Haridwar district the Hazard Quotient was observed with the value of 0.093 and the lifetime average daily dose was found 0.056 µg/kg/d which is less than the reference dose of 0.6 µg/kg/d and 4.4 µg/kg/d prescribed by WHO, 2004 and AERB, 2004. The observed annual effective dose by radon inhalation in Rudraprayag district was a mean value of 100 µSv/y, which is less than the recommended reference limit of 1 mSv/year prescribed by UNSCEAR and WHO.

IV. CONCLUSION

Water is a very important element of life and radioactive contaminated water can pose significant health hazards to inhabitants. The present result shows that Bageshwar and Haridwar show high levels of Uranium content that are largely below the recommended levels set by several regulatory bodies, including the USEPA, WHO, and AERB. Likewise, the use of groundwater as drinking water in many parts of Uttarakhand contributes to the slightly elevated radon consumption in drinking water samples in some areas, which is over the recommended levels. To protect against the health risks that radon poses, it is critical to look into the presence of radon in groundwater. Moreover, the majority of these sources with elevated radon and uranium concentrations come from groundwater sources. The concentration of uranium also varies with the water quality parameters found in the Uttarakhand areas under investigation. This is because uranium tends to be more soluble in areas with low pH levels, while high pH levels in water samples cause uranium to form insoluble precipitates like uranium hydroxides. The geology of Uttarakhand is varied, with some regions naturally having significant uranium and radon concentrations. In some areas, this may be a contributing factor to increased natural radioactivity. In Uttarakhand, water from public supply sources is generally treated and closely monitored to guarantee that it satisfies safety standards, especially those pertaining to radiological safety. Nonetheless, it is advised to have water tested frequently in regions with high levels of naturally occurring radioactivity or where private wells are utilized. Thus, in the future, a thorough investigation from the perspective of health risks will be needed to lower the dose of radon and uranium in water so that residents of these places do not become increasingly exposed to health risks.

REFERENCES

[1] Zamanian A. Hardiman C J H F E. Electromagnetic radiation and human health: A review of sources and effects. *High Frequency Electronics*. (2005). *4*(3); 16-26.

[2] Abdelouas. A. Lutze. W. Nuttall. H E. Uranium contamination in the subsurface: characterization and remediation. Reviews in Mineralogy. (1999). 38; 433-474.

[3] Keith. L. S. Faroon. O. M. Uranium. In Handbook on the Toxicology of Metals. (2022). (pp. 885-936). Academic Press.

[4] Cheng. H. Edwards. R L. Hoff. J. Gallup. C. D. Richards. D A. Asmerom. Y. The half-lives of uranium-234 and thorium-230. Chemical Geology. (2000); 169(1-2); 17-33.

[5] Rajkhowa. S. Sarma. J. Das. A R. Radiological contaminant in water: pollution, health risk, and treatment. In Contamination of water. (2021). (pp. 217-236). Academic Press.

[6] Molinari. J. Snodgrass. W J. The chemistry and radiochemistry of radium and the other elements of the uranium and thorium natural decay series. The environmental behaviour of radium. (1990). 1; 11-56.

[7] Ephritikhine. M. Recent advances in organoactinide chemistry as exemplified by cyclopentadienyl compounds. (2013). Organometallics. 32(9); 2464-2488.

[8] Jabarivasal. N. Indoor atmospheric radon in Hamadan, Iran. Atmospheric radon indoors and around Hamadan city in Iran (Doctoral dissertation, University of Bradford). (2012).

[9] Wilkening. M. Radon in the Environment (Vol. 40). Elsevier. (1990).

[10] István. C. Radon and Space Radiation Protection Measurements (Doctoral dissertation, Debreceni Egyetem (Hungary). Deoli. B K. Bartarya, S. K. Siddiqui. N A. Assessment of surface and ground water Quality of Haridwar district of Uttarakhand. *Int. J. Chem. Tech. Res*. (1997;2017). *10*(10): 95-118.

[11] Khedr. M. G. Radioactive contamination of groundwater, special aspects and advantages of removal by reverse osmosis and nanofiltration. (2013). Desalination, 321, 47-54.

[12] National Research Council, Commission on Life Sciences, Board on Radiation Effects Research, & Committee on Risk Assessment of Exposure to Radon

in Drinking Water. (1999). Risk assessment of radon in drinking water.

[13] Riudavets. M. Garcia de Herreros. M. Besse. B. Mezquita, L.. Radon and lung cancer: current trends and future perspectives. (2022). Cancers, 14(13); 3142.

[14] Kumar. A. Kaur. M. Mehra.R. Sharma. D K. Mishra. R. Comparative study of radon concentration with two techniques and elemental analysis in drinking water samples of the Jammu district, Jammu and Kashmir, India. (2017). Health Physics, 113(4), 271-281.

[15] Singh. P. Nautiyal. O P. Joshi. M. Kumar. A. Ahamad. T. Singh. K. Assessment of physicochemical and radon-attributable radiological parameters of drinking water samples of Pithoragarh district, Uttarakhand. *Journal of Radioanalytical and Nuclear Chemistry*. (2021). *330*, 1559-1570.

[16] Durridge. Electronic Radon Detector. 37, 95. https://www.durridge.com/documentation/RAD7 Manual.pdf .(2018).

[17] Waseem. A.Ullah. H. Rauf. M. K. Ahmad. I. Distribution of natural uranium in surface and groundwater resources: a review. Critical reviews in environmental science and technology. (2015).45(22), 2391-2423.

[18] Patocka. J. Human health and environmental uranium. Military Medical Science Letters. (2014). 83, 120-131.

[19] Vellingiri. B.A deeper understanding about the role of uranium toxicity in neurodegeneration. Environmental Research. (2023). 233, 116430.

[20] Van Acker.T. Theiner. S. Bolea-Fernandez. E. Vanhaecke. F. Koellensperger. G.Inductively coupled plasma mass spectrometry. Nature Reviews Methods Primers. (2023). 3(1); 52.

[21] Diez-Fernandez. S. Jaegler. H. Bresson. C. Chartier. F. Evrard. O. Hubert. A. Isnard. H. A new method for determining 236U/238U isotope ratios in environmental samples by means OF ICP-μS/CMS. (2020). Talanta; 206;120221.

[22] Garcia. R. Baez. A P. Atomic absorption spectrometry (AAS). Atomic absorption spectroscopy. (2012).1; 1-13.

[23] Taylor. A. Day. M. P. Hill. S. Marshall. J. Patriarca. M. White.M. Atomic spectrometry update: Review of advances in the analysis of clinical and biological materials, foods and beverages. Journal of Analytical Atomic Spectrometry. (2014). 29(3); 386-426.

[24] Santos. J S. Teixeira. L. S. Dos Santos. W. N. Lemos. V. A. Godoy. J. M. Ferreira.S L.Uranium determination using atomic spectrometric techniques: an overview. Analytica chimica acta. (2010). 674(2); 143-156.

[25] Part. N. G. Radiation protection and safety of radiation sources International Basic Safety Standards. Interim Edition. (2011).

[26] Martin. C. J. Effective dose: how should it be applied to medical exposures? The British journal of radiology. (2007). 80(956); 639-647.

[27] Panwar. P. Joshi. A. Singh. K. P. Prasad. M. Mehra. R. Sahoo. S. K. Ramola. R. C. Distribution of uranium and selected toxic heavy metals in drinking water of Garhwal Himalaya, India. *Journal of Radioanalytical and Nuclear Chemistry*. (2024). *333*(6); 2927-2935.

[28] Rohit. M. Anamika. K. M. Praveen. M. A comparative study of uranium concentration using two different analytical techniques and assessment of physicochemical parameters in groundwater. *Journal of Radiation and Nuclear Applications*. (2018). *3*(3); 149.

[29] Saklani. C.P. Singh. P. Kumar. A. *et al.* Delineating the radiological dosimetry arising from radon exposure in potable water sources of Dehradun, India. *J Radioanal Nucl Chem* **333**, 3259–3268 (2024). https://doi.org/10.1007/s10967-023-09343-z

[30] Prasad, M, Semwal. P. Panwar. P. Gusain. G. S. Ramola. R. C. Uranium contamination in drinking water as a health concern in Uttarakhand, India. Journal of Radioanalytical and Nuclear Chemistry. (2022). 331(4);1933-1940.

[31] Patni. K. Pratap Pande. A. Pande. C. Physicochemical investigation of some primitive water sources in District Champawat for potability and preservation of historical aesthetics, Uttarakhand, India. *The holistic approach to environment*. (2022). *12*(1); 1-8.

[32] Prasad. M. Kumar.G.A. Sahoo B.K. *et al.* A comprehensive study of radon levels and associated radiation doses in Himalayan groundwater. *Acta Geophys.* **66**; 1223–1231. (2018). https://doi.org/10.1007/s11600-018-0135-0

[33] Kumar. A. Arora. T. Singh. P. Singh. K. Singh. D. Pathak. P. P. Ramola R C. Quantification of radiological dose and chemical toxicity due to radon and uranium in drinking water in Bageshwar region of Indian Himalaya. *Groundwater for Sustainable Development*. (2021). *12*; 100491.

[34] Garg. P. K. Krishan. G O P A L. Kumar. S U D H I R. (2015). Radon concentration in groundwater of Haridwar, Uttarakhand, India. *J Earth Sci Eng*. (2015). *8*(2); 1-4.

[35] Singh. K. P. Chandra. S. Prasad. M. Joshi. A. Prasad. G. Ramola. R C. Estimation of radiation dose due to ingestion of radon in water samples of Garhwal Himalaya, India. *Journal of Radioanalytical and Nuclear Chemistry*. (2024). *333*(6);2867-2879.

[36] Yadav. M. Singh. K. P. Dutt. S. Mehta. V. Kaur. J. Ramola. R C. Risk assessment due to ingestion of uranium and radon in the drinking water samples of the Budhakedar region in Garhwal Himalaya, India. *Journal of Radioanalytical and Nuclear Chemistry*. (2024). *333*(6); 3065-3074.

[37] Negi. R. S. Negi. J. S. Prasad. M. Singh. J. Wadhwa. M. Shrivastava. U. Ramola. R C. Study of radiation exposure to radon in groundwater using scintillation-based RnDuo technique: A statistical analysis for risk assessment. Applied Radiation and Isotopes. (2025).220;111789.

[38] Tripathi. D. K. Pandey. G. Jain. C. K. Physicochemical analysis of selected springs water samples of Dehradun City, Uttarakhand, India. Int J for Innov Res Sci Tech. (2015). 2(5); 99-103.

[39] Patni. K. Pande. C. Pande. A. P. Tiwari. G. Joshi. T. Seasonal variation of uranium and physico-chemical parameters in spring water sources of Pithoragarh city, Uttarakhand, India. Journal of Radioanalytical and Nuclear Chemistry. (2021). 329(2); 647-660.

[40] Sharma. M.Water quality assessment of the central Himalayan Lake, Nainital. *Advances in Environmental Chemistry*, (*2014)*(1); 473074.

[41] Seth. R. Mohan. M. Singh. P. Singh. R. Gupta. V. K. Dobhal. R. Gupta. S. Assessment of seasonal variations in surface water quality of Bageshwar District, Uttarakhand, India for drinking and irrigation purposes. Proceedings of the National Academy of Sciences, India Section A: Physical Sciences. (2015) 85;283-293.

[42] Tyagi. S. Singh. P. Sharma. B. Singh. R. Assessment of water quality for drinking purpose in district Pauri of Uttarakhand, India. *Applied Ecology and Environmental Sciences*. (2014). *2*(4); 94-99.

[43] Agarwal. A. K. Rajwar. G. S. Physico-chemical and microbiological study of Tehri dam reservoir, Garhwal Himalaya, India. Journal of American science. (2010). 6(6); 65-71.

[44] Thakur. P. K. Kumar. V. Deoli. V. Assessment of spring water quality using water quality indices and multivariate statistical techniques in Pithoragarh, Uttarakhand. Journal of The Institution of Engineers (India): Series A. (2023). 104(2); 301-316.

[45] Saini. R. K. Swain. S. Patra. A. Khanday. G. J. Gupta. H. Purushothaman. P. Chakrapani. G J. Water chemistry of three Himalayan Lakes: Dal (Jammu& Kashmir), Khajjiar (Himachal Pradesh) and Nainital (Uttarakhand). Ann. rainfall (mm). (2008). 655(2648); 2300.

[46] Azam. M. Prasad. J. Prasad. H S. Water quality assessment of bageshwar block springs using weighted arithmetic water quality index (WAWQI) method, Bageshwar District, Uttarakhand, India. (2022).

[47] Bisht. S. Sharma. R C. Rawat. S. Kumar. R. Physico–chemical attributes and bacterial diversity of river water at Rudraprayag, Garhwal Himalaya. MOJ Ecology & Environmental Sciences. (2018). 3(4); 277- 282.

[48] Singh. S. Gautam. P. K. Sarkar. T. Taloor. A K. Characterization of the groundwater quality in Udham Singh Nagar of Kumaun Himalaya, Uttarakhand. *Environmental Earth Sciences*. (2022). *81*(19); 468.

[49] BIS. Bureau of Indian Standards. Specification for drinking water. Indian Standards Institution, New Delhi. IS 10500, 1-11. (2012) Website: www.bis.org.in.

[50] WHO. Guidelines for drinking-water quality, vol. 1, 3rd edn. World Health Organization, Geneva. (2004).

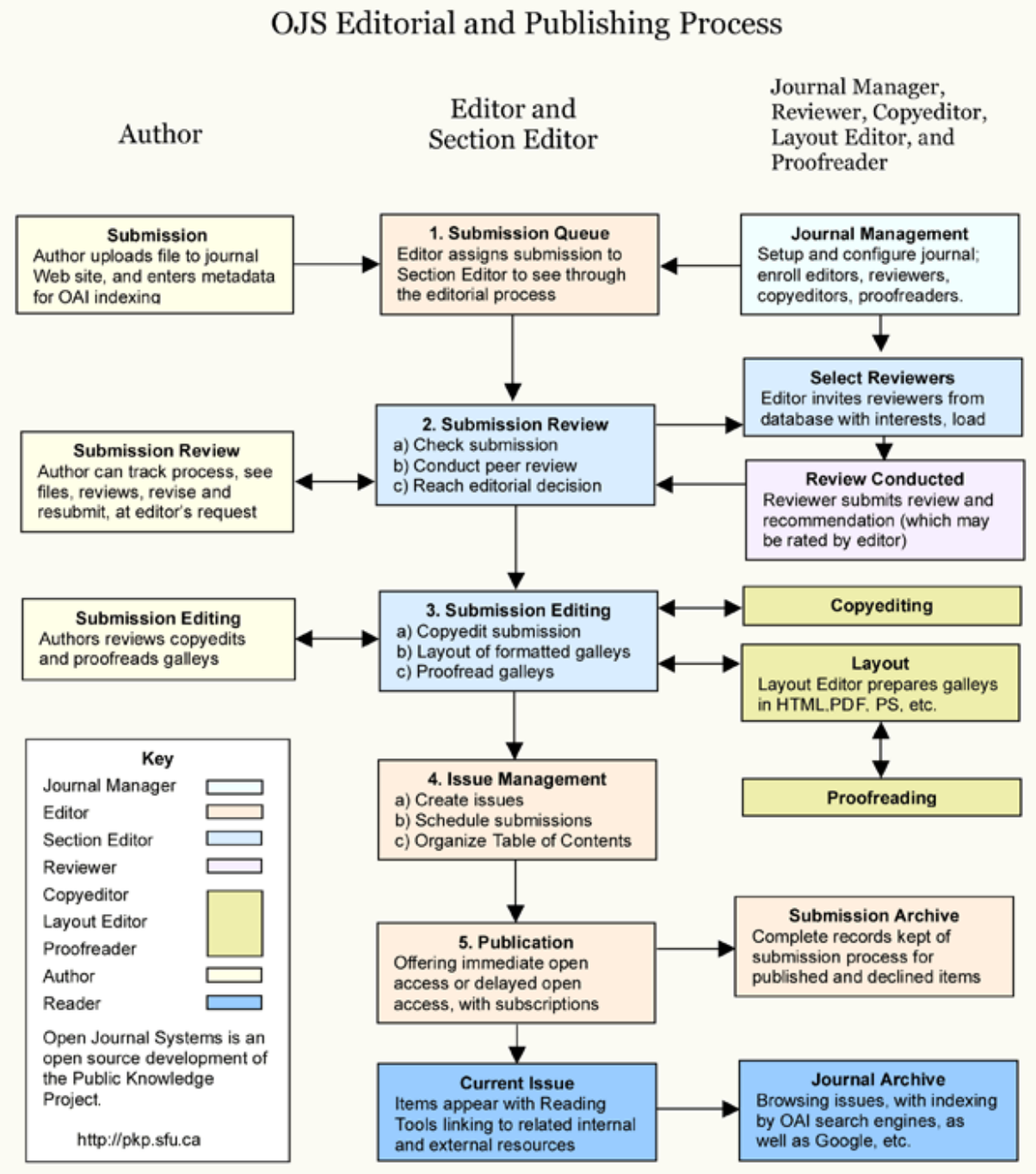

~IJAERS Workflow~

Important links:

Paper Submission Link:
https://ijaers.com/submit-paper/
Editorial Team:
https://ijaers.com/editorial-board/
Peer Review Process:
https://ijaers.com/peer-review-process/
Publication Ethics:
https://ijaers.com/publication-ethics-and-publication-malpractice-statement/
Author Guidelines:
https://ijaers.com/instruction-to-author/
Reviewer Guidelines:
https://ijaers.com/review-guidelines/

Journal Indexed and Abstracted in:

- Qualis-CAPES (A2)-Brazil
- Normatiza (Under Review-Ref.020191511)
- NAAS Score: 3.18
- Bielefeld Academic Search Engine(BASE)
- Aalborg University Library (Denmark)
- WorldCat: The World's Largest Library Catalog
- Semantic Scholar
- J-Gate
- Open J-Gate
- CORE-The world’s largest collection of open access research papers
- JURN
- Microsoft Academic Search
- Google Scholar
- Kopernio - powered by Web of Science
- Pol-Index
- PBN(Polish Scholarly Bibliography) Nauka Polaska
- Scilit, MDPI AG (Basel, Switzerland)
- Tyndale University College & Seminary
- Indiana Library WorldCat
- CrossRef DOI-10.22161/ijaers
- Neliti - Indonesia's Research Repository
- Journal TOC
- WIKI-CFP
- Scinapse- Academic Search Engine
- Mendeley-Reference Management Software & Researcher Network
- Dimensions.ai: Re-imagining discovery and access to research
- Index Copernicus Value(ICV): 81.49
- Citeseerx
- Massachusetts Institute of Technology (USA)
- Simpson University (USA)
- University of Louisville (USA)
- Biola University (USA)
- IE Library (Spain)
- Mount Saint Vincent University Library (Halifax, Nova Scotia Canada)
- University Of Arizona (USA)
- INDIANA UNIVERSITY-PURDUE UNIVERSITY INDIANAPOLIS (USA)
- Roderic Bowen Library and Archives (United Kingdom)
- University Library of Skövde (Sweden)
- Indiana University East (campuslibrary (USA))
- Tilburg University (The Netherlands)
- Williams College (USA)
- University of Connecticut (USA)
- Brandeis University (USA)
- Tufts University (USA)
- Boston University (USA)
- McGill University (Canada)
- Northeastern University (USA)
- BibSonomy-The blue social bookmark and publication sharing system
- Slide Share
- Academia
- Archive
- Scribd
- ISRJIF
- Cite Factor
- SJIF-InnoSpace
- ISSUU
- Research Bib
- infobaseindex
- I2OR
- DRJI journal-repository

AI Publication
International Journal of Advanced Engineering Research and Science (IJAERS)
104/108, Sector-10, Pratap Nagar, Jaipur, India